

# Transport simulations in nanosystems and low-dimensional systems

Von der Fakultät für Mathematik und Physik  
der Gottfried Wilhelm Leibniz Universität Hannover

zur Erlangung des Grades  
DOKTOR DER NATURWISSENSCHAFTEN  
Dr. rer. nat.  
genehmigte Dissertation

von  
Dipl. Phys. Malcolm Einhellinger  
geboren am 13.09.1980 in Wolfsburg.

2013

Referent: Prof. Dr. Eric Jeckelmann  
Korreferentin: Prof. Dr. Gertrud Zwicknagl  
Tag der Promotion: 14.11.2012



## Abstract

In this thesis, we investigate the transport properties of low-dimensional correlated nanosystems. Even though we can not simulate low-dimensional nanosystems in their full experimental reality, we approach this goal in three successive steps, extending the basis for future theoretical and experimental transport studies.

In the first step, we investigate one-dimensional conductors, i.e. the spinless fermion model and the Hubbard model. In that regard, we use the time evolving block decimation (TEBD) method to simulate finite systems driven out of equilibrium by an applied potential bias. Using the Fourier analysis based extraction (FABE) method – a procedure which we have developed based on the analysis of a related classical model (*LC* line) – we are able to calculate the stationary current using the results of the TEBD simulations of systems with a finite size. We show the full  $I$ - $V$  characteristics of the one-dimensional spinless fermion model with nearest-neighbor Coulomb interaction  $V_H$  and several  $I$ - $V$  characteristics of the one-dimensional Hubbard model with onsite Coulomb interactions  $U_H$ , using two different setups to generate currents (turning on/off a potential bias).

Since in an experimental situation lattice vibrations play an important role, in the second step we investigate the applicability of the TEBD method to nanostructures coupled to a bosonic bath. As TEBD has never been applied to such systems before, we have to compare our results with those from well-established methods such as the numerical renormalization group (NRG) procedure. Thus, we choose a two-site fermionic system coupled to a bosonic bath, for which NRG calculations are available, and find that the TEBD results agree with the NRG data.

In the third step we take into account that realistic nanowires are not exactly one-dimensional but their band structure consists of several one-dimensional subbands. To cover those cases, we modify the TEBD code such that it can be applied to two-dimensional structures, and simulate a ladder system described by the tight-binding Hamiltonian. Exact results from one-particle equation of motion calculations confirm our TEBD simulation outcomes.

Keywords: TEBD, low-dimensional correlated nanosystems, stationary current

## Zusammenfassung

In dieser Arbeit untersuchen wir die Transporteigenschaften von niedrigdimensionalen, korrelierten Nanosystemen und wie die theoretischen Ergebnisse experimentell gemessen werden können. Obwohl wir keine niedrigdimensionalen Nanosysteme in ihrer vollständigen, experimentellen Umgebung simulieren können, nähern wir uns dieser Zielsetzung in drei aufeinanderfolgenden Schritten. Dadurch erweitern wir die Basis für zukünftige theoretische und experimentelle Studien.

Im ersten Schritt untersuchen wir eindimensionale Leiter, insbesondere das spinlose Fermionen Modell und das Hubbard Modell. In diesem Zusammenhang benutzen wir die zeitentwickelte Blockdezimierungsmethode (TEBD) um endlich große Systeme im durch ein externes Potential erzeugten Nichtgleichgewicht zu simulieren. Mit Hilfe der Fourieranalyse basierten Extraktionsmethode (FABE) – einer Prozedur die wir mittels Analyse eines verwandten klassischen Modells (*LC* Modell) entwickelt haben – sind wir in der Lage den stationären Strom anhand der TEBD Simulationen eines endlich großen Systems zu berechnen. Wir zeigen die vollständigen  $I$ - $V$  Eigenschaften des eindimensionalen spinlosen Fermionen Modells mit nächster-Nachbar Coulomb-Wechselwirkung  $V_H$  und zudem  $I$ - $V$  Eigenschaften des eindimensionalen Hubbard Modells mit Vor-Ort Coulomb-Wechselwirkung  $|U_H|$  mit Hilfe zweier Setups zur Erzeugung eines Stromes (An-, bzw. Abschalten der angelegten Spannung).

Da in einer experimentellen Umgebung besonders Gitterschwingungen eine wichtige Rolle spielen, untersuchen wir im zweiten Schritt die Anwendbarkeit der TEBD Methode auf Nanostrukturen welche an ein bosonisches Bad gekoppelt sind. Da zudem TEBD niemals zuvor auf solche Systeme angewendet wurde, müssen zunächst Vergleiche mit etablierten und auf dieses Problem optimierten Methoden, wie zum Beispiel die Methode der numerischen Renormalisierungsgruppe (NRG) angestellt werden. Daher wählen wir ein fermionisches Zwei-Gitterplatz Modell, welches an ein bosonisches Bad gekoppelt ist, und für das NRG Rechnungen verfügbar sind. Dabei erhalten wir eine Übereinstimmung der TEBD- mit den NRG-Daten.

Im dritten Schritt berücksichtigen wir, dass realistische Nanodrähte nicht wirklich eindimensional sind, sondern dass ihre Bandstruktur aus vielen eindimensionalen Teilbändern aufgebaut ist. Um diese Situationen abzudecken, wird zunächst der TEBD-Code so modifiziert, dass er auf zweidimensionale Systeme angewandt werden kann. Anschließend simulieren wir ein Leitersystem welches durch den tight-binding Hamiltonoperator beschrieben wird. Die exakten Ergebnisse aus Einteilchen-Bewegungsgleichungs-Rechnungen bestätigen unsere TEBD Ergebnisse.

Schlagworte: TEBD, niedrig-dimensionale korrelierte Nanosysteme, stationärer Strom

# Contents

<b>Chapter 1. Introduction</b>	<b>9</b>
<b>Chapter 2. Classical <math>LC</math> line</b>	<b>15</b>
2.1 Currents in the $LC$ line . . . . .	16
2.2 Stationary current . . . . .	20
2.3 Finite-time and finite-size effects . . . . .	22
2.4 Determining the stationary current from finite system values .	25
2.5 Charge distribution . . . . .	29
2.6 Final notes on the $LC$ line . . . . .	31
2.6.1 Setups . . . . .	31
2.6.2 Applying the FABE approach to rectangular signals . .	31
2.7 Summary . . . . .	33
<b>Chapter 3. Non-equilibrium simulations</b>	<b>35</b>
3.1 Tight-binding model . . . . .	35
3.2 Setups . . . . .	36
3.3 One-particle equation of motion . . . . .	38
3.4 Finite-size effects and stationary current . . . . .	41
3.4.1 Finite-size induced oscillation . . . . .	41
3.4.2 Rapid oscillation on top of the square wave . . . . .	43
3.4.3 Applicability of the FABE approach to quantum systems	46
3.5 Summary . . . . .	48
<b>Chapter 4. TEBD method</b>	<b>51</b>
4.1 Parallelization . . . . .	54
4.2 Error sources . . . . .	56
4.3 Notes on the computation of stationary currents . . . . .	57
4.4 Summary . . . . .	58
<b>Chapter 5. Spinless fermion model</b>	<b>59</b>
5.1 Simulation parameters and errors . . . . .	61
5.2 Simulation results . . . . .	62
5.2.1 Current-voltage characteristics . . . . .	62
5.2.2 Influence of $V_H$ on the period $T^{\max}$ . . . . .	68

5.3	Summary . . . . .	69
<b>Chapter 6. Hubbard model</b>		<b>71</b>
6.1	Simulation parameters, modifications and errors . . . . .	72
6.2	Simulation results . . . . .	73
6.2.1	Equilibrium onsite potentials . . . . .	73
6.2.2	Current-voltage characteristics . . . . .	75
6.3	Summary . . . . .	77
<b>Chapter 7. Two-site system coupled to a bosonic bath</b>		<b>79</b>
7.1	Two-site fermionic system in a bosonic bath . . . . .	80
7.1.1	Mapping to a semi-infinite chain . . . . .	81
7.1.2	General simulation parameters . . . . .	83
7.2	Simulation results . . . . .	84
7.2.1	Equilibrium properties . . . . .	84
7.2.2	Realtime dynamics . . . . .	86
7.3	Summary . . . . .	88
<b>Chapter 8. Ladder systems</b>		<b>91</b>
8.1	Tight-binding ladder system . . . . .	92
8.2	Simulation parameters and errors . . . . .	92
8.3	Simulation results . . . . .	93
8.4	Summary . . . . .	95
<b>Chapter 9. Summary, Conclusion &amp; Outlook</b>		<b>97</b>
9.1	Summary & Conclusion . . . . .	97
9.2	Outlook . . . . .	99
<b>Appendix A. <i>LC</i> line</b>		<b>101</b>
A.1	Current in the finite <i>LC</i> line . . . . .	101
A.2	Solution of the integral (2.24) . . . . .	103
A.3	Solution of the integral (2.32) . . . . .	103
A.4	Approximations of the Bessel and Struve functions . . . . .	104
A.5	Remainder approximation for the Taylor series expansion . . . . .	105
<b>Appendix B. Non-equilibrium simulations</b>		<b>109</b>
B.1	Perturbation theory for small and large biases . . . . .	109
B.2	Period of the rectangular oscillation in the tight-binding model . . . . .	110
B.3	Current in the infinite tight-binding model . . . . .	111
<b>Appendix C. TEBD update scheme</b>		<b>113</b>



## CHAPTER 1

### Introduction

Our understanding of electronic transport in one-dimensional conductors is partly based on experimental outcomes such as for instance the transport through single-walled carbon nanotubes which first showed up in 1991 [1]. The first transport experiment for those structures, which can be down to a few nanometers in diameter, has then been reported in 1997 [2, 3] where a potential bias has been applied to two leads (referred to as source and drain) connected to the nanotube, and the resulting current through the nanotube has been measured. Due to the small diameter of those structures, they are often considered to be one-dimensional, but in fact the band structure is composed of multiple one-dimensional subbands. Thus, electronic correlations are important and the Fermi liquid theory for normal conductors can not be applied. According to the Tomonaga-Luttinger liquid (TLL) theory [4, 5, 6, 7], for the experimental setup of a nanotube connected to comparably infinitely large source and drain, a quantized conductance of  $4e^2/h$  for each subband is predicted, which has been successfully measured for metallic nanotubes [8]. Various other pseudo one-dimensional structures have been prepared and investigated, such as for instance metallic atomic chains on surface substrates [9], or structures based on anisotropic (for instance stepped) surfaces.

While experimentalists have to work hard to prepare such structures, theoreticians have it by far easier in one dimension. By contrast, it is quite a challenge to get theoretical results for transport problems including the infinitely large reservoirs used in experimental setups, and thus theoretical investigations on transport in one dimension are often restricted to finite system sizes (see for instance [10, 11] for simulations of finite systems), and source and drain are often modeled as part of the one-dimensional structure. Although the transport properties of one-dimensional conductors have been investigated both numerically and theoretically [12, 5, 7, 13, 14, 15], most of those studied are restricted to either small applied potential biases ('small' compared to the order of the band width in lattices and to the Fermi velocity in continuous models) or small Coulomb interactions, treating the electron-electron interaction perturbatively.

The transport properties of those systems for applied biases which are weak compared to the energy scale of the system are described by the TLL theory and exact equilibrium properties are available from Bethe Ansatz solutions for instance for the spin  $\frac{1}{2}$   $XXZ$  chain in Bethe's original work [16] (and closely related the spinless fermion model), the Kondo model and the Hubbard model [17, 18]. Without Coulomb interactions, exact results are also available for higher applied voltages [15].

The nonlinear regime has mostly been investigated in quantum contact problems, where the interaction is confined to a small region of the system, such as the Kondo model or the interacting resonant level model (IRLM). Within the framework of the TLL theory, current-voltage characteristics have been studied for the transport through a weak link [19, 20], for instance a one-dimensional interacting fermion system for a weak or strong potential barrier. Recently, the effects in the nonlinear regime have also been investigated [21], and a few works concerned with the full  $I$ - $V$  characteristics showed up [22, 11, 24]. Again, their interest lies mainly on systems with a small interacting region connected to non-interacting leads, such as the IRLM or the single impurity Anderson model (SIAM) and none concentrates on one-dimensional correlated conductors, i.e. where the Coulomb interaction is present in the whole system.

A major goal of this thesis is to investigate, determine and understand the nonlinear transport properties of low-dimensional correlated conductors in which the Coulomb interaction is not confined to a small region but present in the whole system. As electronics on a nanoscale has become more interesting in recent years, it is important to gain a better understanding of those processes to reveal the full scope of quantum wires as electronic components.

In this thesis, we do not try to reproduce a specific experimental situation, but to generally understand effects in correlated one-dimensional conductors. For that, our approach is to study a nanowire which is either itself charged such that parts of the nanowire act as source and drain or (more related to an actual experimental situation) to which an external voltage is applied. Nevertheless, several experimental aspects can not be ignored. Among many, the following three are the most important ones. First, many nanowires have a length-to-diameter ratio of 1000 and more, thus exceeding the present numerical possibilities. Second, a nanowire is not strictly one-dimensional but its band structure rather consists of multiple one-dimensional subbands, and third, lattice vibrations have to be taken into account. The connection of the nanowire to a surface and its coupling to leads is not considered in this thesis. Therefore, this thesis consists of three major parts: the investigation of one-dimensional correlated conductors, the study of a system coupled to a bosonic bath, and a research on the applicability of our methods to low-

dimensional quantum systems.

In the first and major part we study one-dimensional conductors, i.e. the half-filled spinless fermion model and the Hubbard model away from half-filling. Even though both models are exactly solvable by the Bethe Ansatz and their properties for small applied biases are described by the TLL theory, their transport properties in the nonlinear regime are not analytically accessible. Thus, we use the time evolving block decimation (TEBD) method [25, 26] to simulate the finite systems driven out of equilibrium using two different setups. In the first setup (I) we initially (at time  $t = 0$ ) apply a potential bias to source and drain (the two halves of the system). For  $t > 0$  we let the system evolve without potential bias and measure the current flowing through the bond between source and drain. In the second setup (II) for  $t = 0$  we prepare the system without a potential bias and apply a voltage for  $t > 0$ , which also generates a current. We again measure the current through the bond between source and drain.

Recently, several numerical methods for simulating the realtime dynamics of quantum lattices have been developed [27, 28, 29], such as for instance the time-dependent density matrix renormalization group (td-DMRG) or the TEBD method. Both methods can be described within a common mathematical framework, the matrix product states (MPS) [29, 30, 31]. The great advantage of the MPS description is the possibility to keep only the most ‘relevant’ states and discard all others. Fortunately, the contribution of each state decays very quickly, such that a rather small number  $\chi_c$  of states (the Schmidt dimension) has to be kept to get accurate results. However, as the entanglement in the system rises,  $\chi_c$  rises as well, thus defining the limit of what can be simulated anyway. The td-DMRG method has been successfully applied to study transport properties in quantum lattice systems [22, 11, 32, 33, 34, 10, 35, 23, 36, 37, 38], such as for instance the mentioned SIAM, the IRLM or the Hubbard model and the spinless fermion model, even for strong correlations (see for instance [39]). However, the original TEBD method has not yet been applied to electronic transport problems at all.

Although the use of the TEBD method is restricted to low-dimensional systems, it has a great advantage over the td-DMRG method. While the parallelization or the DMRG procedure is quite complicated [40, 41], TEBD is naturally parallelizable with an extremely low overhead, which will be presented in chapter 4 in this thesis. Using the TEBD method, we are able to compute the ground state and simulate the realtime evolution of a finite system of size  $N$  for a finite time  $t$ . Using one of the two setups described above, the system first goes into a transient phase in which a noisy and oscillating current is flowing. As the oscillations become smaller, the current

approaches a constant value while the system goes into a quasi-stationary phase which is continued until the particle front wave hits one of the borders of the system.

Since we are interested in the stationary behaviour of larger structures and especially in the DC transport properties (of infinitely large systems), we have to extrapolate the simulation results to the limits  $N \rightarrow \infty$  and then  $t \rightarrow \infty$ . As finite-size effects in quantum systems are very complex [42] and since we know only little about the influence of the borders in finite systems on the quasi-stationary current, we first study a related classical mode, the so-called *LC* line. With the aid on our findings, we develop a Fourier analysis based extraction (FABE) method, which allows us to calculate the stationary current in infinitely large systems using numerical data from small systems and short simulation times, for instance our TEBD simulation results.

Using TEBD and the FABE method, we determine the full  $I$ - $V$  characteristics of the spinless fermion model and  $I$ - $V$  characteristics of the Hubbard model. Without Coulomb interaction, these models are exactly solvable using the one-particle equation of motion formalism, and for small applied potential biases predictions from the TLL theory are available. All results from these special cases confirm the validity of our approach. We find that while for the linear regime the specific setup does not matter, it is highly decisive for the nonlinear current-voltage characteristics. For setup (I) the system shows a positive differential conductance all over the full voltage range and saturates at a finite value. For setup (II) a negative differential conductance occurs for higher applied voltages, even impeding a current flow for large enough values. Both effects in setup (II) that also occur in the non-interacting case, come from the finite bandwidth and the nonlinear dispersion of the excitations [42, 43].

As already mentioned, lattice vibrations (generally dissipation) play an important role in experimental situations. Thus in the second part of this thesis, we study the applicability of the TEBD method to systems coupled to a bosonic bath. For that purpose we choose a model that can be analyzed using TEBD and for which highly accurate (TD) NRG ((time dependent) numerical renormalization group) simulation results are available for comparison: a two-site fermionic system coupled to a bosonic bath [44]. This model describes the essentials of a two-electron transfer in a dissipative environment, which has been suggested to be an important mechanism in many biological processes, for instance in DNA [45].

Up to the present day, both methods, TEBD and NRG have been used to calculate the ground states and realtime dynamics of quantum systems, but a direct comparison has not been yet carried out. While (TD) NRG is well-suited for such simulations, providing very accurate descriptions for

small quantum systems coupled to a bosonic bath, TEBD can in principle be used for even more extended impurities, such as large molecular bridges or nanowires. Our analyses show that even though the TEBD results agree with the NRG outcomes, it is very hard to simulate the ground state since a very high Schmidt dimension is needed to get a sufficiently small truncation error. Moreover, even though the realtime evolution needs only a reasonably small Schmidt dimension, unfortunately a very small time step is necessary to obtain accurate results, which is due to very long time scales in which the transfer processes in this model take place.

In the third part of this thesis we extend the TEBD method in view of the fact that realistic nanowires are not truly one-dimensional. It is basically possible to use TEBD also for higher-dimensional systems by building an effectively one-dimensional system. With this mapping strategy, we use the TEBD method to simulate a ladder system which is described by the tight-binding Hamiltonian. We use the two setups described above in different ways and find by comparison with one-particle equation of motion calculations that the TEBD method gives correct results for such systems. It nevertheless remains a challenge to apply TEBD to two-dimensional systems with a wider extent.

This thesis is organized as follows: In the next chapter we introduce the classical  $LC$  line and the extraction method (FABE) used in the following chapters. We study several finite-size and finite-time effects of the classical model, deriving many of its properties, such as the period of the rectangular oscillation, or the origin of a rapid oscillation on top of the quasi-stationary plateau. In the third chapter we investigate stationary and transient current properties in a quantum tight-binding model, applying the one-particle equation of motion method and the FABE method from the second chapter. Based on the close connection to the classical  $LC$  line we show the applicability of the FABE method to quantum systems. The fourth chapter explains how we have implemented the parallel TEBD method and what errors are to be expected for the following simulations. In the fifth and sixth chapter we apply our methods to the spinless fermion model and the Hubbard model. We obtain the full  $I-V$  characteristics of the spinless fermion model (including a negative differential conductance and saturation effects). Moreover, we show that the period of the spinless fermion model for different  $V_H$  changes only due to the finite renormalized band width. Our investigations on the Hubbard model reveal  $I-V$  characteristics for one setup which show a similar saturation of the current as for the spinless fermion model. For describing a one-dimensional system in an experimental environment, we have to take lattice vibrations into account. The TEBD method is therefore adapted and used to simulate the two-site fermionic system coupled to a

bosonic bath in the seventh chapter and comparisons with NRG results [44] are carried out. As the band structure of a realistic nanotube consists of multiple one-dimensional subbands, we simulate a ladder system described by the tight-binding model using TEBD in the eighth chapter.

All important (in this thesis) realized implementations, calculations and findings are summarized in the last section of each chapter. Finally, we summarize all of our findings and give an outlook for further work in the ninth chapter. Some calculations are listed in appendices.

## CHAPTER 2

Classical  $LC$  line

In this chapter we start with the investigation of finite-size and finite-time effects in classical oscillator-systems to explain corresponding effects in simulation results from quantum systems. Classical oscillator-systems typically consist of macroscopic elements, such as a mass-spring system or – more electronically – an  $LC$ -Line built upon condensators, inductors and maybe resistors. Some classical setups are furthermore comparable to quantum mechanical systems, regarding for instance particle densities and currents. Those classical setups are in most cases easier to describe and the corresponding models more often solvable than their quantum mechanical pendants. Furthermore, they open the way to understanding the origin of quantum effects and they are a useful tool for gaining more informations about quantum systems, for instance by comparing model parameters and simulation results.

In the following, we concentrate on the so-called  $LC$  line, shown in figure 2.1. The  $LC$  line has been under research as an electrical circuit implementation of a Toda chain [46, 47, 48], a nonlinear oscillator chain that, among others, describes the propagation of soliton waves. Further investigations of the  $LC$  line have so far been focused on the continuous and linear case, for instance tunneling rates in single or double metal-insulator-metal junctions which behave similar to capacitors with  $Q = C \cdot U$  [49]. As the connection between those ‘capacitors’ can be modeled by an inductor, we arrive at the  $LC$  line which we use to describe some of the basic effects in

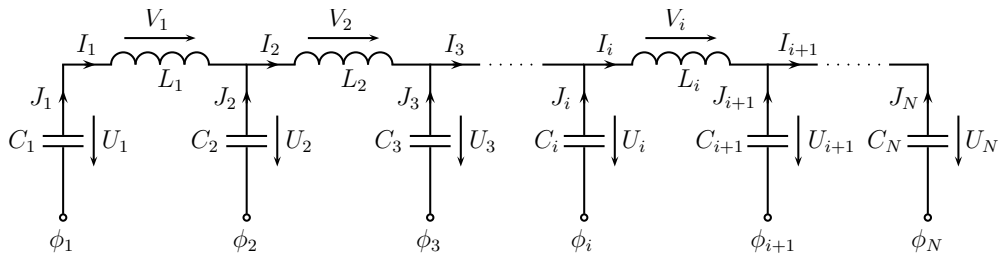


Figure 2.1. Classical  $LC$  line with onsite applied potentials  $\phi_i$ .

chains of coupled quantum sites (one-dimensional quantum wire). While the *LC* line has been analyzed for the nonlinear and the linear (and continuous) cases, our focus lies on the discrete and linear model for finite and infinite sizes.

We show that the *LC* line is well-suited as the classical representation of a one-dimensional quantum wire described by the tight-binding Hamiltonian, while our main focus lies on the behaviour of the current, especially the influence of finite-size effects and stationary values for the infinite-size limit. We present solutions for a setup in which an initial imbalance of charge carriers on the condensators leads to an oscillating, rectangular current curve as the charge carriers move back and forth in the *LC* line: the formerly described setup (I). Scaling the system size  $N$  to infinity leads to an enlargement of the square wave period, and for large times a stationary current  $\bar{I}$  is flowing. Subsequently, a method is presented to compute the stationary current  $\bar{I}$  for infinitely large systems using finite-size simulation results. Based on the comparison of the classical and quantum mechanical model this approach will be applied to quantum systems.

## 2.1 Currents in the *LC* line

Figure 2.1 shows the classical setup of a one-dimensional wire that possesses many properties of a one-dimensional quantum chain. This *LC* line is a combination of condensators and inductors whereas the present model is extended to enable onsite applied potentials  $\phi_i$ . For this setup, the following relations can be derived using elementary electrotechnical relations and Kirchhoff's laws

$$\begin{aligned} J_i &= -C_i \dot{U}_i \quad ; \quad i = 1, 2, \dots, N \\ V_i &= L_i \dot{I}_i \quad ; \quad i = 1, 2, \dots, N - 1 \\ I_{i+1} &= I_i + J_{i+1} \quad ; \quad i = 0, 1, \dots, N - 1 \end{aligned} \tag{2.1}$$

and

$$V_i = U_i - U_{i+1} + \phi_i - \phi_{i+1} \quad ; \quad i = 1, 2, \dots, N - 1 \tag{2.2}$$

where  $I_0 = I_N = 0$  was defined.  $V_i$  in equation (2.2) results from the potential difference between the left and right connection of the  $i$ -th inductor.  $C_i$  denotes the capacity of the  $i$ -th capacitor,  $U_i$  the voltage drop over the capacitor,  $L_i$  the inductance of the  $i$ -th inductor and  $I_i$  and  $J_i$  are the currents as shown in figure 2.1.  $Q_i$  is the charge of the  $i$ -th capacitor and the  $\phi_i$



denote externally applied potentials. From the equations above follows

$$I_{i+1} = I_i + J_{i+1} = I_i - C_{i+1}\dot{U}_{i+1}, \quad (2.3)$$

$$L_i\dot{I}_i = U_i - U_{i+1} + \phi_i - \phi_{i+1}. \quad (2.4)$$

Differentiating equation (2.4) with respect to the time  $t$  and plugging in  $\dot{U}_i$  from equation (2.3) gives in matrix notation

$$\ddot{\vec{I}} = -M\dot{\vec{I}} + \dot{\vec{\Phi}} \quad (2.5)$$

with  $\dot{\Phi}_i = (\dot{\phi}_i - \dot{\phi}_{i+1})/L_i$  and

$$M_{ij} = -\delta_{i,j+1} \left( \frac{1}{L_i C_i} \right) - \delta_{i,j-1} \left( \frac{1}{L_i C_{i+1}} \right) + \delta_{ij} \left( \frac{1}{L_i C_{i+1}} + \frac{1}{L_i C_i} \right). \quad (2.6)$$

Hence, we get

$$\begin{aligned} O^{-1}\ddot{\vec{I}} &= -O^{-1}M(OO^{-1})\dot{\vec{I}} + O^{-1}\dot{\vec{\Phi}} \\ \Rightarrow \quad \ddot{\vec{q}} &= -\Omega\dot{\vec{q}} + \vec{c} \end{aligned} \quad (2.7)$$

with

$$\vec{q} = O^{-1}\dot{\vec{I}} \quad , \quad \vec{c} = O^{-1}\dot{\vec{\Phi}} \quad \text{and} \quad \Omega = O^{-1}MO \quad ; \quad \Omega_{ij} = \delta_{ij}\lambda_i \quad (2.8)$$

where  $O$  contains the normalized eigenvectors of  $M$  in its columns and  $\lambda_i$  are the eigenvalues of  $M$ . In index notation it is written as

$$\ddot{q}_k = -\lambda_k q_k + c_k \quad ; \quad k = 1, 2, \dots, N-1 \quad (2.9)$$

which describes a harmonic oscillator driven by an external force. We consider an  $LC$  line with equal capacities and inductances

$$L_i = L \quad \text{and} \quad C_i = C \quad \forall i \quad (2.10)$$

and temporally constant applied potentials  $\dot{\vec{\Phi}} = \vec{0}$  for which equation (2.5) reduces to

$$\ddot{\vec{I}} = -\frac{1}{LC}m\dot{\vec{I}} + \dot{\vec{\Phi}} \quad (2.11)$$

with

$$m_{ij} = -\delta_{i,j+1} - \delta_{i,j-1} + 2\delta_{ij}. \quad (2.12)$$

In that case, the current is given by [app. A.1]

$$I_i(t) = \sqrt{\frac{2}{N}} \sum_{k=1}^{N-1} \sin\left(\frac{ki\pi}{N}\right) [b_k \sin(\omega_k t) + d_k \cos(\omega_k t)] \quad (2.13)$$

and

$$\omega_k = \frac{2}{\sqrt{LC}} \sin\left(\frac{k\pi}{2N}\right). \quad (2.14)$$

With  $Q_{0,i} = Q_i(t=0)$  and  $\phi_{0,i} = \phi_i(t=0)$  one has

$$\dot{I}_i(0) = \frac{1}{LC} (Q_{0,i} - Q_{0,i+1}) + \frac{1}{L} (\phi_{0,i} - \phi_{0,i+1}) \quad (2.15)$$

and thus using the orthogonality of the sine functions, it follows

$$b_k = \frac{\sqrt{2}}{\omega_k L \sqrt{N}} \sum_{i=1}^{N-1} \left[ \frac{1}{C} (Q_{0,i} - Q_{0,i+1}) + \phi_{0,i} - \phi_{0,i+1} \right] \sin\left(\frac{ki\pi}{N}\right). \quad (2.16)$$

We further assume that initially (at time  $t=0$ ) no current is flowing

$$I_i(0) = 0 \quad \forall i \quad \Rightarrow \quad d_k = 0 \quad \forall k \quad (2.17)$$

which leads to the following expression for the current through the  $i$ -th inductor

$$I_i(t) = \sqrt{\frac{2}{N}} \sum_{k=1}^{N-1} b_k \sin\left(\frac{ki\pi}{N}\right) \sin(\omega_k t). \quad (2.18)$$

Another simplification shall be that the chain is divided into two halves in which the charge carriers are uniformly distributed for  $t=0$ , i.e.

$$\begin{aligned} Q_L = Q_{0,i=1,\dots,\frac{N}{2}} \quad , \quad Q_R = Q_{0,i=\frac{N}{2}+1,\dots,N} \\ \text{and} \quad \phi_i(t) = 0 \quad \forall i, t. \end{aligned} \quad (2.19)$$

Figure 2.2 shows the current through the inductor  $L_{N/2}$  according to the general formula for the current at site  $N/2$  for any even  $N$

$$\begin{aligned} I_{\frac{N}{2}}(t) &= \frac{2(Q_L - Q_R)}{NLC} \sum_{k=1}^{N-1} \frac{1}{\omega_k} \underbrace{\sin^2\left(\frac{k\pi}{2}\right)}_{1(k \text{ odd}) \text{ or } 0(k \text{ even})} \sin(\omega_k t) \\ &= \frac{Q_L - Q_R}{N\sqrt{LC}} \sum_{k=1}^{N/2} \frac{\sin\left(\frac{2}{\sqrt{LC}}\eta_k t\right)}{\eta_k} \end{aligned} \quad (2.20)$$

where equation (2.16) was used for  $b_k$  and equation (2.19) for  $Q_L$  and  $Q_R$ . The substitution  $k \rightarrow (2k-1)$  was applied during the last transformation to get rid of the  $\sin^2$ -term and the definition

$$\eta_k = \omega_{2k-1} \frac{\sqrt{LC}}{2} = \sin\left(\frac{(2k-1)\pi}{2N}\right) \quad (2.21)$$

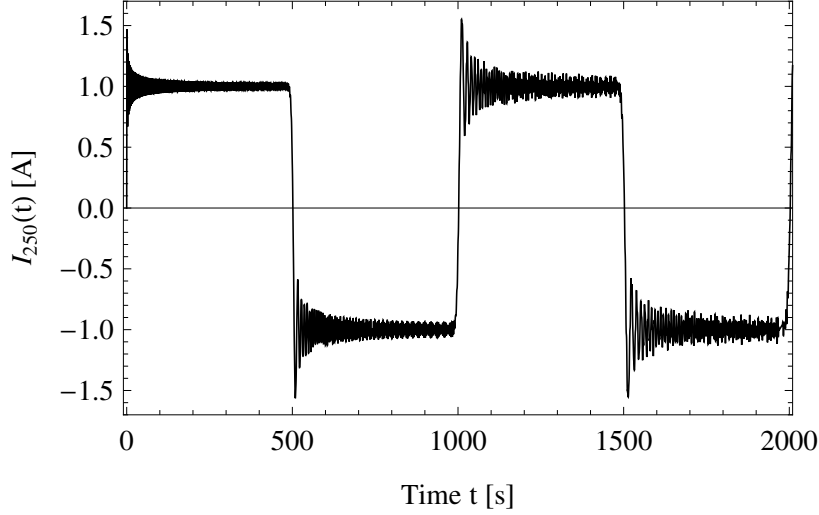


Figure 2.2. Current  $I_{250}(t)$  for a classical wire of size  $N = 500$  through the inductor at position  $N/2$ .  $L = C = 1$ ,  $Q_L = Q_{0,i \leq N/2} = 1$  and  $Q_R = Q_{0,i > N/2} = -1$

was introduced in that context. All values for the classical system ( $Q_i$ ,  $t$ ,  $L$ ,  $C$ , etc.) are given in S.I. units unless otherwise specified.

In figure 2.2, one can see a rectangularly oscillating curve, superimposed by small oscillations, magnified in figure 2.3. While the rectangular shape of the dominant oscillation is understandable through the picture of charge carriers moving back and forth in the line, the rapid oscillation on top of the square wave is harder to explain and we will later take a closer look at it. The period  $T_{\text{cl}}^{\text{max}}$  of the square wave can be calculated by using equation (2.20) and (2.21) and taking only the smallest frequency ( $k = 1$ ) into account

$$T_{\text{cl}}^{\text{max}} = \frac{\pi\sqrt{LC}}{\sin\left(\frac{\pi}{2N}\right)}. \quad (2.22)$$

For large system sizes ( $N \gg 1$ ) this period is approximately given by

$$T_{\text{cl}}^{\text{max}} \approx 2N\sqrt{LC} \quad (2.23)$$

and is thus linearly dependent on  $N$ . In the second half period of the current in figure 2.2 one can see a beat upon the rapid oscillation. This is due to the unequally distributed charges which form an oscillating pattern and so create additional frequencies in the current. This effect also occurs in quantum wires, not only after the reflection at the right border but already

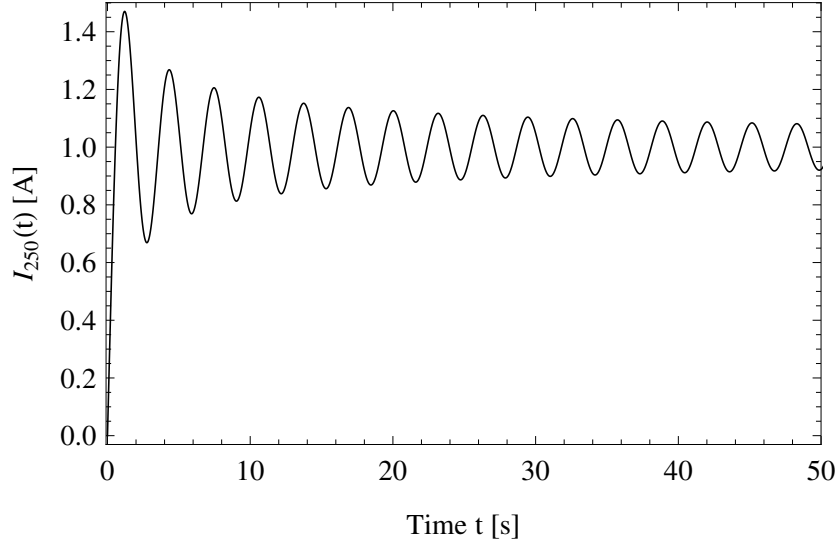


Figure 2.3. Magnification of figure 2.2. Current  $I_{250}(t)$  for a classical wire with  $L = C = 1$  and  $Q_L = -Q_R = 1$

from the beginning due to using an initial (ground) state with non-uniform local densities, see chapter 3.

## 2.2 Stationary current

In contrast to the oscillating current in a finite system where the charge carriers are scattered at the borders, we assume that the current in an infinitely large system is constantly flowing in one direction. To validate this assumption one has to execute the limit  $N \rightarrow \infty$  first, and then take the limit  $t \rightarrow \infty$ . In the limit  $N \rightarrow \infty$  one gets from equation (2.20)

$$\begin{aligned} I_\infty(t) &= \lim_{N \rightarrow \infty} I_{N/2}(t) \\ &= \frac{Q_L - Q_R}{\sqrt{LC}} \frac{1}{\pi} \int_0^{\frac{\pi}{2}} \frac{\sin\left(\frac{2}{\sqrt{LC}} \sin(x)t\right)}{\sin(x)} dx. \end{aligned} \quad (2.24)$$

The solution is given by [app. A.2]

$$\begin{aligned} I_\infty(t) &= \frac{(Q_L - Q_R)t}{2LC} [\mathcal{J}_0(\varphi t) (2 - \pi \mathcal{H}_1(\varphi t)) \\ &\quad + \pi \mathcal{J}_1(\varphi t) \mathcal{H}_0(\varphi t)] \end{aligned} \quad (2.25)$$

with

$$\varphi = \frac{2}{\sqrt{LC}}. \quad (2.26)$$

$\mathcal{J}_n(x)$  are the Bessel functions of the first kind and  $\mathcal{H}_n(x)$  denote the Struve functions [50].

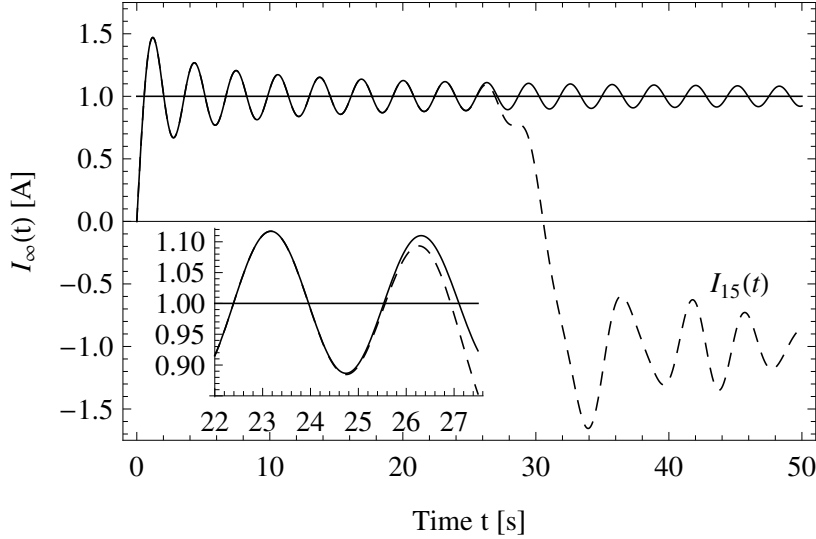


Figure 2.4. Solid curve: Current  $I_\infty(t)$  for a classical infinite wire through the inductor at the middle with  $L = C = 1$ ,  $Q_L = 1$  and  $Q_R = -1$ . The dashed curve is the current for a finite system with size  $N = 30$ . The constant line denotes the stationary value  $\bar{I}_{\text{cl}} = 1$  against which the solid line converges.

The current for the infinite system (2.25) is shown in figure 2.4 and it shows that for smaller times the curve for finite system sizes matches the one for the infinitely large LC line. Hence, a very accurate approximation of the value of a stationary current in an infinitely large system can be extracted from the value of a corresponding finite system result. This behaviour will be later used for the analysis of quantum systems.

Using the approximations (A.12) from [app. A.4] for the Bessel and Struve functions we find the value of the stationary current in the infinitely large system

$$\bar{I}_{\text{cl}} = \lim_{t \rightarrow \infty} I_\infty(t) = \frac{Q_L - Q_R}{2\sqrt{LC}}. \quad (2.27)$$

The conductance  $G_{\text{cl}}$  for the stationary case is given by

$$G_{\text{cl}} = \frac{\bar{I}_{\text{cl}}}{V} = \frac{1}{2} \sqrt{\frac{C}{L}} \quad (2.28)$$

with a local voltage drop  $V = (Q_L - Q_R)/C$  in the middle of the chain.

## 2.3 Finite-time and finite-size effects

In order to describe finite-time effects in the infinite system we seek for a simpler current expression which does not only give the correct stationary value but also a good approximation for the short-time behaviour. Using the approximations (A.15) from [app. A.4],  $I_{\infty}(t)$  can be transformed into the following form for  $t \gg 1$

$$\begin{aligned} I_{\text{app}}(t) &= \bar{I}_{\text{cl}} + I_{\text{dev}}(t) \\ &= \bar{I}_{\text{cl}} + \frac{Q_L - Q_R}{16} \sqrt{\frac{\varphi}{\pi t}} [(10\pi - 32)(\sin^2(\varphi t) \\ &\quad + \sin(\varphi t) \cos(\varphi t)) \\ &\quad + 4(\sin(\varphi t) - \cos(\varphi t))] + \mathcal{O}\left(\frac{1}{t}\right) \end{aligned} \quad (2.29)$$

with  $\varphi = 2/\sqrt{LC}$ .  $I_{\text{dev}}(t)$  denotes the deviation from the stationary current  $\bar{I}_{\text{cl}}$  from equation (2.27). The order  $\mathcal{O}(t^{-1})$  of the rest term is only valid if the approximation of  $\mathcal{H}_1(x)$  in (A.15) has an error of smaller order which holds as argued in [51]. As shown in figure 2.5, expression (2.29) is a persuasive approximation even for smaller times and thus forms a good explanatory basis for short-time effects in the LC line. It states a general  $\mathcal{O}(1/\sqrt{t})$  decay of the amplitudes of the rapid oscillation in the current curve, which is the maximal order of the error for an approximation of the stationary current (2.27) using a finite-time (i.e. a finite-size) result.

Instead of looking at the current through a single inductor, one can consider the current through two or more neighboring ones. We will show that the short time behaviour of this current has some advantages compared to the simple  $I_{N/2}(t)$  curve. We define the quantity of interest for even  $N$  as

$$I_{\text{m},N/2}(t) = \frac{1}{2} I_{N/2}(t) + \frac{1}{4} (I_{N/2+1}(t) + I_{N/2-1}(t)) \quad (2.30)$$

which is equal to the expression  $\frac{1}{2}(I_{N/2}(t) + I_{N/2+1}(t))$ , whereas for the latter expression the subsequently explained effect also occurs for odd  $N$  for the

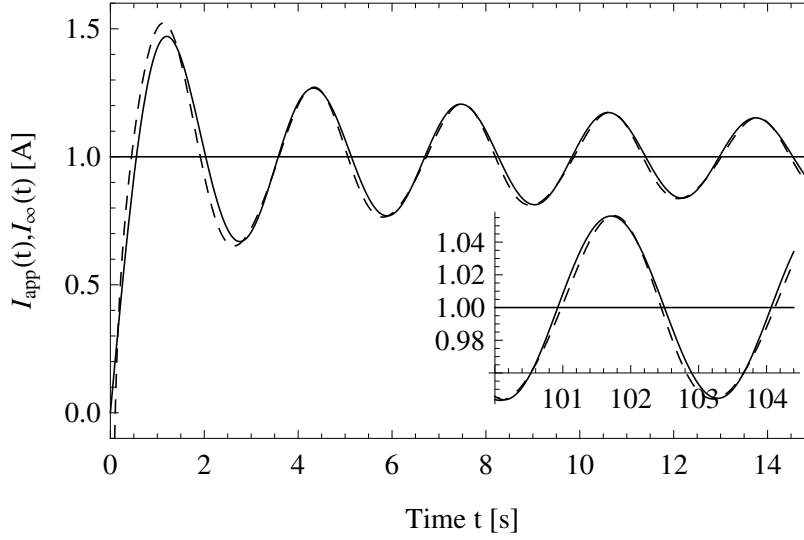


Figure 2.5. Exact current  $I_\infty(t)$  (solid line) and approximate current  $I_{\text{app}}(t)$  (dashed line) with  $L = C = 1$  and  $Q_L = -Q_R = 1$

substitution  $N/2 \rightarrow (N-1)/2$ . In the limit  $N \rightarrow \infty, t \rightarrow \infty$ , the expression  $I_{\text{m},N/2}(t)$  converges against the same value as  $I_{N/2}(t)$  which implies that the stationary current is as well assessable via the current through two or more adjacent inductors. From (2.18) one gets

$$I_{\text{m},N/2}(t) = \frac{Q_L - Q_R}{NLC} \sum_{k=1}^{N-1} \frac{1}{\omega_k} \sin(\omega_k t) \sin^2\left(\frac{k\pi}{2}\right) \cdot \left[1 + \cos\left(\frac{k\pi}{N}\right)\right] \quad (2.31)$$

with expression (2.16) for  $b_k$  and the step distribution for the charges (2.19). In the limit  $N \rightarrow \infty$  it follows

$$I_{\text{m},\infty}(t) = \frac{Q_L - Q_R}{\pi\sqrt{LC}} \int_0^{\pi/2} \frac{\sin\left(\frac{2}{\sqrt{LC}} \sin(x) t\right)}{\sin(x)} \cos^2(x) dx. \quad (2.32)$$

The solution of this integral is given by [app. A.3]

$$I_{\text{m},\infty}(t) = \frac{Q_L - Q_R}{\sqrt{LC}} \left[ \mathcal{J}_1(\varphi t) \left( \frac{\pi\varphi t}{4} \mathcal{H}_0(\varphi t) - \frac{1}{\varphi^2 t^2} - \frac{1}{2} \right) + \mathcal{J}_0(\varphi t) \left( \frac{\varphi t}{2} + \frac{1}{2\varphi t} - \frac{\pi\varphi t}{4} \mathcal{H}_1(\varphi t) \right) \right]. \quad (2.33)$$

This result, plotted in figure 2.6 together with equation (2.25) for the current

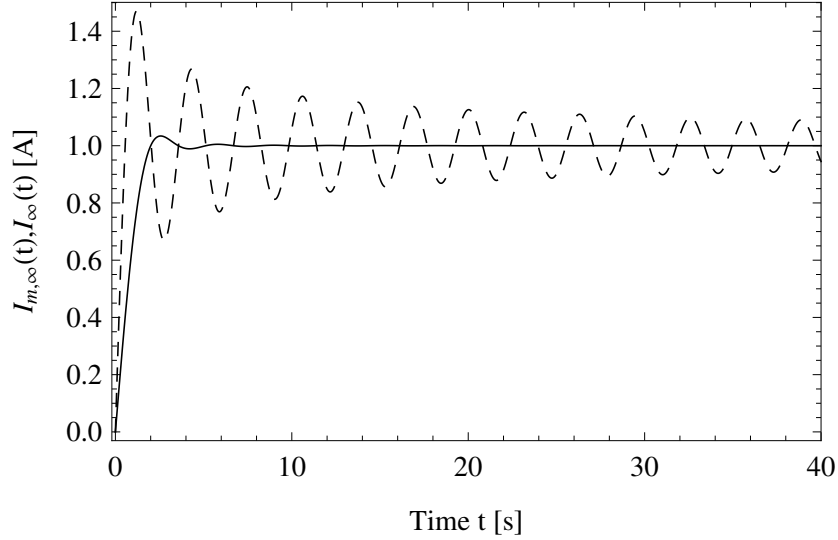


Figure 2.6. Solid curve: Current  $I_{m,\infty}(t)$  through two adjacent inductors in the middle; equation (2.33). Dashed curve: Current  $I_\infty(t)$  from equation (2.25) through a single inductor.  $L = C = 1$ ,  $Q_L = 1$  and  $Q_R = -1$ .

$I_\infty(t)$  through a single inductor, shows almost no rapid oscillations. An approximative expression for the rapid oscillations  $I_r(t) \approx I_{\text{dev}}(t)$  can therefore be derived using the difference between the two current expressions (2.33) and (2.25)

$$\begin{aligned} I_r(t) &= I_{m,\infty}(t) - I_\infty(t) \\ &= \frac{Q_L - Q_R}{4} \left[ \frac{\mathcal{J}_0(\varphi t)}{t} - \left( \frac{2}{\varphi t^2} + \varphi \right) \mathcal{J}_1(\varphi t) \right]. \end{aligned} \quad (2.34)$$

Using the approximations (A.15) for the remaining Bessel functions one has

$$\begin{aligned} I_{r,\text{app}}(t) &= \frac{(Q_L - Q_R)}{32\sqrt{\pi}} \frac{(\varphi t)^{5/2}}{t} \left[ (5(\varphi t)^2 + 8(\varphi t)^3 \right. \\ &\quad \left. + 15\varphi t - 6) \cos(\varphi t) (5(\varphi t)^2 - 8(\varphi t)^3 \right. \\ &\quad \left. - 15\varphi t - 6) \sin(\varphi t) \right]. \end{aligned} \quad (2.35)$$

Hence the rapid oscillations have a radial frequency  $\varphi = 2/\sqrt{LC} = 2\pi/T_{\text{cl}}^{\text{min}}$  and thus

$$T_{\text{cl}}^{\text{min}} = \pi\sqrt{LC}. \quad (2.36)$$



The effect that the rapid oscillations of currents through two adjacent inductors (bonds) cancel out is also present in a quantum wire, see chapter 3. This shows the close resemblance between the classical  $LC$  line and a corresponding quantum system.

## 2.4 Determining the stationary current from finite system values

There are various methods to calculate the stationary current from simulation results stemming from systems with finite size. The most obvious and easiest way to do so is to use the curve of a current through the middle inductor (or the mean value of currents through two or more adjacent inductors) and to compute the mean value over a certain time interval in the quasi-stationary regime. In contrast to this approach, we will present a more analytical method using the Fourier transformation. Although we can not prove that the following strategy can be applied to quantum mechanical systems with complicated interactions, several numerical and theoretical indications are given in subsequent chapters. We start with a square wave described by its Fourier series

$$\mathcal{R}_m(t) = \frac{4A}{\pi} \sum_{k=1}^m \frac{\sin((2k-1)\chi t)}{2k-1} \quad (2.37)$$

where  $m$  determines the number of harmonics,  $A$  denotes the value of the quasi-stationary plateau and  $\chi = 2\pi/T_R^{\max}$  where  $T_R^{\max}$  is the period of the square wave. This signal has certain similarities with the current curve  $I_{N/2}(t)$ . It possesses a quasi-stationary regime which becomes infinite for  $\chi \rightarrow 0$  (equals  $N \rightarrow \infty$  for the  $LC$  line) and shows a rapid and decaying oscillation on top of it. The main difference between the composition of the current curve (2.20) and the square wave is the presence of sine-functions in the current curve that enclose the  $(2k-1)$ -terms.

The current in (2.20) is dependent on  $\eta_k$  and it is thus convenient to write  $I_{N/2}^{[\eta_k]}(t)$  where  $\eta_k = \sin(\frac{(2k-1)\pi}{2N})$ . Choosing an  $\eta_k$  without the enclosing sine-functions gives

$$I_{N/2}^{[\frac{(2k-1)\pi}{2N}]}(t) = \frac{2(Q_L - Q_R)}{\pi\sqrt{LC}} \sum_{k=1}^{N/2} \frac{\sin((2k-1)\varphi't)}{2k-1} \quad (2.38)$$

with  $\varphi' = \varphi\pi/(2N) = \pi/(N\sqrt{LC})$ . Since expression (2.38) now describes a square wave, one can compare it with (2.37) and get its quasi-stationary

value

$$A = \frac{Q_L - Q_R}{2\sqrt{LC}} = \bar{I}_{\text{cl}} \quad (2.39)$$

which is equal to the value that was derived for the stationary current in equation (2.27). Remarkably, the enclosing sine-functions do not change the stationary value, i.e. the expression (2.38) and the current in an  $LC$  line have the same stationary value for  $N \rightarrow \infty$ . In case of expression (2.38) this value is equal to the quasi-stationary value (2.39), which leads to the idea to calculate the quasi-stationary value from a given current signal in a finite system (using the procedure described below) and use it as approximation for the stationary current value for  $N \rightarrow \infty$ . Applying the Fourier-transformation

$$\tilde{I}_{N/2}(\omega) = \int_{-\infty}^{\infty} I_{N/2}(t)e^{i\omega t} dt \quad (2.40)$$

term by term to expression (2.20) gives

$$\tilde{I}_{N/2}(\omega) = i \cdot \frac{(Q_L - Q_R)}{N\sqrt{LC}} \sum_{k=1}^{N/2} \frac{\delta(\omega + \varphi\eta_k) - \delta(\omega - \varphi\eta_k)}{\eta_k} \quad (2.41)$$

with equation (2.21) for  $\eta_k$  and  $\varphi = 2/\sqrt{LC}$ . If numerical data with  $m$  values are given, one has to apply a discrete Fourier transformation which preserves the area underneath a delta peak, such that for any interval  $\Delta t$  containing a single delta function  $a \cdot \delta(x - x_0)$  the peak is of height  $a/\Delta t$ . Taking only the first ( $k = 1$ ) and only the positive delta-peak into account and using the discrete transformation

$$\tilde{f}(j) = \frac{1}{m} \sum_{k=0}^{m-1} f(k)e^{-ikj\omega_0} \quad \text{with } \omega_0 = \frac{2\pi}{m} \quad (2.42)$$

and  $j = 0, 1, \dots, m - 1$ , one gets for the current

$$\bar{I}_{\text{cl}} = \frac{\text{Im}[\tilde{I}_{N/2}(\omega_1)]N\Delta t}{2} \cdot \sin\left(\frac{\pi}{2N}\right) \quad (2.43)$$

where  $\text{Im}[\tilde{I}_{N/2}(\omega_1)]$  is the height of the first discrete peak ( $k = 1$ ). In fact, one can not expect to know the precise form of  $\eta_k$  for complicated quantum systems. Instead, one can take a first order approximative expression. For  $N \gg 1$  it holds  $\sin\left(\frac{\pi}{2N}\right) \approx \frac{\pi}{2N}$ , which implies that the given curve is a square wave, and thus

$$\bar{I}_{\text{cl}} \approx \frac{\pi}{4} \text{Im}[\tilde{I}_{N/2}(\omega_1)]\Delta t \quad (2.44)$$

with a relative error of [app. A.5]

$$\frac{|\Delta \bar{I}_{\text{cl}}|}{|\bar{I}_{\text{cl}}|} \leq \frac{\pi^2}{8N^2}. \quad (2.45)$$

It is important to remark that equation (2.44) is not only an exact result for a square wave, but also an excellent approximation for the *LC* line current with a maximal error according to equation (2.45).

As our analyses in section 2.5 reveal, the charge carriers in the *LC* line coming from the left half first reach the right border at  $t \approx T_{\text{cl}}^{\text{max}}/4$ . After this time the finite system size has a significant influence on the simulation results. Applying a discrete Fourier transformation means to assume that a periodic function is given. For that, and to minimize the upcoming error for times larger than  $T_{\text{cl}}^{\text{max}}/4$ , the following procedure is proposed: From a given current curve  $I_{N/2}(t)$  stemming from simulation results, first determine a position  $t = t_s$  in the vicinity of  $T_{\text{cl}}^{\text{max}}/4$  – but smaller than  $T_{\text{cl}}^{\text{max}}/4$  – where the curve could be mirrored along a parallel to the *y*-axis such that the loss of continuity is minimized, which is the case for instance at inflection points. Then consider a  $4t_s$ -periodic function, constructed as follows

$$I_{\mathcal{R}}(t, t_s) = \begin{cases} I_{N/2}(t) & \text{for } 0 \leq t < t_s \\ I_{N/2}(2t_s - t) & \text{for } t_s \leq t < 2t_s \\ -I_{N/2}(t - 2t_s) & \text{for } 2t_s \leq t < 3t_s \\ -I_{N/2}(4t_s - t) & \text{for } 3t_s \leq t \leq 4t_s \end{cases} \quad (2.46)$$

and apply the Fourier transformation to the constructed signal (2.46) and use equation (2.44) to calculate the corresponding stationary value of the current, see figure 2.7. In order to keep the notations short, we call this method for extracting the stationary current from outcomes of analyses of systems with finite size the ‘Fourier analysis based extraction’ (FABE) method.

Let us clarify the construction (2.46) once again: Assume that one has a current curve with a period of  $T_{\text{cl}}^{\text{max}}$ . One takes only the first fourth of the signal into account and then searches for a minimum or maximum in the negative vicinity of  $T_{\text{cl}}^{\text{max}}/4$  such that a new continuous curve can be constructed using 4 times the remaining signal from  $t = t_0$  to  $t_s = t_{\text{min or max}}$ . Finally, one applies the discrete Fourier transformation to the constructed signal and uses equation (2.44) to calculate the stationary current.

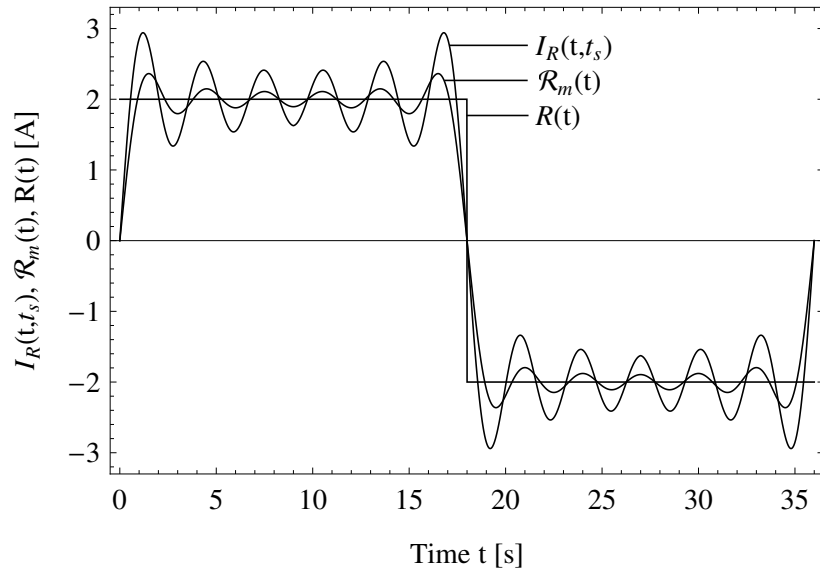


Figure 2.7. Constructed signal  $I_{\mathcal{R}}(t, t_s)$  from simulation results together with the Fourier series representation of a square wave  $\mathcal{R}_m(t)$  from (2.37) with  $m = 8$  and an ideal square wave  $R(t)$ . The Fourier transformation of  $I_{\mathcal{R}}(t, t_s)$  and expression (2.44) was used to calculate the amplitude of  $R(t)$ .

## 2.5 Charge distribution

In the following we investigate the behaviour of the charge distribution with  $Q = C \cdot U$  with constant  $C$ , to show when the finite size of a system starts to become important, and to compare those results with the analyses of quantum systems in chapter 3. From equations (2.1) it follows

$$\begin{aligned} \dot{U}_i &= \frac{1}{C}(I_{i-1} - I_i) \\ \Rightarrow U_i(t) &= \frac{1}{C} \int_0^t I_{i-1}(t') - I_i(t') dt' \end{aligned} \quad (2.47)$$

where all  $C_i$  has been chosen equal to  $C$  as usual and  $I_i(t)$  is given by equation (2.18). The initial conditions are given with  $b_k$  from (2.16)

$$b_k = \frac{\sqrt{2}}{\omega_k L \sqrt{N}} \sum_{p=1}^{N-1} \underbrace{\left[ \frac{1}{C} (Q_{0,p} - Q_{0,p+1}) + \phi_{0,p} - \phi_{0,p+1} \right]}_{u_{0,p} - u_{0,p+1}} \sin\left(\frac{kp\pi}{N}\right) \quad (2.48)$$

with  $\omega_k = \varphi \sin\left(\frac{k\pi}{2N}\right)$  from (2.14),  $\varphi = \frac{2}{\sqrt{LC}}$ ,  $u_p(t) = U_p(t) + \phi_p(t)$  and  $u_{0,p} = u_p(t=0)$ . It directly follows

$$\begin{aligned} U_i(t) &= \frac{2}{NLC} \sum_{k,p=1}^{N-1} \frac{1}{\omega_k} (u_{0,p} - u_{0,p+1}) \sin\left(\frac{kp\pi}{N}\right) \\ &\quad \cdot \left[ \underbrace{\sin\left(\frac{k(i-1)\pi}{N}\right)}_{\text{from } I_{i-1}(t)} - \underbrace{\sin\left(\frac{ki\pi}{N}\right)}_{\text{from } I_i(t)} \right] \int_0^t \sin(\omega_k t') dt' \\ &= \frac{1}{2N} \sum_{k,p=1}^{N-1} \frac{u_{0,p} - u_{0,p+1}}{\sin^2\left(\frac{k\pi}{2N}\right)} \sin\left(\frac{kp\pi}{N}\right) \\ &\quad \cdot \left[ \sin\left(\frac{k(i-1)\pi}{N}\right) - \sin\left(\frac{ki\pi}{N}\right) \right] \cos\left(\varphi \sin\left(\frac{k\pi}{2N}\right) t\right) + U_0. \end{aligned} \quad (2.50)$$

$U_0$  shifts the distribution of the initial voltages by an offset  $\sum_i U_{i,0} = U_0$ . We note that without  $U_0$  only voltage differences  $u_{0,p} - u_{0,p+1}$  contribute, such that  $\sum_i U_{i,0} = 0$ . Taking a look at figure 2.8 where the left half of the chain was initially charged, one can see that the charge carriers move back and forth in the LC-Line as expected. A corresponding movie is available on [whypsi.com/einhellinger/chargeDistribution.zip](http://whypsi.com/einhellinger/chargeDistribution.zip). It is quite remarkable that in addition to the existing voltage plateaus a third level is formed over the course of time. This specific pattern also appears in investigations of quantum systems, as discussed in chapter 3.

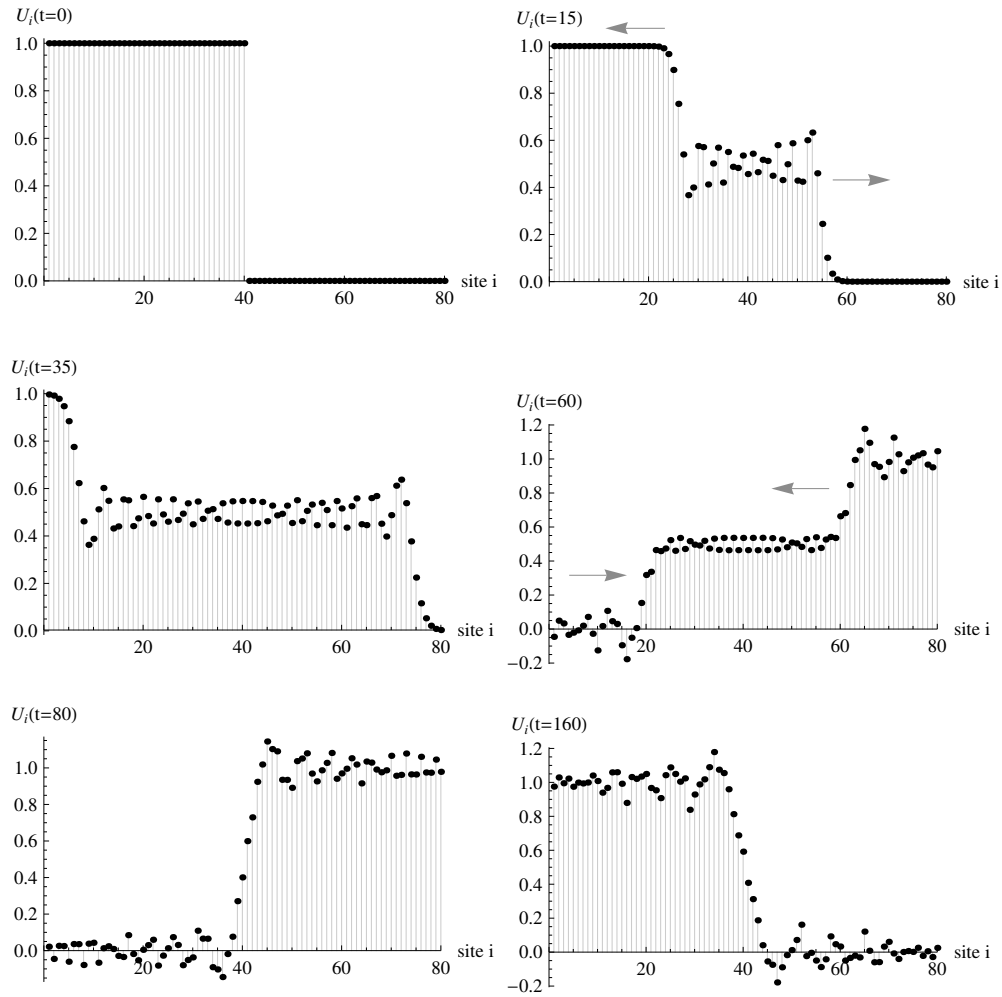


Figure 2.8. Onsite voltage distribution  $U_i(t)$  for  $t = 0, 15, 35, 60, 80$  and  $160$  and system size  $N = 80$ .  $L = C = 1$ . Shown are voltage drops at the  $i$ -th condensator with  $U_i(t) = Q_i(t)/C$ .

## 2.6 Final notes on the LC line

### 2.6.1 Setups

Instead of initially dividing the system into two halves with different charges  $Q_L$  and  $Q_R$ , we can distribute the charge carriers homogeneously over the chain, apply a temporally constant voltage ( $\phi_{0,L} - \phi_{0,R}$ ) and get the same result for the current as a function of time, which can be seen in equation (2.16) for  $b_k$ . The reason for this lies in the linear character of our model which thus behaves independently from the chosen setup. This is the main reason why we can not fully compare the LC line with a quantum system, since preparing the classical system in setup (II) gives the same outcomes as for setup (I), in contrast to the quantum simulation results in subsequent chapters.

### 2.6.2 Applying the FABE approach to rectangular signals

The following passage treats an important detail that arises during the derivation of equation (2.39): There seem to be different functions  $\eta_k$  which provide the same quasi-stationary value, for instance  $\sin(\frac{\pi(2k-1)}{2N})$ ,  $\cos(\frac{\pi(2k-1)}{2N})$  and  $\frac{\pi(2k-1)}{2N}$ , see figure 2.9. Accordingly, it seems to be a good idea to use the presented FABE approach even if the specific equation of a given rectangular curve is unknown.

Using a cosine- instead of a sine-function does not change the current-curve at all, since one obtains the same integral in [app. A.2] for  $I_\infty(t)$  with  $\eta = \cos(x)$ . Thus, the expression for the current in an infinitely large system, and therefore its stationary value, is unchanged. For  $\eta_k = \frac{\pi}{2N}(2k-1)$  one obtains the same quasi-stationary value and a similar behaviour with regular, decreasing oscillations. For some other trigonometric functions – such as the tangent – the shape of the current curve is not overshooting at the beginning anymore. Still, it seems as if the curve oscillates around the same stationary value. For polynomial expressions it is apparent that there must be at least a term of the order  $\mathcal{O}(k)$  to form a quasi-stationary part with the correct value, whereas one has to note that the prefactor of this term determines the quasi-stationary value itself. When the prefactors of higher order terms in  $k$  become to large, a pre-plateau is formed, for instance shown in the right bottom part of figure 2.9. When scaling  $N \rightarrow \infty$  the first plateau extends to infinity. One could expect that whenever two or more plateaus are visible, the value of the first plateau will be most likely the one against which the current converges for  $N \rightarrow \infty$ .

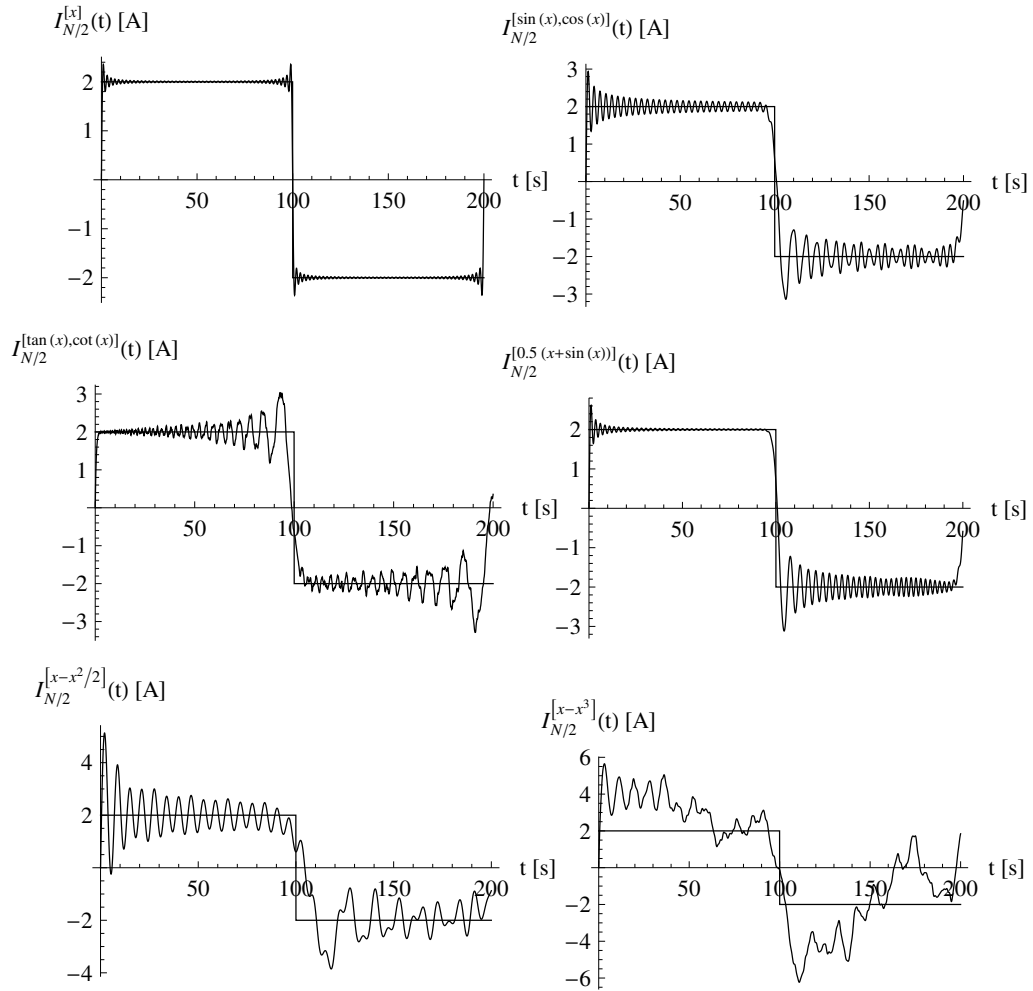


Figure 2.9. Current  $I_{N/2}^{[\eta_k]}(t)$  for different  $\eta_k$ . For reasons of clarity, the substitution  $x = \frac{(2k-1)\pi}{2N}$  with  $N = 100$  was used. The rectangular signal with the amplitude  $\pm 2$  in every plot is only a guide for the eyes.



## 2.7 Summary

In this chapter we have derived the description of currents for a finite and infinite  $LC$  line in case of an initial step distribution of the charges. We found explanations for several finite-size effects, such as the rectangular or the rapid oscillation and how the currents through two adjacent inductors cancel out. Using our analyses, we developed a Fourier transformation based method to extract the stationary current from outcomes of analyses of finite systems, which we simply call the FABE method for reasons of clarity.



## CHAPTER 3

### Non-equilibrium simulations

To understand finite-size and finite-time effects in quantum systems we investigate a system without electron-electron interaction. The great advantage of this model is that exact results from one-particle equation of motion calculations are available, see section 3.3, to test the TEBD method in chapter 4 and the FABE method for analysing the stationary current, which we presented in chapter 2.

#### 3.1 Tight-binding model

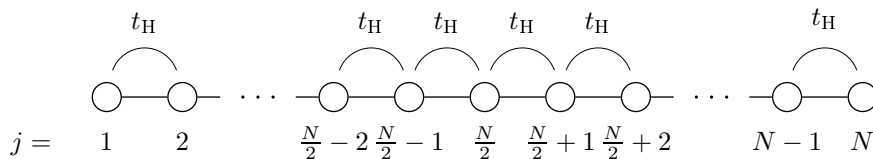


Figure 3.1. One-dimensional tight-binding model

In the following, we will focus on the one-dimensional tight-binding model without spin (figure 3.1) whose Hamiltonian is given by

$$H = H_0 + H_B \quad (3.1)$$

with

$$H_0 = -t_H \sum_{j=1}^{N-1} (c_j^\dagger c_{j+1} + c_{j+1}^\dagger c_j) \quad (3.2)$$

where  $t_H$  denotes the hopping amplitude between nearest-neighbor sites,  $c_j^\dagger, c_j$  denote the fermionic creation and annihilation operators and  $N$  is the system size. To drive the system out of equilibrium we use a step-like potential bias between the left- and right-hand halves of the chain

$$H_B = \frac{\Delta\epsilon}{2} \left( \sum_{j=1}^{N/2} n_j - \sum_{j=N/2+1}^N n_j \right) \quad (3.3)$$

with  $n_j = c_j^\dagger c_j$ . The potential energy step is set by  $\Delta\epsilon = |eV|$  where  $V$  is the voltage bias and  $e$  is the elementary charge. It is possible to use a smoother potential profile but the results for the stationary current using the FABE method are only slightly affected by the specific shape as long as the non-constant part in the middle is rather smooth and locally confined.

The tight-binding model originates from the LCAO idea and evolved from that in 1954 among others through the work of J. C. Slater and G. F. Koster [52]. Based on its provenance, the model describes electrons that are tightly bound to atoms in a solid. Per atom, only one atomic orbital is taken into account and the overlap of adjacent atomic wave functions is limited such that the electrons are rather localized and their transitions can be seen as ‘hopping’. Regarding its application, the tight-binding model is the basic lattice model on which more complicated models such as the spinless fermion model and the Hubbard model are based. It describes non-interacting free fermions on a (in our case one-dimensional) lattice that can hop from one site to adjacent sites with a hopping amplitude  $t_H$ . According to the Pauli principle only one electron per site is allowed.

Although electron-electron interactions are significant for the appearance of many quantum effects, they are not part of the tight-binding model. Nevertheless, the model has some of the ground state properties and describes many realtime effects that also appear in more complicated systems that include Coulomb interactions.

## 3.2 Setups

We employ two different setups to generate currents in the lattice models [42]. In the first one (I) we prepare the system at time  $t = 0$  in the ground state  $|\phi(\Delta\epsilon \neq 0)\rangle$  of the Hamiltonian  $H = H_0 + H_B$  (i.e. with potential bias), see figure 3.2. For later times  $t > 0$  we let the system evolve according to the Hamiltonian  $H_0$  (i.e. without potential bias)

$$|\psi(t > 0)\rangle = \exp\left(-i\frac{H_0 t}{\hbar}\right) |\phi(\Delta\epsilon \neq 0)\rangle. \quad (3.4)$$

This setup describes an inhomogeneous initial state with more particles in one half of the system than in the other one. Thus particles flow from one side to the other one for  $t > 0$ . It corresponds to a one-dimensional scattering experiment in which particles are emitted on one side of the system with energies between  $[-\Delta\epsilon/2, \Delta\epsilon/2]$ , scattered at the junction between both system halves, and then (partially) transmitted to the opposite side. This picture of transport through junctions is often used in theoretical investigations.

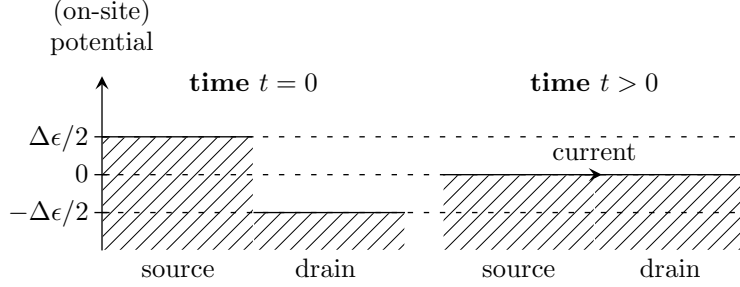


Figure 3.2. Setup (I): The charge reservoirs (two halves: source and drain) have different potentials but are coupled for  $t = 0$ . For  $t > 0$  the potential difference is set to  $\Delta\epsilon = 0$  instantaneously.

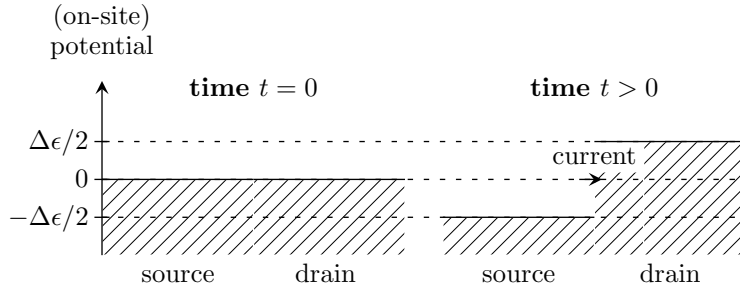


Figure 3.3. Setup (II): The charge reservoirs (two halves: source and drain) are in equilibrium and coupled for  $t = 0$ . For  $t > 0$  a potential difference  $\Delta\epsilon > 0$  is applied.

In the second setup (II) we prepare the system at time  $t = 0$  in the ground state  $|\phi(\Delta\epsilon = 0)\rangle$  of the Hamiltonian  $H_0$  (i.e., without potential bias). For later times  $t > 0$  the time evolution of the system is determined by the Hamiltonian  $H = H_0 - H_B$ , i.e. with a potential bias that causes the current to flow in the same direction as in setup (I)

$$|\psi(t > 0)\rangle = \exp\left(-i\frac{(H_0 - H_B)t}{\hbar}\right) |\phi(\Delta\epsilon = 0)\rangle. \quad (3.5)$$

Setup (II) describes the evolution of an initially homogeneous state under the influence of a potential gradient, see figure 3.3. Thus it corresponds more closely to the actual experimental situation with a voltage source generating a current in a conducting wire.

### 3.3 One-particle equation of motion

A one-dimensional chain in the tight-binding model can be described by the single particle reduced density matrix [53, 54]

$$\mathcal{G}_{ij}(t) = \langle \Psi(t) | c_i^\dagger c_j | \Psi(t) \rangle. \quad (3.6)$$

$|\Psi(t)\rangle = e^{-(i/\hbar)Ht} |\Psi_0\rangle$  denotes the wave function of the system at time  $t$ . If the initial state  $|\Psi_0\rangle$  is chosen to be the ground state of a tight-binding Hamiltonian, it is a Slater determinant

$$|\Psi_0\rangle = \psi_{i_1}^\dagger \psi_{i_2}^\dagger \dots \psi_{i_n}^\dagger |0\rangle \quad (3.7)$$

where  $|0\rangle$  is the vacuum state,  $\psi_{i_j}^\dagger$  the fermionic creation operator which creates a particle in the  $i_j$ -th eigenstate of the single particle Hamiltonian  $H^{(1)}$  and  $n$  is the total particle number. Local onsite creation operators  $c_i^\dagger$  can be written as

$$c_i^\dagger = \sum_{k \in \mathfrak{J}_{\Psi_0}} \Psi_{k,i}^* \psi_k^\dagger \quad (3.8)$$

with the  $k$ -th eigenstate  $\Psi_{k,l}$  of  $H^{(1)}$  in the local basis. The index set  $\mathfrak{J}_{\Psi_0}$  contains all indices of occupied single particle states in  $\Psi_0$ . The initial single particle reduced density matrix  $\mathcal{G}^0 = \mathcal{G}(t=0)$  is given by

$$\begin{aligned} \mathcal{G}_{ij}^0 &= \sum_{k,q=1}^N \Psi_{k,i}^* \Psi_{q,j} \langle \Psi_0 | c_k^\dagger c_q | \Psi_0 \rangle \\ &= \sum_{k \in \mathfrak{J}_{\Psi_0}} \Psi_{k,i}^* \Psi_{k,j} \end{aligned} \quad (3.9)$$

since  $\langle \Psi_0 | c_k^\dagger c_q | \Psi_0 \rangle = 1$  only for  $k = q$  and only if the  $k$ -th single particle state is occupied in  $\Psi_0$ . Preparing the ground state for half-filling at zero temperature means that  $\mathfrak{J}_{\Psi_0}$  contains the indices of all eigenstates of  $H^{(1)}$  with an eigenenergy smaller than or equal to zero.

The time evolution is given by the one-particle equation of motion

$$\frac{d}{dt} \mathcal{G}(t) = \frac{i}{\hbar} [H_{t>0}^{(1)}, \mathcal{G}(t)] \quad (3.10)$$

where  $H_{t>0}^{(1)}$  denotes the single particle Hamilton matrix of size  $N \times N$  with which the system is evolved in time. More precisely  $H_{t>0}^{(1)}$  is the one-particle representation of  $H_0$  or  $H_0 + H_B$  depending on the specific setup. Since it is time-independent, the solution of the differential equation (3.10) is given by

$$\mathcal{G}(t) = \exp\left(-\frac{i}{\hbar} H_{t>0}^{(1)} t\right) \mathcal{G}^0 \exp\left(\frac{i}{\hbar} H_{t>0}^{(1)} t\right). \quad (3.11)$$

Defining  $H^d$  as  $H_{t>0}^{(1)}$  in its eigenbasis, it holds

$$H_{t>0}^{(1)} = z H^d z^\dagger \quad (3.12)$$

where the columns of  $z$  are the eigenvectors of  $H_{t>0}^{(1)}$  and  $H^d$  contains the corresponding eigenvalues in its diagonal entries.  $\mathcal{G}(t)$  is then evolved in time with

$$\mathcal{G}(t) = \left[ z \exp\left(-\frac{i}{\hbar} H^d t\right) z^\dagger \mathcal{G}^0 z \exp\left(\frac{i}{\hbar} H^d t\right) z^\dagger \right]. \quad (3.13)$$

Consequently, the dynamics of a tight-binding chain can be computed numerically without additional truncation error with a runtime of  $\mathcal{O}(N^3)$  for any point in time. The particle number expectation values are equal to the diagonal terms of the reduced density matrix

$$\langle n_k(t) \rangle = \langle \Psi(t) | c_k^\dagger c_k | \Psi(t) \rangle = \mathcal{G}_{kk}(t) \quad (3.14)$$

and the expectation value for the current operator

$$j_k = i \frac{et_H}{\hbar} \left( c_k^\dagger c_{k+1} - c_{k+1}^\dagger c_k \right) \quad (3.15)$$

from site  $k$  to  $k+1$  can be calculated with the off-diagonal entries

$$\langle j_k(t) \rangle = i \frac{et_H}{\hbar} [\mathcal{G}_{k,k+1}(t) - \mathcal{G}_{k+1,k}(t)]. \quad (3.16)$$

For a given (time-dependent) quantum state we define the current flowing between both halves of the system (figure 3.1) as the expectation value of the current operator for the site pair in the middle of the system

$$J(t) = \langle j_{N/2} \rangle. \quad (3.17)$$

We note that

$$J(t) = -\frac{d}{dt} Q_L(t) = \frac{d}{dt} Q_R(t) \quad (3.18)$$

where

$$Q_L(t) = -e \sum_{k=1}^{N/2} \langle n_k \rangle \quad \text{and} \quad Q_R(t) = -e \sum_{k=N/2+1}^N \langle n_k \rangle \quad (3.19)$$

are the (time-dependent) charges in the left- and right-hand halves of the chain, respectively. As the number of particles  $n_p$  is conserved, it holds

$$Q_L(t) + Q_R(t) = -e \cdot n_p = \text{const.} \quad (3.20)$$

The stationary current is a constantly flowing current in an infinitely large system after the settling time

$$\bar{J} = \lim_{t \rightarrow \infty} \lim_{N \rightarrow \infty} J(t). \quad (3.21)$$

If not otherwise specified,  $t_H = 1$  for all numerical simulations and, if units are not given explicitly,  $e = \hbar = 1$ . With the single-particle density matrix (3.6) and the time evolution (3.13), we have implemented a program using the Matlab framework, which is capable of simulating for instance a system of size  $N = 1000$  for a full period of the oscillating rectangular current within a couple of minutes on a single core processor. For the simulations performed in chapter 8 we have additionally extended this program to work for two-dimensional systems. Thus, the program serves well for performing fast and accurate simulations on tight-binding structures, giving us the possibility to compare our TEBD outcomes with numerically exact results for non-interacting cases in the following chapters.

Generally, currents (3.17) calculated with the states (3.4) and (3.5) are different. In the strong-bias limit  $|\Delta\epsilon| \gg t_H$  one can show [app. B.1] that the steady-state current remains finite for the first setup while it vanishes for the second one. Recently, it has been reported that initial conditions (quenching an interaction term or a tunneling term) can also alter the steady-state current flowing through a quantum point contact between two TLL leads which have been driven out of equilibrium by an external bias [55]. In the weak-bias limit  $|\Delta\epsilon| \ll t_H$ , however, a simple perturbation calculation shows that both setups yield the same linear response for the stationary current in the spinless fermion model and the Hubbard model [app. B.1]. Thus in this regime both setups can be used indifferently but in the non-linear regime we must distinguish them. For non-interacting fermions in setup (I), the  $I$ - $V$  curve is known exactly [15, 56]

$$\begin{aligned} \bar{J} &= (e/h)\Delta\epsilon \quad \text{for } |eV| \leq 4t_H, \\ \bar{J} &= (e/h)4t_H \quad \text{for } |eV| \geq 4t_H \end{aligned} \quad (3.22)$$

with  $\Delta\epsilon = |eV|$  where  $V$  is the voltage bias.

In most theoretical studies the potential bias switching is not instantaneous, but adiabatic. This can also be used in numerical simulations, for instance, see [32, 36]. Our tests do not reveal any significant differences for the steady-state current depending on the switching rate as long as the potential changes in a time scale which is much smaller than the time scale associated with the motion of particles from one reservoir to the other one. Since the FABE method (presented in chapter 2) is designed to work with an instantaneous change in the potential difference and as numerical simulations are simpler with it, we prefer this approach.



## 3.4 Finite-size effects and stationary current

### 3.4.1 Finite-size induced oscillation

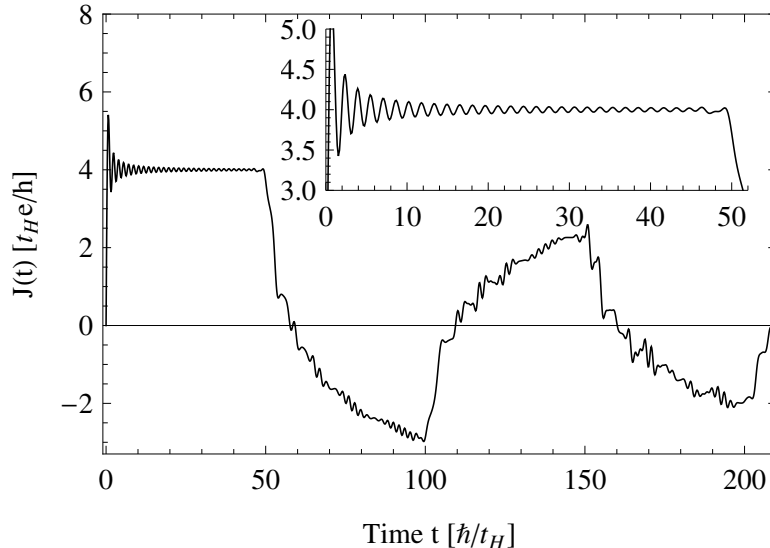


Figure 3.4. Current in the tight-binding model with size  $N = 100$  for a long time scale, calculated using the one-particle equation of motion and setup (I). The initial state was prepared with a completely filled left half, a completely empty right half and  $t_H = 0$  for all bonds.

With both setups (I) and (II) one observes qualitatively similar currents in the tight-binding model as a function of time, see figure 3.4. First, there is a small transient regime for  $t < t_a \lesssim 3h/t_H$  with very rapid and dominant small oscillations. For long times  $t > t_b \gg T^{\max}$  the current becomes very irregular because of the progressive dephasing of moving particles. Between  $t_a$  and  $t_b$  we observe an approximately rectangular wave with a period  $T^{\max}$  which diverges with increasing system length (the corresponding leading frequency  $\omega^{\max} = 2\pi/T^{\max}$  converges towards 0 in the thermodynamic limit). The period of the rectangular oscillation is given by [app. B.2]

$$T^{\max} \approx \hbar \cdot \frac{N}{t_H} \quad \text{for } N \gg 1. \quad (3.23)$$

Using a semi-classical picture, particles first flow from one side of the system to the opposite side because of the inhomogeneous density (first setup) or

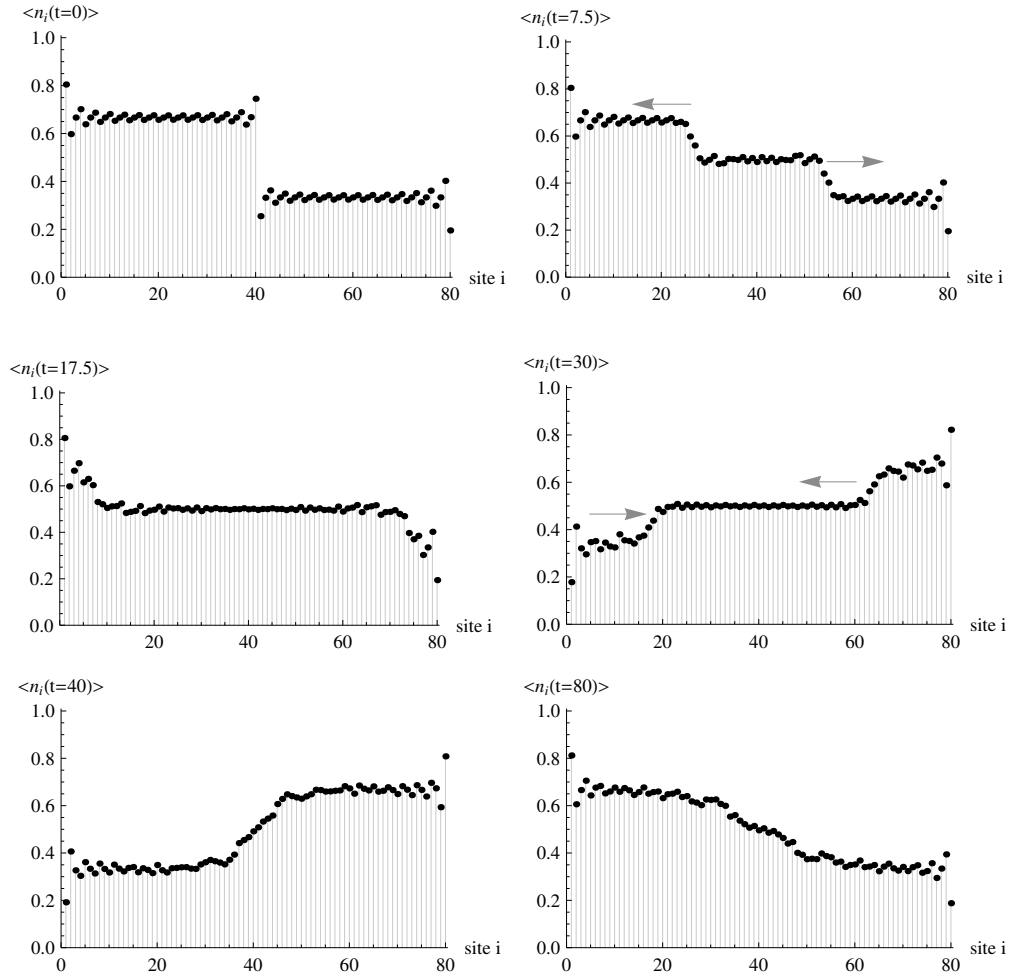


Figure 3.5. Setup (I): Particle density distributions for times  $t = 0, 7.5, 17.5, 30, 40$  and  $80$  in units of  $\hbar/t_H$ . The initial state has been prepared with  $|\Delta\epsilon| = 2t_H$  and the system size is  $N = 80$ .

the potential difference (second setup). In the first setup, they are reflected by the hard wall represented by the chain edge. As there is no dissipation in our model, all reflected particles flow back with the same velocity in the opposite direction until they reach the other chain edge and are again reflected and so on. Figure 3.5 shows the particle densities at different times. A similar behaviour of the time evolution of the density distribution has already been observed for instance in the spin  $\frac{1}{2}$   $XXZ$  chain [57, 58], which is

closely related to the spinless fermion model which is studied in chapter 5. We also note that the same behaviour is generally observed in the Hubbard model for which the time evolution of the particle densities for a system of size  $N = 60$  in setup (I) with  $\Delta\epsilon = 1.2t_H$  and  $U_H = 2t_H$  can be seen at [whypsi.com/einhellinger/hubbardDistribution.zip](http://whypsi.com/einhellinger/hubbardDistribution.zip). One can see the close connection to the charge distributions of the  $LC$  line in figure 2.8. In the second setup it is basically the same effect, but since the potential bias is still present after the first half oscillation, the particles are scattered on their way back, and the oscillation amplitude is damped. The concrete behaviour can be seen in the current curve and particle density distributions for setup (II) in figure 3.6. The current oscillates around zero but only a small change in the particle density distribution generates this current (see the last two density plots for  $t = 150$  and  $t = 250$  in figure 3.6). For higher potential differences the remaining oscillation in the current curve becomes smaller, tending to zero for a very high voltage.

The progressive degradation of the rectangular signal for both setups can be understood using the same semi-classical picture. First, all particles flow in the same direction but, as they have different velocities, they progressively come out of phase. For long times  $t \gg t_b$ , which can be checked up to the numerical double limit  $t \approx 10^{300}\hbar/t_H$ , our simulations using the one-particle equation of motion show that the current does not go to zero but continues to oscillate with a period  $T^{\max}$ . This can be understood in the picture of the classical  $LC$  line as well as for the tight-binding model through the dominant amplitude of the  $\omega^{\max}$  oscillation. It is basically the same effect as if all contributions to a series representation of a square wave (2.37) would ‘randomly’ come out of phase. In that case, the contribution with the lowest frequency  $\omega^{\max}$ , which is the frequency of the rectangular oscillation, determines the frequency of the remaining irregularly shaped curve.

### 3.4.2 Rapid oscillation on top of the square wave

Setting the expression (2.22) for the period of the classical system and equation (3.23) for the period of the quantum system equal, one gets

$$t_H \approx \frac{\hbar}{2\sqrt{LC}} \quad \text{for } N \gg 1. \quad (3.24)$$

Further comparison with equation (2.36) gives for the period of the rapid oscillation

$$T^{\min} = \pi\sqrt{LC} \approx \frac{h}{4t_H} \quad \text{for } N \gg 1. \quad (3.25)$$

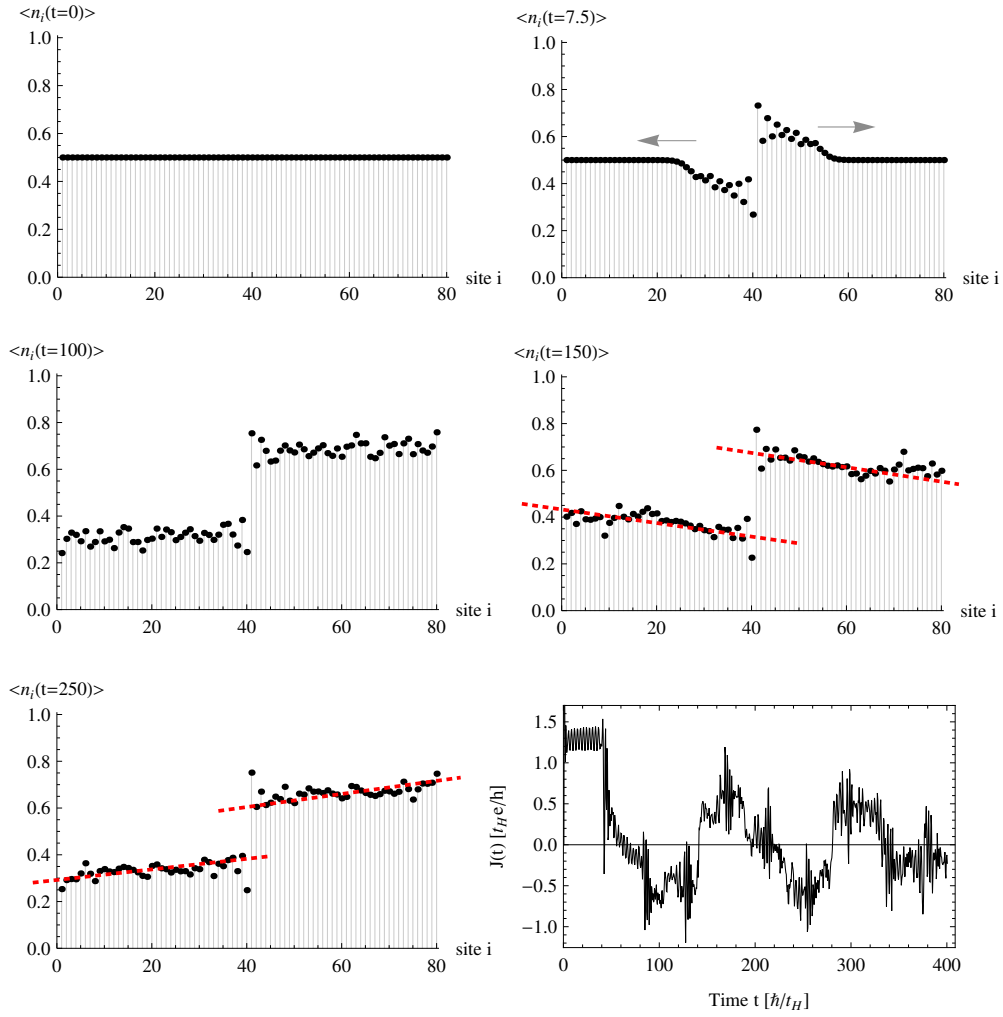


Figure 3.6. Setup (II): Particle density distributions for times  $t = 0, 7.5, 100, 150, 250$  in units of  $\hbar/t_H$  and the current for a long time scale for a system of size  $N = 80$ . The realtime evolution was performed with  $|\Delta\epsilon| = 2t_H$ . The dashed red lines in the density plots for  $t = 150$  and  $t = 250$  clarify the difference in the particle densities which feeds the oscillating current.

Instead of preparing the system in a ground state of a Hamiltonian with applied potentials, one can initially decouple all sites and fill the left half of the system with (uncorrelated) particles, leaving the right half empty. This almost corresponds to choosing  $\Delta\epsilon = 4t_H$ , insofar as a ground state with

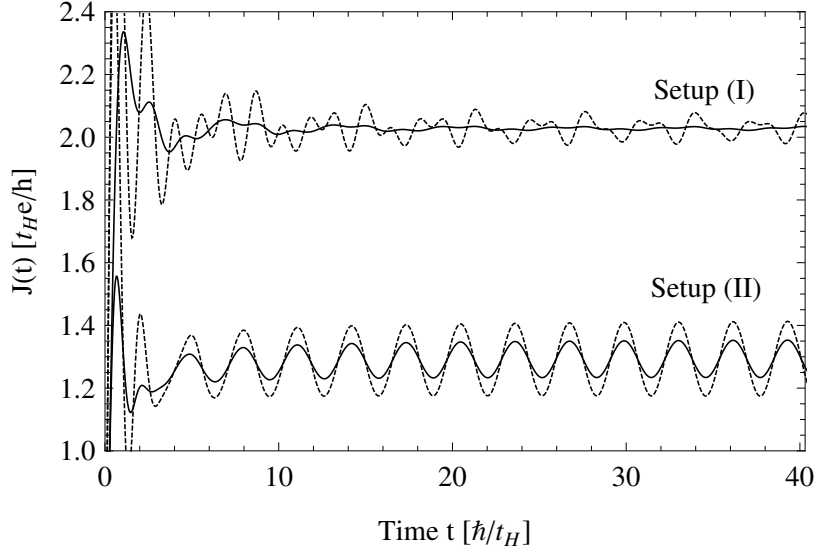


Figure 3.7. Current in the tight-binding model for  $\Delta\epsilon = 2t_H$ , calculated using the one-particle equation of motion. The dashed lines are currents through a single bond in the chain while the solid ones represent the mean value of the currents through two adjacent bonds in the middle.

this applied voltage and coupled reservoirs still has some correlations and unequally distributed onsite particle densities in it. The resulting current curve in figure 3.4 in the first half period closely resembles the curve shown in figure 2.2 for the *LC* line.

The magnification in figure 3.4 shows a rapid oscillation with a period according to equation (3.25), in contrast to the oscillation shown in figure 3.7 for setup (I) which is ‘disturbed’ by oscillations stemming from correlations and an unequal distribution of particles in the ground state due to a lower applied voltage  $\Delta\epsilon < 4t_H$ . Although the oscillation in figure 3.7 for setup (II) is very regular, it does not stem from the same ‘classical’ origin, which is confirmed by the facts that on the one hand two adjacent currents do not cancel out and on the other hand the oscillation does not fulfill equation (3.25).

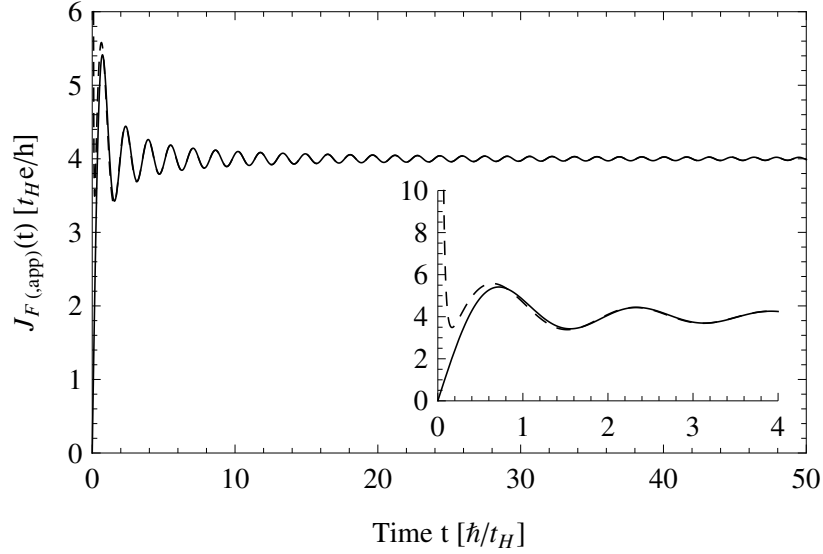


Figure 3.8. Solid line:  $J_{\text{F}}(t)$  from equation (3.27), dashed line: corresponding approximation  $J_{\text{F,app}}(t)$  from (3.28).

### 3.4.3 Applicability of the FABE approach to quantum systems

Although we have seen the close connection between the tight-binding system for initially uncorrelated particles and the classical  $LC$  line, there exists a major difference in the behaviour of the respective currents: the damping of the rapid oscillations. While for the classical  $LC$  line a  $\mathcal{O}(t^{-\frac{1}{2}})$  dependence of the amplitudes according to equation (2.29) is predicted, this decrement is different for a quantum system. The expectation value of the current for setup (I) and for initial conditions like in figure 3.4 (one completely filled and one completely empty half) is for  $N \rightarrow \infty$  given by [15, 56]

$$J_{\text{F}}^k(t) = \frac{2et_{\text{H}}}{\hbar} \sum_{l=k-\frac{N}{2}}^{\infty} \mathcal{J}_l(\omega t) \mathcal{J}_{l+1}(\omega t) \quad (3.26)$$

where  $k$  denotes the site,  $\omega = 2t_{\text{H}}/\hbar$  and  $\mathcal{J}_l(z)$  are the Bessel functions of the first kind and the expression can be simplified to [app. B.3]

$$J_{\text{F}}(t) = \frac{et_{\text{H}}}{\hbar} \omega t [(\mathcal{J}_0(\omega t))^2 + (\mathcal{J}_1(\omega t))^2]. \quad (3.27)$$

Using the asymptotic series expansions (A.15) yields for the current

$$J_{\text{F,app}}(t) = \frac{et_{\text{H}}}{16h(\omega t)^2} [5 - 32\omega t \cos(2\omega t) + 4 \sin(2\omega t)] + \frac{4et_{\text{H}}}{h} \quad (3.28)$$

which is plotted together with expression (3.27) in figure 3.8. The curve highly coincides with the one shown in figure 3.4 for  $t < T^{\text{max}}/4$  which confirms the assumption that the borders in the finite quantum system for setup (1) only significantly change the current after a time  $T^{\text{max}}/4$ , determined by the velocity of the particle density front wave [56] which moves from the middle of the chain to the borders. The quasi-stationary value from (3.28) is given by  $\bar{J} = 4et_{\text{H}}/h$  and the amplitudes of the rapid oscillation are damped with  $\mathcal{O}(1/t)$ . Moreover, expression (3.25) for the period of the rapid oscillation – which was derived only by comparison with the classical model – is confirmed by equation (3.28).

Since the latter analysis shows a  $\mathcal{O}(1/t)$  damping of the rapid oscillation, the open question at hand is, if it is reasonable to use the FABE method for a quantum system. In fact, a pure square wave described by its Fourier series (2.37) has also a damping of the rapid oscillation of  $\mathcal{O}(1/t)$  and highly resembles the current described by (3.27) or depicted in figure 3.4 when choosing an appropriate amplitude and number of harmonics. Since the mathematical error (2.45) of our method stems from the difference of the analyzed curve to a square wave, the FABE approach provides an even smaller error than (2.45) for a quantum system prepared in setup (I).

In contrast, the rapid oscillation of the current in a quantum system prepared with setup (II) has an unknown behaviour and it seems uncertain if correct results can be obtained using outcomes from simulations of finite systems and the FABE method. However, figures 3.9 and 3.10 show that the computed stationary values do not significantly change for system sizes larger than  $N \approx 60$ . The scaling behaviour for setup (I) can be seen in figure 3.11 and confirms the good applicability of our method also for smaller potential differences  $\Delta\epsilon$ . Remarkably, the curve for setup (I) approaches the limit value from above while the curves for setup (II) converge coming from below the limit values.

The curve in figure 3.11 for  $\Delta\epsilon = 4t_{\text{H}}$  converges against  $4t_{\text{H}}e/h$  as expected according to equation (3.28). The other curve in that figure for  $\Delta\epsilon = 2t_{\text{H}}$  has the limit value  $2t_{\text{H}}e/h$  as expected according to equation 3.22 and the curve in figure 3.9 converges against zero. An exact result for  $\Delta\epsilon = 2t_{\text{H}}$  and setup (II) is not available. All curves have a deviation from the mentioned values of less than  $10^{-7}t_{\text{H}}e/h$  for  $N \geq 70$ . Figures 3.9, 3.10 and 3.11 emphasize

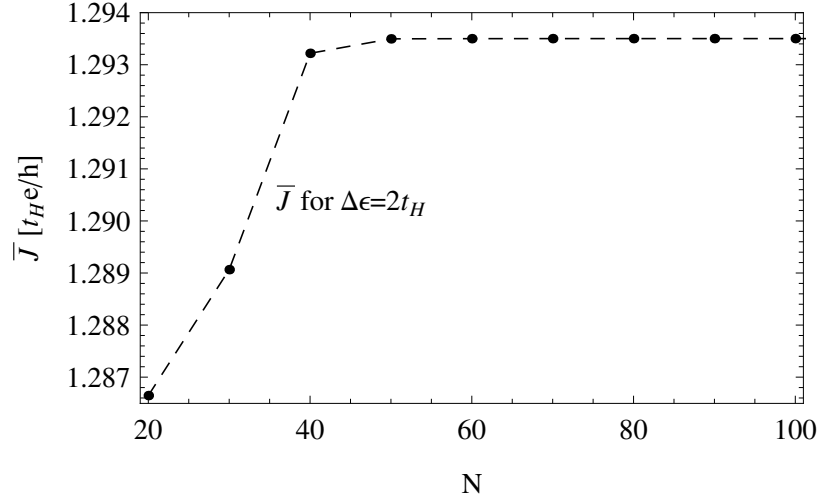


Figure 3.9. Stationary currents  $\bar{J}$  for **setup (II)** and  $\Delta\epsilon = 2t_H$ , calculated using the presented FABE method and different system sizes. The dashed lines are guides for the eyes.

that an extrapolation of the results obtained from the FABE method is not necessary for sufficiently high system size  $N$ . Thus, in the following chapters we can use a system size  $N = 100$  for the simulations and directly apply the FABE method to our simulation results.

### 3.5 Summary

In this chapter we have shown the close connection of the *LC* line and the tight-binding model by comparing model parameters and the behaviour of charge and particle density distributions, respectively. Furthermore, we implemented a one-particle equation of motion method. We explained the rapid oscillation in the tight-binding model on the one hand by comparison with the classical model and on the other hand by using the results from [15, 56]. Finally we showed the general applicability of the FABE approach to quantum systems and argued that an extrapolation of the stationary current values obtained by our approach is unnecessary for sufficiently high system sizes.



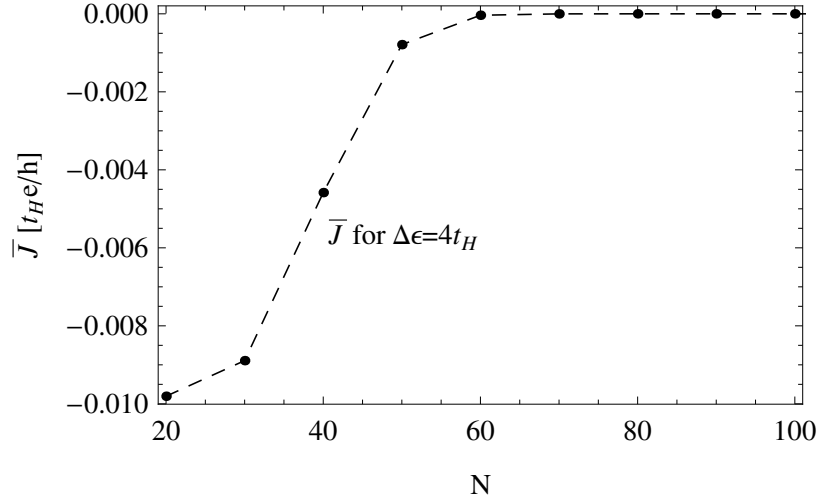


Figure 3.10. Stationary currents  $\bar{J}$  for **setup (II)** and  $\Delta\epsilon = 4t_H$ , calculated using the presented FABE method and different system sizes. The dashed lines are guides for the eyes.

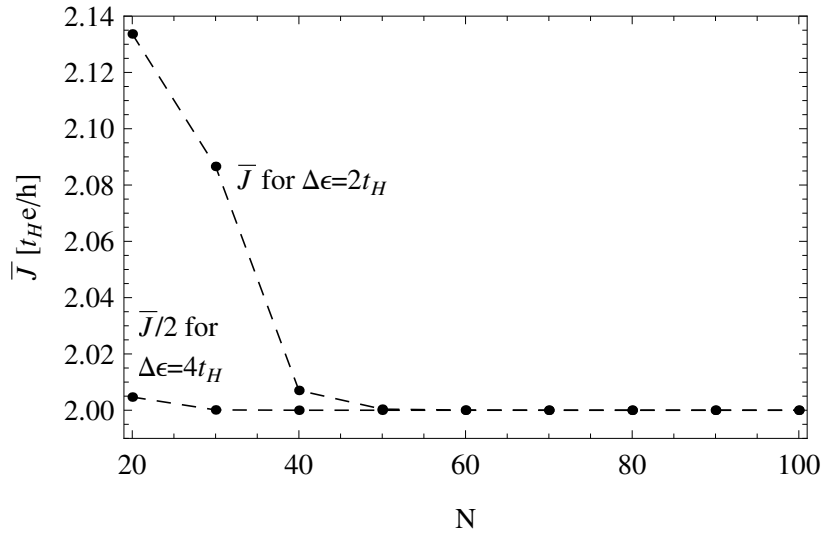


Figure 3.11. Stationary currents  $\bar{J}$  for **setup (I)** and for  $\Delta\epsilon = 2t_H$  and  $\Delta\epsilon = 4t_H$ , calculated using the presented FABE method and different system sizes. The values for  $\Delta\epsilon = 4t_H$  have been divided by 2, regarding a better comparability of the two curves. The dashed lines are guides for the eyes.



## CHAPTER 4

### TEBD method

In this chapter we introduce the time evolving block decimation (TEBD) method for the simulation of systems with electron-electron interaction. We especially use this method for simulating the spinless fermion model and the Hubbard model in chapters 5 and 6. In chapters 7 and 8 the method is extended and applied to a two-site fermionic system coupled to a bosonic bath and a tight-binding ladder. The TEBD method has been invented in 2003 by Guifré Vidal [25, 26]. The algorithm is based on a specific representation of quantum states by matrix product states (MPS) and it was the first MPS-based procedure allowing efficient realtime simulations of interacting quantum systems. For an  $N$ -site lattice an MPS is generally written

$$\begin{aligned}
 |\Psi\rangle = & \sum_{\{j_k\}} \Gamma^{[1]j_1} \lambda^{[1]} \Gamma^{[2]j_2} \lambda^{[2]} \dots \\
 & \dots \Gamma^{[N-1]j_{N-1}} \lambda^{[N-1]} \Gamma^{[N]j_N} |j_1 j_2 \dots j_N\rangle
 \end{aligned} \tag{4.1}$$

where  $|j_1 j_2 \dots j_N\rangle$  designs the states of the occupation number basis,  $\lambda^{[k]}$  ( $k = 1, 2, \dots, N - 1$ ) are positive definite diagonal matrices and  $\Gamma^{[k]j_k}$  ( $k = 1, 2, \dots, N$ ) are matrices satisfying orthogonality conditions

$$\begin{aligned}
 \sum_{j_k} (\Gamma^{[k]j_k})^\dagger (\lambda^{[k-1]})^2 \Gamma^{[k]j_k} &= I, \\
 \sum_{j_k} \Gamma^{[k]j_k} (\lambda^{[k]})^2 (\Gamma^{[k]j_k})^\dagger &= I.
 \end{aligned} \tag{4.2}$$

Sums over an index  $j_k$  run over a complete basis of the site  $k$ , for instance 2 states for the spinless fermion model and 4 states for the Hubbard model. Every quantum state of the Fock space associated with a finite lattice can be represented exactly in this form if the matrix dimensions can be as large as the square root of the Fock space dimension, for instance  $2^{N/2}$  for the spinless fermion model and  $4^{N/2}$  for the Hubbard model. In numerical computations, however, the matrix dimension must be kept smaller than a relatively small upper limit  $\chi_c$  (Schmidt dimension). Fortunately, for many one-dimensional systems this truncation is possible and can lead to a dramatic computational

speedup while keeping the error in computed observables conveniently low. This is done by using the Schmidt decomposition of the density matrix at each bond to calculate the matrices  $\lambda^{[k]}$  from its eigenvalues and the  $\Gamma^{[k]j_k}$  from its eigenvectors. For a bipartite split at bond  $k$ , the Schmidt decomposition is defined by

$$|\Psi\rangle = \sum_{\alpha_k=1}^{\chi_k} \lambda_{\alpha_k} |\Phi_{\alpha_k}^{[1..k]}\rangle |\Phi_{\alpha_k}^{[k+1..N]}\rangle. \quad (4.3)$$

The vectors  $|\Phi_{\alpha_k}^{[1..k]}\rangle$  are the eigenvectors of  $\rho^{[1..k]}$ , the reduced density matrix of the left side of the split, the  $|\Phi_{\alpha_k}^{[k+1..N]}\rangle$  correspondingly the eigenvectors of  $\rho^{[k+1..N]}$  for the right side and the  $\lambda_{\alpha_k}^2$  are the eigenvalues of both  $\rho^{[1..k]}$  and  $\rho^{[k+1..N]}$ , with

$$\lambda_{\alpha_k} \geq 0 \quad \text{and} \quad \sum_{\alpha_k=1}^{\chi_k} \lambda_{\alpha_k}^2 = 1. \quad (4.4)$$

The  $\lambda_{\alpha_k}$  are the matrix elements  $(\lambda^{[k]})_{\alpha_k}$  and either of the  $|\Phi_{\alpha_k}\rangle$  can be used to build the matrices  $\Gamma^{[k]j_k}$  from equation (4.1). Thus, it is possible to keep only the largest  $\chi_c$  eigenvalues and throw away the rest while re-normalizing the state, such that the sum of the discarded values is smaller than an arbitrary error  $\epsilon$

$$\sum_{\alpha_k=\chi_c}^{\chi_k} \lambda_{\alpha_k}^2 < \epsilon. \quad (4.5)$$

The best candidates are states for which the Schmidt dimension, and hence the dimension of the MPS matrices is low (like product states), or states for which the Schmidt coefficients show an exponential decay, such that a large number of eigenvalues can be discarded without significant information loss.

The great advantage of the TEBD algorithm is the possibility to compute the time evolution of a state using a time-dependent Hamiltonian

$$|\Psi(t + \delta t)\rangle = e^{-\frac{i}{\hbar}H(t)\delta t} |\Psi(t)\rangle. \quad (4.6)$$

In a numerical implementation,  $\delta t$  has to be discrete, such that the total simulation time  $\tau = n_t \cdot \delta t$ , where  $n_t$  is the number of time steps and  $\delta t$  the numerical time step. The time evolution can be used as well to calculate the ground state  $|\psi_{\text{gs}}\rangle$  of a Hamiltonian  $H$ . This is done by taking the time to be imaginary and projecting (effectively ‘cooling’) a starting state  $|\psi_{\text{P}}\rangle$  to the ground state of  $H$

$$|\psi_{\text{gs}}\rangle = \lim_{\tau \rightarrow \infty} \frac{e^{-H\tau} |\psi_{\text{P}}\rangle}{\|e^{-H\tau} |\psi_{\text{P}}\rangle\|}. \quad (4.7)$$

For a one-dimensional system of size  $N$  with nearest-neighbour interaction

$$H_N = \sum_{l=1}^N K_1^{[l]} + \sum_{l=1}^N K_2^{[l,l+1]} \quad (4.8)$$

one can split the Hamiltonian into two sums  $H_N = F + G$  over even and odd sites, with

$$\begin{aligned} F &= \sum_{\text{even } l} (K_1^{[l]} + K_2^{[l,l+1]}) = \sum_{\text{even } l} F^{[l]}, \\ G &= \sum_{\text{odd } l} (K_1^{[l]} + K_2^{[l,l+1]}) = \sum_{\text{odd } l} G^{[l]}. \end{aligned} \quad (4.9)$$

Using the Suzuki-Trotter decomposition for exponential operators

$$\begin{aligned} e^{-\frac{i}{\hbar}H\delta t} &= e^{-\frac{i}{\hbar}(F+G)\delta t} \\ &= e^{-\frac{i}{\hbar}\frac{F}{2}\delta t} e^{-\frac{i}{\hbar}G\delta t} e^{-\frac{i}{\hbar}\frac{F}{2}\delta t} + \mathcal{O}(\delta t^3), \end{aligned} \quad (4.10)$$

we can reduce the process of time evolution to the successive application of operators which act only on two sites

$$\begin{aligned} e^{-\frac{i}{\hbar}\frac{F}{2}\delta t} &= \prod_{\text{even } l} e^{-\frac{i}{\hbar}\frac{F}{2}^{[l]}\delta t}, \\ e^{-\frac{i}{\hbar}G\delta t} &= \prod_{\text{odd } l} e^{-\frac{i}{\hbar}G^{[l]}\delta t}. \end{aligned} \quad (4.11)$$

The TEBD algorithm then updates the MPS representation by calculating the new Schmidt decomposition at the corresponding bond each time after a two-site operator is applied to it. This succession of two-site operators imposes a linear dependence of the computational cost on the system size  $N$ . Each time a Schmidt decomposition is computed, we can truncate the dimension of the MPS by keeping only a maximal number of eigenvalues  $\chi_c$ , which is necessary, since the computational cost of both Schmidt decomposition and update of the MPS representation is of the order  $\mathcal{O}(\chi_c^3)$  as shown in [25, 26].

## 4.1 Parallelization

The total (single core) CPU time used to obtain the results in this thesis amounts to approximately four million hours. Even though many concurrent simulations have been performed, this thesis would have not been realizable in the given time with a serial TEBD method. Accordingly, a parallel (i.e. multi-threaded) version of the TEBD algorithm has been developed and optimized to run on SMP machines with up to 150 CPU cores. These computational resources have been provided by the Regional Computing Center for Lower Saxony at the Leibniz Universität Hannover (RRZN).

The basic scheme according to which a serial TEBD performs the updates of the MPS representation is

```

t ← 0
while (not simulation finished) {
  for (l = 2 : 2 : N - 1) // l even
    call TEBDl;
  for (l = 1 : 2 : N - 1) // l odd
    call TEBDl;
  for (l = 2 : 2 : N - 1) // l even
    call TEBDl;
  compute expectation values (e.g. current)
  t ← t + dt
}

```

(4.12)

where  $\text{TEBD}_l$  updates the  $l$ -th bond and is defined in [app. (C)]. The alternate updating of even and odd sites according to (4.11) makes the TEBD algorithm highly parallelizable since one can execute every call of  $\text{TEBD}_l$  in one for-loop simultaneously using  $N/2$  threads. However, it is very important to use a well-suited synchronization scheme to get a low overhead and low waiting time of the threads. The diagram in figure 4.1 shows a simplified version of the process of one update of all bonds. In fact, even more threads are started and they are specialized on different tasks, but the level of detail of this scheme is high enough to show the low overhead that a multi-threaded TEBD algorithm produces.

All threads start with even bonds and as soon as a thread has finished, it updates the next available odd or even bond if its two neighbors have already been updated. This procedure is continued until all bonds have been processed according to the scheme (4.12). The threads then wait for all others to finish, i.e. they wait at a so-called barrier. When all threads are

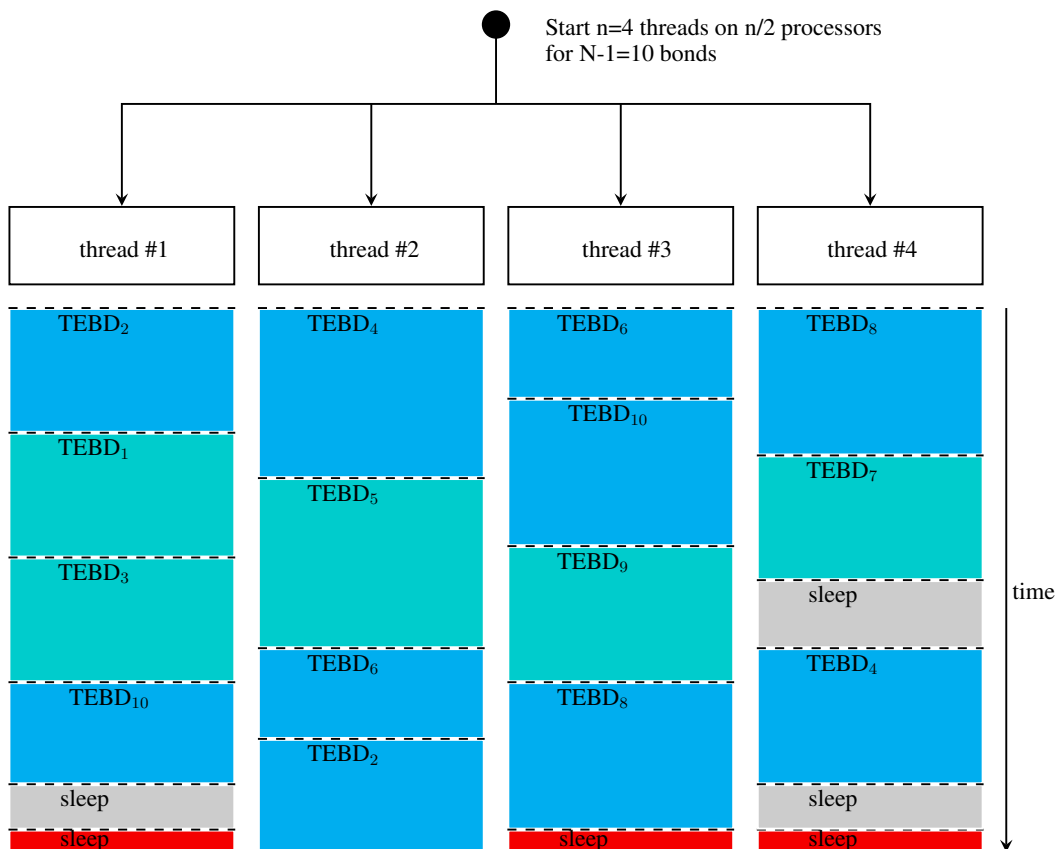


Figure 4.1. Single iteration of the outer while-loop of a parallel TEBD according to the serial scheme (4.12). Only during ‘red’ phases a significant loss in parallelization occurs.

available, the desired expectation values are computed and the procedure starts again from the beginning. In fact, twice as much threads are started than processors (cores) are available. The operating system switches from thread to thread which causes only a small overhead if not much memory is used in every thread, which ought to be transferred between cache and RAM. Accordingly, it is important to organize a thread such that always the minimal amount of private memory (local variables) is allocated. Also note that a waiting (sleeping) thread needs almost no CPU time.

One can see gray and red ‘sleep’ times in figure 4.1. Even while threads are waiting (gray sleep phases), as long as at least as much threads are working as processors are available, the operating system will split the CPU time over the remaining threads. Only during red sleep phases a significant loss

in parallelization occurs, which in the given example means that only half of the cores are used.

The implemented multi-threaded version of TEBD has an extremely low overhead with less than 1% for 10 processors (cores) and less than 10% for up to 150 processors (cores). The TEBD method has been implemented in C++, using pthreads for multi-threading, a self-written synchronization (barrier) scheme and stack system. Since the LAPACK package in its most recent version is not thread-safe, Intel's MKL library has been used for the diagonalization of the density matrix  $\rho^{(R)}$ , see [app. C]. The overall cost of a TEBD simulation is slightly higher than that of a DMRG calculation on a single processor. If several processors are used in parallel, the overhead of DMRG calculations become rapidly prohibitive, exceeding 100% for as few as 4 processors [40]. Thus, our TEBD implementation is already twice as fast as DMRG for 4 processors and the difference is likely to increase rapidly with the number of processors.

## 4.2 Error sources

One obvious error source is the one stemming from the discretization of time in order to numerically compute equation (4.6). Therefore, it is necessary to keep the actual time step  $\delta t$  small enough to have a good approximation of  $H(t)$  in the interval  $[t, t + \delta t]$ . However, the main error sources in the algorithm are the Suzuki-Trotter approximation and the Schmidt truncation. In order to improve the time step error, one can use higher-dimensional Suzuki-Trotter formulas, at a computational cost which scales linearly with higher-order approximations [59], or we can decrease the time step  $\delta t$ , which also comes at a linear cost.

The dominating error in probably all setups of interest is thus the truncation error. It is also very difficult to compensate for this error, because of the  $\mathcal{O}(\chi_c^3)$  scaling of the computational cost. As a trivial example, when starting a real time evolution with a state with Schmidt dimension smaller than  $\chi_c$ , the simulation runs with a constant truncation error. As the simulation continues, there comes a point where more states than  $\chi_c$  are needed, and the truncation error quickly overcomes the Trotter error, which basically defines a runaway time for the simulation, as reported in [57], see also figure 5.2. A reasonable and often used estimator of the truncation error is the discarded weight

$$D_k = 1 - \sum_{\alpha_k=1}^{\chi_m} \lambda_{\alpha_k}^2 \quad (4.13)$$



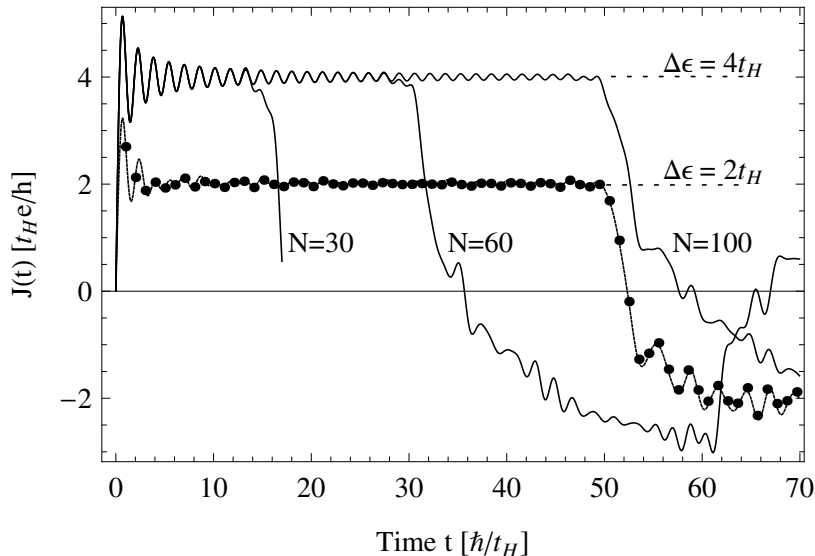


Figure 4.2. Current for non-interacting fermions for setup (I). Shown are TEBD results (dots) and one-particle equation of motion outcomes (lines) for different system sizes  $N$ . The TEBD results for  $\Delta\epsilon = 4t_H$  are not shown for reasons of clarity, but they almost perfectly agree with the displayed equation of motion outcomes.

for a bipartite split at the  $k$ -th bond where  $\chi_m < \chi_c$  is the number of kept eigenvalues. Figure 4.2 shows the very good agreement between our TEBD simulations and the exact calculation using the single particle reduced density matrix (3.6) and the one-particle equation of motion (3.10) for the tight-binding model. More detailed analyses of simulation errors are presented in the respective sections 5.1 and 6.1 where the TEBD method is applied to the spinless fermion model and the Hubbard model.

### 4.3 Notes on the computation of stationary currents

Using both methods, TEBD and the FABE approach from chapter 2, we investigate the stationary currents in the spinless fermion model and in the Hubbard model in chapters 5 and 6. In that context, we compare our outcomes with exact results for the systems without Coulomb interaction. An-

alytical results are known for setup (I), see equation (3.22). For setup (II), exact results are calculated numerically using the one-particle equation of motion with a system size of  $N = 1000$ . We have found that our procedure yields stationary current values which agree with an overall error of less than 5% with the exact results. Additionally, it has been checked by Alex Cujhovski that our FABE method calculations agree with the field-theoretical analysis and td-DMRG simulations [22] for the IRLM. We nevertheless have to remark that the IRLM is far easier to simulate than the spinless fermion model or the Hubbard model, since for higher Coulomb interactions the correlations (and thus the needed Schmidt dimension) within the nanowire grow more quickly than in the IRLM.

For the following discussions of the stationary current results, we remark that the value of the potential bias is given by a parameter  $\Delta\epsilon$  of the Hamiltonian, which corresponds to an external field. However, the potential difference measured in experiments might differ from this value [12, 60] and a voltage is applied to leads which are connected to the quantum wire. The effects of leads attached to a TLL have been widely investigated [19, 61, 62, 63, 64] and it has been shown that the conductance is given by  $e^2/h$  independently of the Coulomb interaction within the TLL. Moreover, this result coincides with experimental outcomes.

However, the motivation in this thesis is to understand the effects in correlated nanostructures and thus our main interest does not lie on the influence of attached leads, but on transport properties of isolated correlated nanowires. Concerning this matter, recently the contactless transport in a Hubbard-like system could be observed experimentally during the free expansion of an initially confined atomic cloud within a homogeneous optical lattice [65].

## 4.4 Summary

In this chapter, we have explained how we implemented a multi-threaded version of the TEBD algorithm, which is capable of running on 150 cores with an extremely low overhead. In addition, we have shown that our methods to simulate and extract the stationary current (using TEBD and the FABE approach) work well for several test models for which exact results or comparative data are available, such as non-interacting fermions and the IRLM.

## CHAPTER 5

## Spinless fermion model

In this chapter, we investigate a one-dimensional lattice model representing correlated conductors driven out of equilibrium by a potential bias. For spinless fermions the Hamiltonian without a potential bias is

$$\begin{aligned}
 H_0 = & -t_{\text{H}} \sum_{j=1}^{N-1} (c_j^\dagger c_{j+1} + c_{j+1}^\dagger c_j) \\
 & + V_{\text{H}} \sum_{j=1}^{N-1} \left( n_j - \frac{1}{2} \right) \left( n_{j+1} - \frac{1}{2} \right)
 \end{aligned} \tag{5.1}$$

where  $t_{\text{H}}$  denotes the hopping amplitude between nearest-neighbor sites,  $V_{\text{H}}$  is the Coulomb repulsion between spinless fermions on nearest-neighbor sites, and  $n_j = c_j^\dagger c_j$ . This so-called spinless fermion model can be interpreted as a system of spin-polarized electrons. At half-filling ( $N/2$  fermions in an  $N$ -site lattice) this Hamiltonian describes an ideal conductor for  $-2t_{\text{H}} < V_{\text{H}} \leq 2t_{\text{H}}$ .

Although the closely related spin  $\frac{1}{2}$   $XXZ$  chain has been studied in several works using the td-DMRG method [10, 57, 58], the nonlinear properties of the model (especially its full  $I$ - $V$  characteristics) have not been investigated. The low-energy behaviour of this lattice model is described by the TLL theory [5, 7] for which two parameters are important: The velocity of elementary excitations (renormalized Fermi velocity)  $v$  and the dimensionless correlation exponent  $K$ . From the Bethe Ansatz solution we know the relation between TLL parameters and the parameters  $t_{\text{H}}$  and  $V_{\text{H}}$  of the spinless fermion model at half-filling

$$v = \pi \frac{a_L t_{\text{H}}}{\hbar} \sqrt{1 - \left( \frac{V_{\text{H}}}{2t_{\text{H}}} \right)^2} \left[ \arccos \left( \frac{V_{\text{H}}}{2t_{\text{H}}} \right) \right]^{-1} \tag{5.2}$$

and

$$K = \frac{\pi}{2} \left[ \pi - \arccos \left( \frac{V_{\text{H}}}{2t_{\text{H}}} \right) \right]^{-1} \tag{5.3}$$

where  $a_L$  is the lattice constant which we set  $a_L = 1$  in all numerical simulations. To drive the system out of equilibrium we use the step-like potential bias  $\Delta\epsilon$  from equation (3.3).

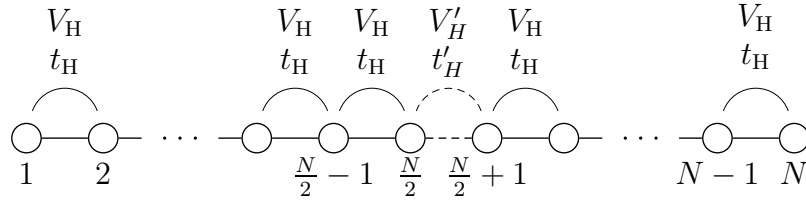


Figure 5.1. One-dimensional conductor consisting of two coupled leads. A bias between its right- and left-hand halves is applied and the current is measured in the middle of the system at the junction between both sides (dashed connection).

The above system can be seen as two coupled interacting leads consisting of the sites  $\{1 \dots \frac{N}{2}\}$  and  $\{\frac{N}{2} + 1 \dots N\}$ , respectively, see figure 5.1. The coupling is given by a hopping term  $t'_H$  between the left- and right-hand sides of the system (i.e., between site  $N/2$  and site  $N/2 + 1$ ) and an additional coupling  $V'_H(n_{N/2} - 1/2)(n_{N/2+1} - 1/2)$ . We restrict ourselves to the homogeneous system ( $t'_H = t_H$  and  $V'_H = V_H$ ), but our approach is also applicable to systems with weaker links, such as for instance a quantum dot [32, 22].

According to the TLL theory, the stationary current (3.21) in the linear regime is given by [5]

$$\bar{J} = \frac{e^2}{h}KV = \frac{e}{h}K\Delta\epsilon \quad \text{for } V \geq 0. \quad (5.4)$$

The states initially prepared with setup (I) or (II) are all half-filled for  $t = 0$ . If a weak potential bias is applied, the system remains approximately half-filled, and thus we expect that the TLL predictions (5.4) are valid for our simulations in the linear regime.

We should point out that in setup (I) the two leads are decoupled with respect to the Coulomb interaction  $V'_H$  for the calculation of the ground state. Our tests have revealed that otherwise a strong dependency of the stationary current on the system size appears, that is, for smaller system sizes the stationary current becomes higher but for  $N \rightarrow \infty$  it approaches the same constant value as the value one gets with  $V'_H = 0$  for  $t = 0$ . Choosing  $V'_H = 0$  for the computation of the ground state therefore decreases the finite-size error.

## 5.1 Simulation parameters and errors

For the realtime simulations, we use the TEBD method described in chapter 4 with a maximal Schmidt dimension in the range of  $300 \leq \chi_c \leq 500$ , depending on the specific parameter combination. We use a site-dependent  $\chi_c(\text{site})$  and allow our simulations to adapt  $\chi_c(\text{site})$  if test values (discarded weight, entanglement entropy) show the necessity to do so. We have to remark that for higher  $|V_H|$  and  $\Delta\epsilon$  the correlations (and thus the needed Schmidt dimension) within the spinless fermion model grow very quickly. Hence, the chosen  $\chi_c$ -range can lead to significantly larger errors in the regime  $|V_H| \geq 1.6t_H$  and  $\Delta\epsilon \geq 3t_H$ .

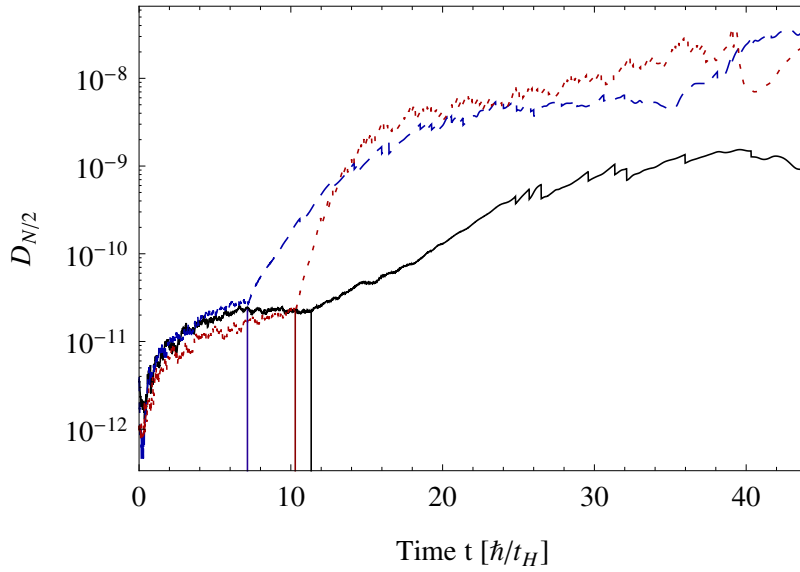


Figure 5.2. Discarded weight  $D_{N/2}$  for different parameters. solid black curve:  $\Delta\epsilon = 0.5t_H$ ,  $V_H = 0.8t_H$ , dashed blue curve:  $\Delta\epsilon = t_H$ ,  $V_H = 1.6t_H$ , dotted red curve:  $\Delta\epsilon = 2t_H$ ,  $V_H = 0$ . The vertical lines indicate the runaway times described in the text.

Figure 5.2 shows the discarded weight for different parameters for a split in the middle of the chain. One can see the runaway time (see chapter 4) indicated by the vertical lines. However, the maximal discarded weight over all simulations, sites and times up to  $40\hbar/t_H$  we measured is yet smaller than  $10^{-6}$ . Our simulations reveal that when taking a maximal Schmidt dimension of  $\chi_c = 600$  instead of 300, the runaway time is shifted only about 20% to larger times and the quantities of interest are only slightly changed.

Moreover, the stationary current computed with the FABE approach, is only changed by less than 0.5%.

We use a time step  $\delta t = 0.01$ , a system size  $N = 100$  and a typical simulation runs approximately 1/2 to eight hours for a ground state calculation and about four hours to one week for a realtime evolution. We have used 12 threads for a TEBD simulation on average. The total single-core CPU time needed to obtain the simulation results in this chapter amounts to approximately two million hours.

## 5.2 Simulation results

In this section, we discuss our results for the stationary current in the spinless fermion model and show our findings for the finite-system period as a function of the interaction strength  $V_H$ .

### 5.2.1 Current-voltage characteristics

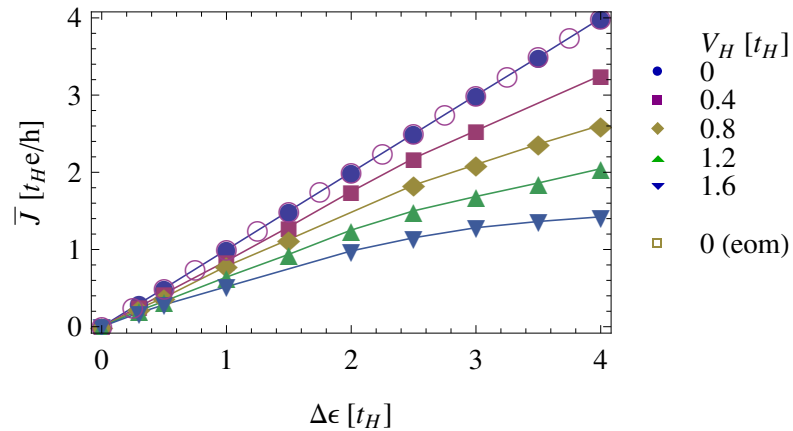


Figure 5.3. Current-voltage curve of the spinless fermion model with **setup (I)** for several **positive**  $V_H$ . For  $V_H = 0$  the current has been computed using TEBD and the one-particle equation of motion (eom). The lines are guides for the eyes.

In setup (I) the current in the non-interacting system is proportional to  $\Delta\epsilon$  up to the band width of the system, according to equation (3.22). For  $V_H > 0$  figure 5.3 shows that the current increases sub linearly with  $\Delta\epsilon$  for a fixed interaction strength  $V_H$  and that it decreases monotonically with

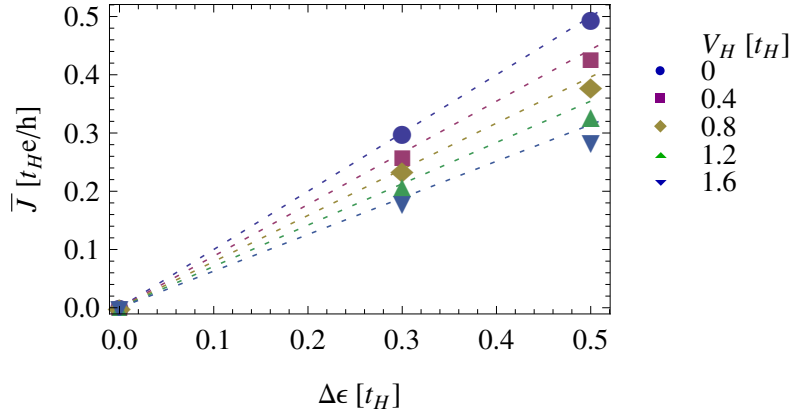


Figure 5.4. Magnification of figure 5.3. The lines indicate the linear response according to the TLL theory (5.4) for small  $\Delta\epsilon$ .

increasing  $V_H$  for a fixed potential bias  $\Delta\epsilon$ . The magnification in figure 5.4 shows a comparison with the linear response in the TLL theory (5.4) for small  $\Delta\epsilon$ , using the Bethe Ansatz solution parameters (5.3). The good agreement confirms the validity of our approach. Obviously, an increasing  $V_H$  does not only reduce the current but also the range of the potential bias  $\Delta\epsilon$  for which the linear response approximation remains valid.

In figure 5.5 we observe a behaviour for attractive interactions  $V_H < 0$  which is quite similar to the non-interacting case. The current increases almost linearly with  $\Delta\epsilon$  and then saturates at a  $V_H$ -dependent maximum. As  $V_H$  is increased, the maximal current is decreased but also a higher linear conductance is present for small applied voltages. Figure 5.6 shows that for negative interactions our results agree as well with the TLL theory (5.4) for small  $\Delta\epsilon$ . Again, increasing  $|V_H|$  seems to reduce the range of the potential bias  $\Delta\epsilon$  for which the linear response approximation remains valid.

We can easily understand the appearance of the plateaus in the  $I$ - $V$  curves for large applied voltages. In setup (I), one half of the chain initially contains more particles than the other one due to the applied potential bias  $\Delta\epsilon$ . When  $\Delta\epsilon$  is large enough to separate the system into a completely filled and a completely empty reservoir (i.e., when saturation occurs), increasing the applied voltage does not increase the current anymore. According to expression (3.22), this saturation occurs for non-interacting fermions at  $\Delta\epsilon = 4t_H$ . For an attractive interaction  $V_H < 0$ , the particles are more likely to stick together and thus even more particles gather in one half of the system. Therefore, saturation occurs for even smaller applied voltages, see figure 5.5. When

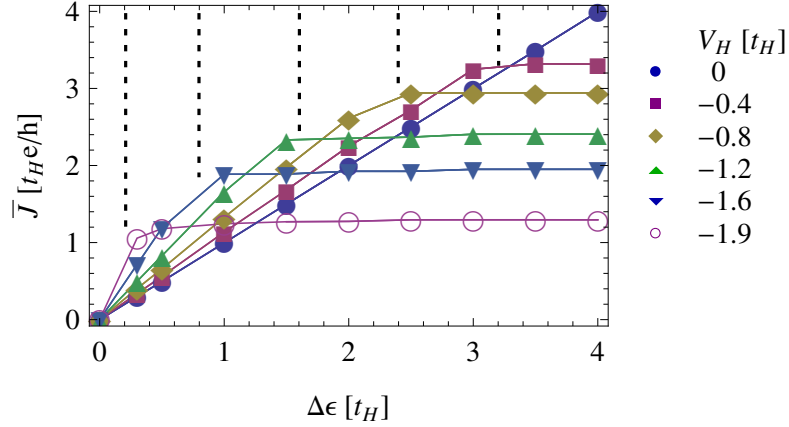


Figure 5.5. Current-voltage curve of the spinless fermion model with **setup (I)** for several **negative**  $V_H$ . The dashed lines indicate the theoretical beginning of the current plateaus according to (5.5). The solid lines are guides for the eyes.

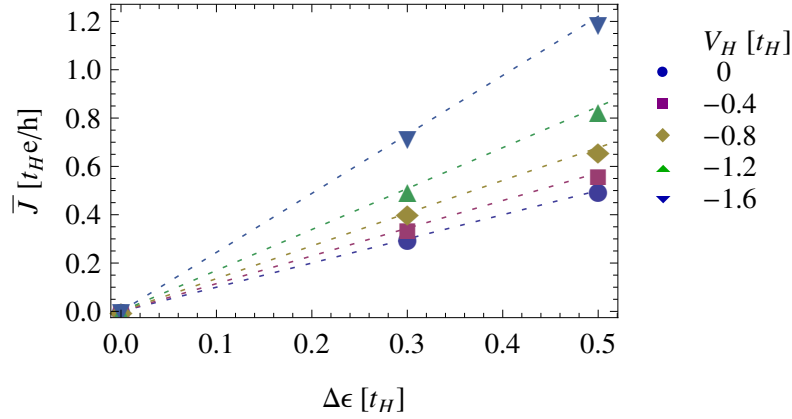


Figure 5.6. Magnification of figure 5.5. The lines indicate the linear response according to the TLL theory (5.4) for small  $\Delta\epsilon$ .

$V_H > 0$ , the effect is reversed, and thus saturation occurs at higher values  $\Delta\epsilon > 4t_H$ , beyond the potential range shown in figure 5.3. The decreasing of the plateau heights with increasing  $|V_H|$  is not yet understood.

We can approximately determine for which potential difference  $\Delta\epsilon$  the system reaches saturation. Removing a single particle from the completely



filled reservoir or adding one particle to the empty half costs an energy  $\Delta\epsilon/2 - V_H - 2t_H$ . Thus, saturation occurs if

$$\Delta\epsilon \geq 2V_H + 4t_H. \quad (5.5)$$

Figure 5.5 shows that this approximation fits well to the numerical data for  $V_H \leq 0$  whereas the saturated regime according to (5.5) for  $V_H > 0$  lies outside the potential range shown in figure 5.3, as mentioned above.

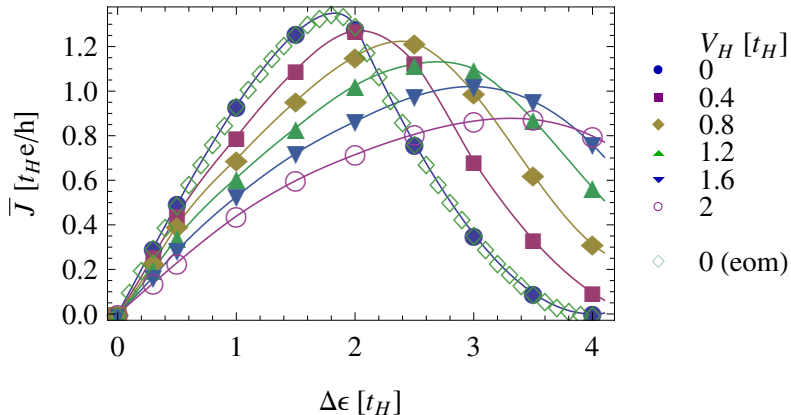


Figure 5.7. Current-voltage curve of the spinless fermion model with **setup (II)** for several **positive**  $V_H$ . For  $V_H = 0$  the current has been computed using TEBD and the one-particle equation of motion (eom). The lines are guides for the eyes.

While for setup (I) the differential conductance is always positive, we observe a negative differential conductance in setup (II) for  $V_H \geq 0$ , see figure 5.7. The current seems to vanish for very large potential biases as predicted by strong-coupling perturbation theory for this setup. We note that the current becomes smaller with increasing  $V_H$  for a small potential bias. For larger  $\Delta\epsilon$  the behaviour of  $I$  as a function of  $V_H$  is no longer monotonic. Additionally, it can be seen that the position of the maximum of  $I$  as a function of  $\Delta\epsilon$  is shifted to higher values with increasing  $V_H$ . The magnification for small  $\Delta\epsilon$  (figure 5.8) confirms again that our results agree with the TLL theory in the linear regime and that the range of the linear response regime shrinks with increasing interaction strength.

For setup (II) and  $V_H < 0$ , figure 5.9 shows again a negative differential conductance and a vanishing current for very large potential biases. In contrast to the case  $V_H > 0$  for this setup, we see that the maximum of the

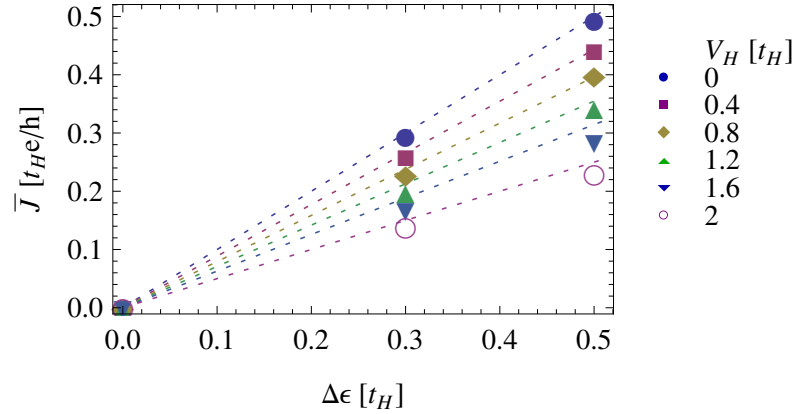


Figure 5.8. Magnification of figure 5.7. The lines indicate the linear response according to the TLL theory (5.4) for small  $\Delta\epsilon$ .

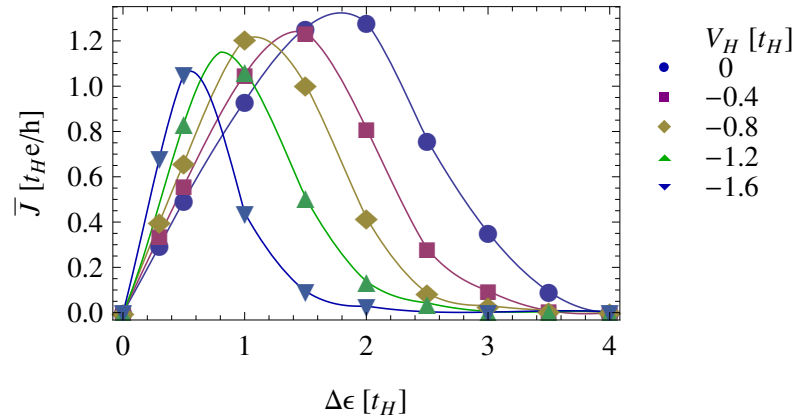


Figure 5.9. Current-voltage curve of the spinless fermion model with **setup (II)** for several **negative**  $V_H$ . The lines are guides for the eyes.

current is shifted to lower values of  $\Delta\epsilon$  for increasing  $|V_H|$ . Finally, the data in figure 5.10 shows the good agreement between our results and the TLL theory predictions in the small bias regime. We again see, that the interaction strength rapidly reduces the range of potential biases for which the linear response remains valid.

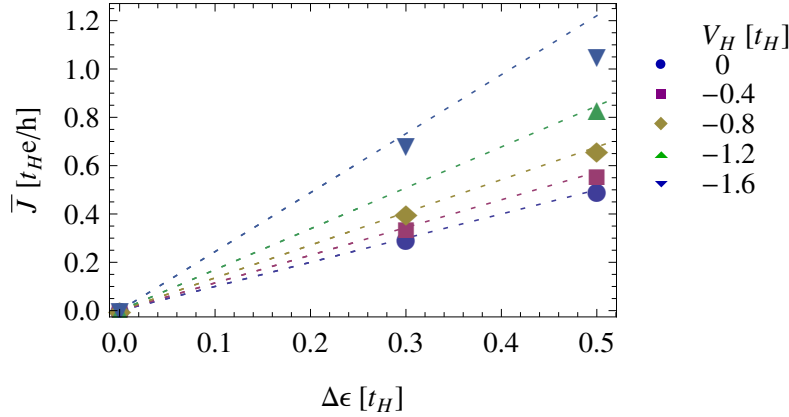


Figure 5.10. Magnification of figure 5.9. The lines indicate the linear response according to the TLL theory (5.4) for small  $\Delta\epsilon$ .

The negative differential conductance which is observed in setup (II) for all  $V_H$  can be understood in terms of the overlap of the energy bands for elementary excitations. Our simulations show that there is no significant difference in the current curve whether one initially does or does not couple source and drain (the two halves of the system). For the following considerations we can therefore regard source and drain as initially decoupled, having two separate but equal energy bands. Then we apply a step-like voltage in setup (II) and thus shift the two bands against each other. For  $V_H = 0$  only overlapping occupied one-particle states in the source and unoccupied ones in the drain contribute to the current. While this overlap rises with increasing  $|\Delta\epsilon|$  from 0 to  $2t_H$ , it diminishes from  $\Delta\epsilon = 2t_H$  and reaches zero at  $4t_H$ . As a result, the current is maximal for  $\Delta\epsilon \approx 2t_H$  and vanishes for large  $\Delta\epsilon$ . Similarly, we can understand the non-monotonic behaviour in interacting cases ( $V_H \neq 0$ ) in terms of the overlap of the elementary excitation bands in the spinless Luttinger liquids in the two halves of the system. However, the effective bandwidth is renormalized like the Fermi velocity in equation (5.2). Therefore, the maximum of the current is reached for a smaller potential bias  $\Delta\epsilon$  when  $V_H$  becomes negative as shown in figure 5.9, and shifted to a higher potential bias when  $V_H$  is increased, see figure 5.7. Our conclusion agrees with the findings in [43] where it is shown that within a similar one-dimensional model a negative differential conductance is mainly caused by finite electrode bandwidths.

### 5.2.2 Influence of $V_H$ on the period $T^{\max}$

Our results show a further effect of  $V_H$  on the finite-system current. While for  $V_H > 0$  the period of the rectangular oscillation becomes smaller, it grows for negative interactions.

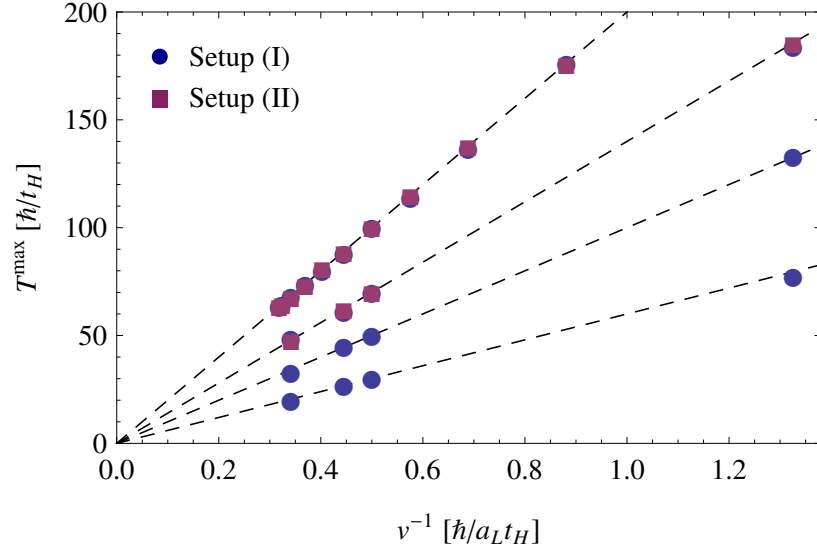


Figure 5.11. Period  $T^{\max}$  of the rectangular current oscillation in the finite spinless fermion model as a function of the inverse renormalized Fermi velocity  $v^{-1}$  from expression (5.2). The dashed lines are described by equation (5.6).

Figure 5.11 shows the period  $T^{\max}$  of the rectangular current oscillation in the finite system as a function of the inverse renormalized Fermi velocity  $v^{-1}$  from expression (5.2). The  $T^{\max}$  values are mean values from various  $\Delta\epsilon$  for each setup. These values agree perfectly with the dashed lines in figure 5.11 which are given by the equation

$$T^{\max}(V_H) = \frac{v(V_H = 0)}{v(V_H)} T^{\max}(V_H = 0). \quad (5.6)$$

Thus, the period is fully determined by the time-scale of the non-interacting system  $T^{\max}(V_H = 0)$  from (B.15) and the renormalized Fermi velocity  $v$  from expression (5.2).

## 5.3 Summary

In this chapter we have applied the TEBD method and our FABE approach to obtain stationary current values in the full voltage range for the spinless fermion model. We found that while in the linear regime the results are mostly independent from the specific setup, the non-linear characteristics are primarily determined by it. For setup (I) the system shows a positive differential conductance over the full voltage range and the current saturates at a finite value for both, repulsive and attractive interactions  $V_H$ . For setup (II) we observe a negative differential conductance and for large applied voltages the current vanishes. The effects from setup (II) also occur in the non-interacting case and come from the finite bandwidth and the nonlinear dispersion of the excitations [42, 43].

Finally, it turned out that the period of the oscillating current in the finite system is fully determined by the time-scale of the non-interacting system  $T^{\max}(V_H = 0)$  from (B.15) and the renormalized Fermi velocity  $v$  from expression (5.2), according to equation (5.6).



## CHAPTER 6

### Hubbard model

So far in this thesis we have investigated one-dimensional non-interacting quantum systems in chapter 3 and extended this study to interacting spinless fermions in chapter 5. However, spinless fermions are in most cases far away from a realistic description of electrons in a solid. The simplest model which covers electron-electron interaction for particles with spin is the fermionic Hubbard model [66, 67, 68].

This model has been under permanent research since its invention in the early 1960s. Among others, the model was widely studied to investigate heavy fermions, the magnetic properties of solids and high-temperature superconductivity. Over the years, several methods have been used to study the Hubbard model, for instance mean field calculations [69], studies using perturbation theory and numerical methods like the quantum Monte Carlo [70, 71] or the DMRG method [72].

At half-filling the one-dimensional Hubbard model describes a Mott-insulator for any value of the repulsive onsite Coulomb interaction  $U_H > 0$  while for all other fillings it is a metal. This Mott-metal-insulator transition shows the competition between the kinetic energy of the fermions and the repulsion  $U_H$  of two particles [73]. At half-filling and for  $U_H > 0$ , the system tries to avoid doubly occupied states such that each site is preferably occupied with a single electron, and charge fluctuations around this state are energetically very expensive. On the contrary, the kinetic energy term in the Hamiltonian tries to delocalize the particles into Bloch states, leading to a metal for  $U_H = 0$ .

The one-dimensional Hubbard model without a potential bias is exactly solvable with the Bethe Ansatz solution and several properties such as the full phase diagram and elementary excitations are well known [74, 17, 18]. For small applied voltages, the transport properties are described by the TLL theory [5, 7] and the stationary current in the linear regime is given by

$$\bar{J} = \frac{2e^2}{h}KV = \frac{2e}{h}K\Delta\epsilon. \quad (6.1)$$

However, the correlation exponent  $K$  can not be obtained analytically, but from numerical solutions of the integral equation of Lieb and Wu [75]. One gets, that while for an attraction  $U_H < 0$  the conductance in the linear

regime is increased, it becomes smaller for a repulsive interaction  $U_H > 0$ . This behavior agrees with the characteristics of the current-voltage curves in the spinless fermion model with respect to  $V_H$ .

The Hubbard Hamiltonian for a one-dimensional lattice without a potential bias is

$$\begin{aligned}
 H_0 = & -t_H \sum_{\sigma,j=1}^{N-1} (c_{\sigma,j}^\dagger c_{\sigma,j+1} + c_{\sigma,j+1}^\dagger c_{\sigma,j}) \\
 & + U_H \sum_{\sigma,j=1}^N \left( n_{\sigma,j} - \frac{1}{2} \right) \left( n_{\sigma,j} - \frac{1}{2} \right) + \bar{\epsilon} \sum_{\sigma,j=1}^N n_{\sigma,j} \quad (6.2)
 \end{aligned}$$

where  $t_H$  is the hopping amplitude,  $U_H$  denotes the onsite Coulomb repulsion between two spins,  $c_j^{(\dagger)}$  are the fermionic annihilation (creation) operator for site  $j$  and spin  $\sigma$ , and  $n_{\sigma,j} = c_j^\dagger c_j$ . The reason for adding an additional potential offset  $\bar{\epsilon}$  to every site is given in section 6.1. We drive the system out of equilibrium by using the previously presented setups (I) and (II) with the Hamiltonian

$$H_B = \frac{\Delta\epsilon}{2} \left( \sum_{\sigma,j=1}^{N/2} n_{\sigma,j} - \sum_{\sigma,j=N/2+1}^N n_{\sigma,j} \right), \quad (6.3)$$

perform TEBD simulations and extract the stationary current (3.21) using the FABE method presented in chapter 2. Since the Hubbard model is an insulator for half-filling, the following simulations are performed away from half-filling with a fixed particle number  $n_p$ , leading to a couple of problems which are described below.

## 6.1 Simulation parameters, modifications and errors

For the following simulations, we use the TEBD method described in chapter 4 with a maximal Schmidt dimension of  $\chi_c = 1000$ . The maximal discarded weight over all simulations, sites and times up to  $40\hbar/t_H$  we measured is smaller than  $10^{-6}$ . For the non-interacting case we compare our TEBD results with exactly available results from one-particle equation of motion calculations and find that the outcomes for the stationary current match within an error of less than  $10^{-3}$ . We use a time step  $\delta t = 0.01$ , a system size  $N = 100$  and a typical simulation runs approximately 2-4 weeks for a ground state calculation and about two months for a realtime evolution. We have



used 16 threads for a TEBD simulation on average. The total single-core CPU time needed to obtain the simulation results in this chapter amounts to approximately one and a half million hours.

As already mentioned above, there is a problem in the calculation of the ground state with a fixed particle number  $n_p$ . Basically, the time evolution of TEBD is grand canonical, allowing any particle number from 0 to  $2N$  for the Hubbard model. To force the system into having a specific particle number one can use an implementation of TEBD with particle symmetry, but tests performed by Alex Cojuhovski showed that this is only applicable in a regime which is slightly away from the filling which the system naturally prefers due to the applied onsite potentials. Thus, we have introduced the additional potential offset  $\bar{\epsilon}$  in equation (6.2) with which we can control the preferred total particle number of the system. We use a Newton gradient method during the imaginary time evolution to adapt the potential offset, i.e. we increase or decrease the potential offset after each time step, dependent on whether the total particle number is currently too low or too high. Unfortunately, this procedure can lead to very long (up to four weeks) ground state calculations. It would have been easier to perform the TEBD ground state simulations with a given (and fixed) potential offset  $\bar{\epsilon}$ , but the actual  $\bar{\epsilon}$  which is needed to enforce a certain particle number  $n_p$  depends on the system size  $N$ , on  $U_H$  and on the applied potential  $\Delta\epsilon$ .

For all following simulations, we use a filling of 0.9, i.e. 90 particles in a Hubbard model with one hundred sites, which is slightly below half-filling. Note that for the realtime evolution, the potential offset  $\bar{\epsilon}$  keeps its value from the computation of the ground state.

## 6.2 Simulation results

In this section we show the computed potential offsets for various Coulomb interactions  $U_H$  and applied potentials  $\Delta\epsilon$ . Furthermore, we show  $I$ - $V$  characteristics for the Hubbard model for setup (I). Unfortunately, due to limited computational resources, the high computational cost and recurring technical problems at the RRZN, results for setup (II) are not available.

### 6.2.1 Equilibrium onsite potentials

Due to our Newton-gradient procedure for the imaginary time evolution, we have obtained the potential offset  $\bar{\epsilon}$  for repulsive and attractive Coulomb interaction, see figures 6.1 and 6.2.

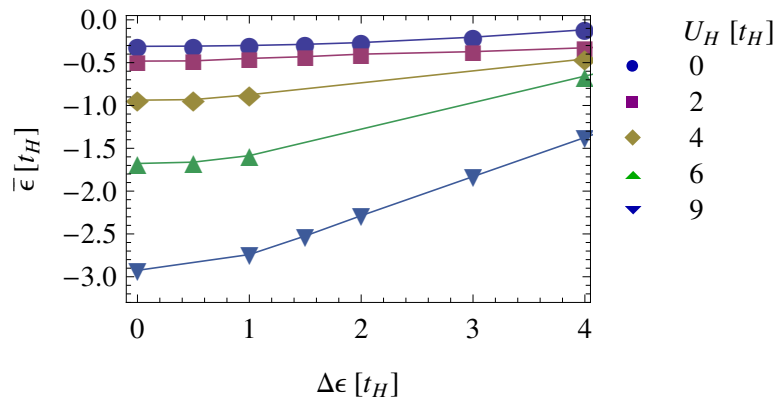


Figure 6.1. Potential offset  $\bar{\epsilon}$  for setup (I) and positive  $U_H$ . The lines are guides for the eyes.

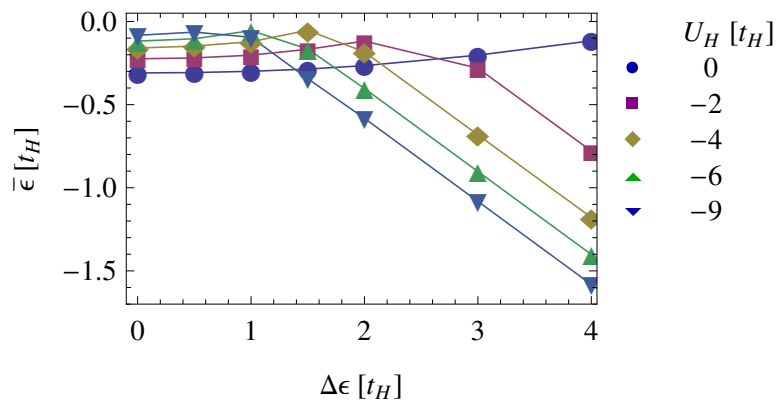


Figure 6.2. Potential offset  $\bar{\epsilon}$  for setup (I) and negative  $U_H$ . The lines are guides for the eyes.

When the repulsion between the particles is increased, the potential offset for a constant number of particles is decreased as expected, see figure 6.1. For an attractive Coulomb interaction this effect is generally reversed, but for higher voltages, the potential offset is again decreased with both an increasing  $\Delta\epsilon$  and an increasing  $|U_H|$ , see figure 6.2. This effect is not yet understood.

### 6.2.2 Current-voltage characteristics

In setup (I) the current shows a similar behavior as in the spinless fermion model. For small applied biases it is proportional to the bias (as predicted by the TLL theory), but for larger voltages it saturates at a finite value, dependent on the interaction strength  $|U_H|$ . While the height of the plateau is decreased with increasing  $|U_H|$  we observe the beginning of a second plateau for a repulsive interaction, which can be easily understood.

Since we simulate the system with a filling of 0.9, when  $\Delta\epsilon$  is increased, there comes the point when one of the system-halves approaches half-filling and thus this half becomes gapped for  $U_H > 0$  (the first plateau). Only when the applied voltage is increased to a value high enough to overcome the Mott gap, the number of electrons in this half can increase beyond one per site and the current is again increased. For still higher voltages the current saturates at its actual maximum when one half of the system has a maximal filling and the other one is empty. The position of the second plateau is shifted to higher values of  $\Delta\epsilon$  with increasing  $U_H$ , in agreement with the increase of the Mott gap, see figure 6.3.

We note that our results can not be compared with the TLL predictions, since we do not have suitable values for the small bias regime. As we know that for positive  $U_H$  ( $K < 1$ ) the linear conductance should be smaller with larger  $|U_H|$ , and vice versa for negative  $U_H$  ( $K > 1$ ), figures 6.3 and 6.4 indicate this behaviour.

For negative  $U_H$  and higher voltages in setup (I) the current as a function of time decays slowly towards its stationary value. This decay is quick enough for a system of size  $N = 100$  to obtain the stationary value from larger times, but for times  $t \approx T^{\max}/4$  (where  $T^{\max}$  is the period of the rectangular oscillation) this value is not yet reached, see figure 6.5. Our FABE approach has shown to be valid if we use simulation results from times  $t < T^{\max}/4$ , but several tests with one-particle equation of motion outcomes show that the method also works fine with data from times  $t < T^{\max}/2$ . For the results obtained for negative  $U_H$  we have thus used data from times up to  $t \approx T^{\max}/2$  where necessary.

Finally, we note that in contrast to the spinless fermion model, the period  $T^{\max}$  of the finite-site rectangular oscillation remains constant for all  $U_H$ .

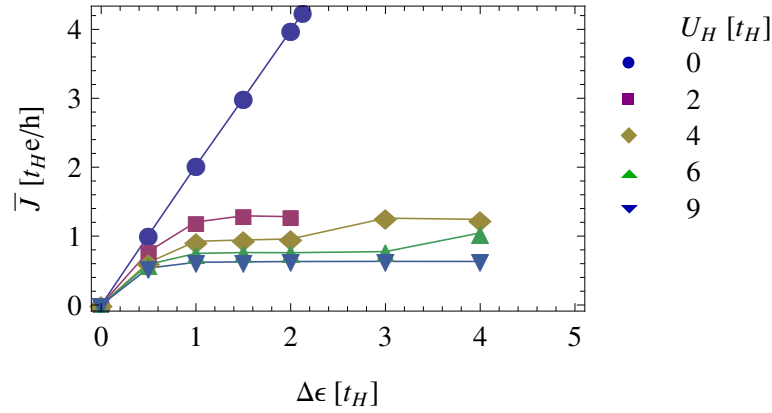


Figure 6.3. Current-voltage curve of the Hubbard model with **setup (I)** for several **positive**  $U_H$ . For  $U_H = 0$  the currents computed with the one-particle equation of motion match the TEBD results. The lines are guides for the eyes.

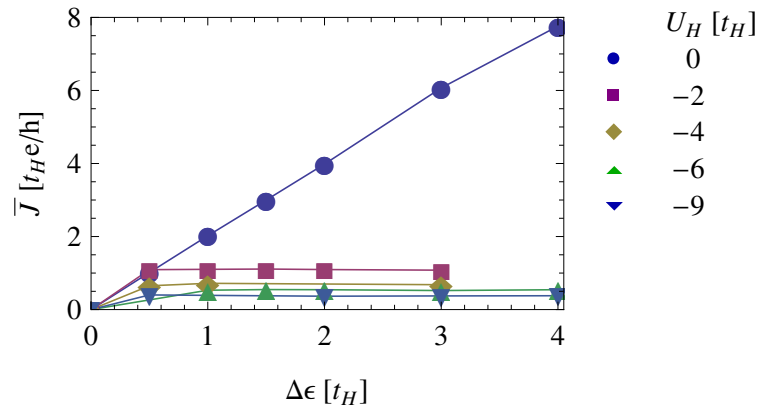


Figure 6.4. Current-voltage curve of the Hubbard model with **setup (I)** for several **negative**  $U_H$ . The lines are guides for the eyes.

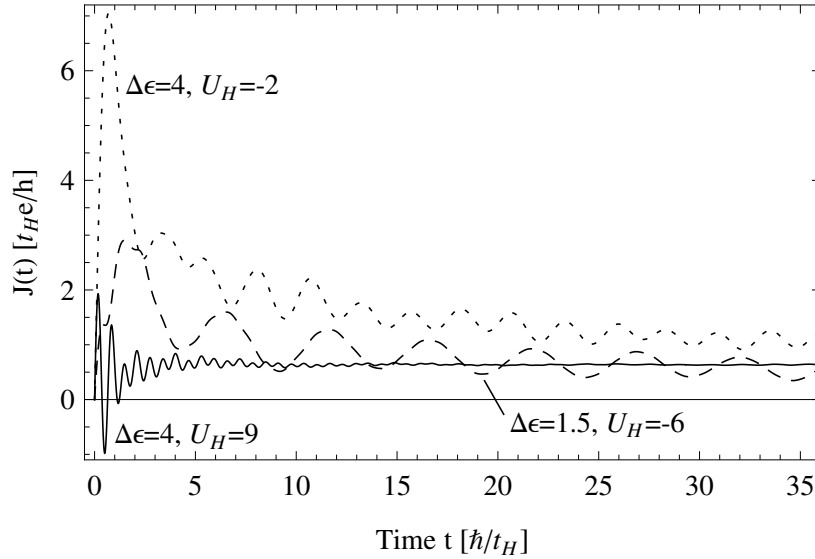


Figure 6.5. Currents through the middle bond in the Hubbard model with a system size  $N = 100$  for **setup (I)** as a function of time.

### 6.3 Summary

In this chapter, we extended the TEBD method to be able to enforce a fixed particle number to a system by adapting an applied potential offset. We simulated the one-dimensional Hubbard model and obtained  $I$ - $V$  characteristics for setup (I). Due to limited computational resources, the high computational cost and recurring technical problems at the RRZN, results for setup (II) are not available. Despite similar effects as in the spinless fermion model, we found the beginning of a second plateau for positive  $U_H$ . When the applied voltage is increased, one half of the system reaches half-filling and thus becomes a Mott insulator. Only when the voltage is larger than the Mott gap, the current is increased again.



## CHAPTER 7

### Two-site system coupled to a bosonic bath

As it has been argued before, lattice vibrations play an important role in actual experimental situations, such that we should add a bosonic bath to our one-dimensional correlated nanostructure. Unfortunately, no exact results or comparative data are available for the systems we investigated in the last chapters, but since the TEBD method has never been used to simulate such systems, we have to test its applicability first. Therefore, we have chosen to simulate a system which is closely related to our problem and for which comparative data from (TD) NRG [76] ((time dependent) numerical renormalization group) simulations are available: a two-site fermionic system coupled to a bosonic bath [44]. The impurity is described by the extended Hubbard model which combines the nearest-neighbor Coulomb interaction from the spinless fermion model and the onsite interaction from the Hubbard model.

At half-filling (i.e. with two particles in the impurity), this model describes the essentials of a two-electron transfer in a dissipative environment. Also most investigations on such transfer processes focus on single-electron transfer and it has been argued that the two-electron transfer has a major contribution in many processes, such as in DNA [45] or in proteins [77].

The original NRG method was proposed by Wilson to solve the Kondo problem [78, 79], but recently the method has been extended to simulate quantum impurities coupled to a bosonic bath and the realtime dynamics of systems out-of-equilibrium (see for instance [80]). While (TD) NRG provides a very accurate description of the bosonic bath, the TEBD method can principally be used to simulate even more extended impurities, such as large molecular bridges or nanowires. However, so far TEBD has not been used to simulate a quantum system in a bosonic bath and it is thus important to compare both methods to proof the applicability of the TEBD algorithm to such problems.

## 7.1 Two-site fermionic system in a bosonic bath

We investigate a two-site extended Hubbard model embedded in a dissipative environment (bosonic bath). The first site is called (D)onor while the second

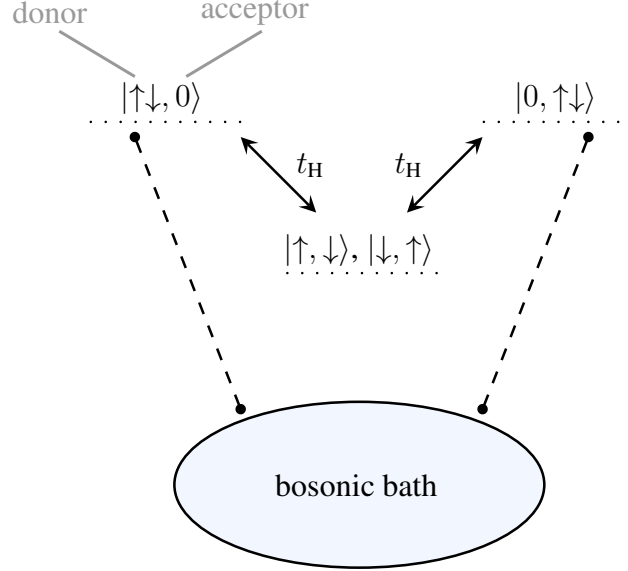


Figure 7.1. Local basis of the two-site extended Hubbard model. The doubly occupied states are coupled to a bosonic bath.

one is the (A)cceptor, see figure 7.1. The Hamiltonian is given by

$$H = H_{\text{el}} + H_{\text{coupl}} + H_{\text{b}}$$

with the two-site operator

$$\begin{aligned} H_{\text{el}} = & \frac{\epsilon}{2} \sum_{\sigma=\uparrow,\downarrow} (c_{D\sigma}^\dagger c_{D\sigma} - c_{A\sigma}^\dagger c_{A\sigma}) - t_{\text{H}} \sum_{\sigma} (c_{D\sigma}^\dagger c_{A\sigma} + c_{A\sigma}^\dagger c_{D\sigma}) \\ & + U_{\text{H}} (n_{D\uparrow} n_{D\downarrow} + n_{A\uparrow} n_{A\downarrow}) + \frac{V_{\text{H}}}{2} \sum_{\sigma,\sigma'} \sum_{i,j=A,D;i \neq j} n_{i\sigma} n_{j\sigma'} \end{aligned} \quad (7.1)$$

and the terms for the bosonic bath and its coupling to the two-site system

$$\begin{aligned} H_{\text{b}} &= \sum_{n=1}^{\infty} \omega_n \tilde{b}_n^\dagger \tilde{b}_n, \\ H_{\text{coupl}} &= \sum_{\sigma} (n_{A\sigma} - n_{D\sigma}) \sum_{n=1}^{\infty} \frac{\lambda_n}{2} (\tilde{b}_n^\dagger + \tilde{b}_n). \end{aligned} \quad (7.2)$$



The parameter  $\epsilon$  describes an applied potential difference on the two fermionic sites.  $c_{D,A\sigma}^{(\dagger)}$  are the fermionic creation and annihilation operators for Donor (D) and Acceptor (A),  $\tilde{b}_n^{(\dagger)}$  are the bosonic ones and the fermionic particle number operator is  $n_{D,A\sigma} = c_{D,A\sigma}^\dagger c_{D,A\sigma}$ . The hopping parameter is  $t_H$  and the onsite and nearest-neighbour Coulomb interaction strength is determined by  $U_H$  and  $V_H$ . The two-site extended Hubbard model (7.1) is thus an extension of the normal Hubbard model by the nearest-neighbour Coulomb interaction  $V_H$  which we already know from the spinless fermion model. It can be shown that the dynamics of the system is governed only by the difference  $\tilde{U} = U_H - V_H$  and accordingly we will choose  $V_H = 0$  for all following simulations.

In all following simulations, the particle number in the fermionic part of the system is set to  $n_p = 2$ . Thus, the local dimension of the two-site system is 4 which is apparent from figure 7.1.

### 7.1.1 Mapping to a semi-infinite chain

The coupling term  $H_{\text{coupl}}$  connects every bosonic state to the two-site system. Such a ‘star’ Hamiltonian cannot be simulated with TEBD since the method is based on the possibility to perform an alternate update of bonds which are not nearest neighbors. The problem of using TEBD for two-dimensional systems will be treated in chapter 8 in particular. However, the Hamiltonian can be mapped onto a semi-infinite chain [81] where only the first bosonic site couples to the fermionic system. For the mapping we need to know the bath spectral function which is chosen [44]

$$J(\omega) = 2\pi\alpha\omega \quad \text{for } 0 < \omega < \omega_c \quad (7.3)$$

and zero otherwise. The parameter  $\alpha$  describes the coupling strength between the bath and the two-site system. For simulation outcomes, all variables are given in units of the cut-off frequency  $\omega_c$ . The semi-infinite Hamiltonian is

$$H = H_{\text{el}} + \frac{\sqrt{\eta_0}}{2}(b_0^\dagger + b_0) \sum_{\sigma=\uparrow,\downarrow} (n_{A\sigma} - n_{D\sigma}) + \sum_{n=0}^{N_{\text{bath}}} \epsilon_n b_n^\dagger b_n + \sum_{n=0}^{N_{\text{bath}}-1} t_n (b_n^\dagger b_{n+1} + b_{n+1}^\dagger b_n) \quad (7.4)$$

where ideally the length of the bosonic chain  $N_{\text{bath}} \rightarrow \infty$  and

$$\eta_0 = \int_0^{\omega_c} J(\omega) d\omega = \int_0^{\omega_c} 2\pi\alpha\omega d\omega = \pi\omega_c^2\alpha. \quad (7.5)$$

Figure 7.2 shows the corresponding setup. The onsite potentials  $\epsilon_n$  and

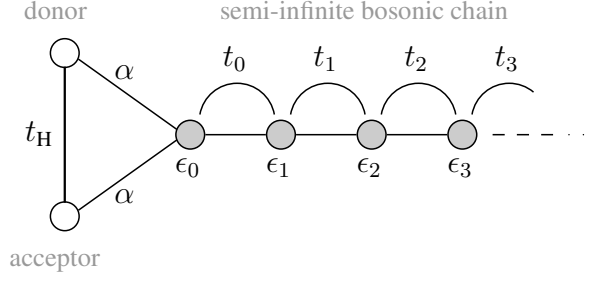


Figure 7.2. Two-site fermionic system coupled to a semi-infinite bosonic chain.

hopping terms  $t_n$  for the semi-infinite bosonic chain from expression (7.4) can be calculated using the following recursion relation, which is initialized for site  $m = 0$  by

$$\begin{aligned}
 U_{0n} &= \frac{\gamma_n}{\eta_s} \\
 \epsilon_0 &= \sum_{n=0}^{\infty} \xi_n U_{0n}^2 \\
 t_0 &= \frac{1}{\eta_s} \sqrt{\sum_{n=0}^{\infty} (\xi_n - \epsilon_0)^2 \gamma_n^2} \\
 U_{1n} &= \frac{1}{t_0} (\xi_n - \epsilon_0) U_{0n}
 \end{aligned}$$

with

$$\begin{aligned}
 \eta_s &= \sqrt{\eta_0} = \omega_c \sqrt{\pi \alpha} \\
 \gamma_n &= \eta_s \sqrt{\frac{\Lambda^2 - 1}{\Lambda^{2n+2}}} \\
 \xi_n &= \frac{2\omega_c}{3} \frac{\Lambda^3 - 1}{\Lambda^n (\Lambda^3 - \Lambda)}.
 \end{aligned}$$

The recursion proceeds for  $m > 0$  as

$$\begin{aligned}\epsilon_m &= \sum_{n=0}^{\infty} \xi_n U_{mn}^2 \\ t_m &= \sqrt{\sum_{n=0}^{\infty} [(\xi_n - \epsilon_m)U_{mn} - t_{m-1}U_{m-1,n}]^2} \\ U_{m+1,n} &= \frac{1}{t_m} [(\xi_n - \epsilon_m)U_{mn} - t_{m-1}U_{m-1,n}]\end{aligned}$$

and runs from  $m = 0$  to  $N_{\text{bath}} - 1$  to compute the  $\epsilon_m$  and  $t_m$  for all sites.  $U_{mn}$  denotes an auxiliary variable and  $\Lambda$  is the discretization parameter. All the sums which run to infinity include terms  $\xi_n$  or  $\gamma_n$  which both decay exponentially with  $n$ , wherefore we can cut the summations at a finite value  $N_{\text{sum}} = 10^4$ . Our tests have shown that a higher value  $N_{\text{sum}} = 10^5$  does not noticeably change our results. Since even with an optimized procedure very high powers of  $\Lambda$  are to be calculated, a big-integer class [82] is needed to avoid roundoff errors [83].

### 7.1.2 General simulation parameters

The hopping term  $t_n$  in (7.4) decays exponentially with  $t_n \propto \Lambda^{-n}$ , which naturally allows us to take only a finite number of bosonic sites into account. Nevertheless, the local dimension  $m_b$  of a bosonic site stays infinite, which means that we have to cut the local dimension and thus allow only a finite number of bosons per site. For the model and parameters considered here, we have used a maximal  $m_b = 8$  for the TEBD simulations, which corresponds to maximally seven bosons per site.

For the mapping onto a linear chain, the energy continuum has to be logarithmically discretized into intervals  $[\Lambda^{-(n+1)}\omega_c, \Lambda^{-n}\omega_c]$  with  $n \in \mathbb{N}_0$  where only a single mode of each interval couples to the impurity. This process is characterized by the discretization parameter  $\Lambda$ . The discretization is lossless for  $\Lambda = 1$  but in that case the hopping terms  $t_n$  do not decay exponentially with  $n$ . Instead, a  $\Lambda > 1$  has to be used which is small enough to give correct results but yet large enough such that the chain can be cut at a sufficiently small length  $N_{\text{bath}}$ . For the TEBD simulations, the length of the bosonic chain has been set to  $N_{\text{bath}} = 40$  such that the hopping term at its end is smaller than 0.02 for  $\Lambda = 1.1$ . We have checked that this length is sufficient for all following simulations since our outcomes do not noticeably change for  $N_{\text{bath}} = 30$ .

Applied to the presented two-site model in a bosonic bath, the equilibrium NRG (which corresponds to the imaginary time-evolution for TEBD) starts with the two-site fermionic system and takes only the first bosonic site ( $n = 0$ ) into account. If  $H_n$  is the Hamilton operator including the impurity and all sites of the bosonic system up to site  $n$  the NRG uses the renormalization group transformation to compute the ‘next’ Hamiltonian  $H_{n+1}$  which includes all bosonic sites up to  $n + 1$ . In each step, only the  $N_s$  lowest eigenstates of the Hamiltonian are retained. In order to give accurate results, the NRG method needs a sufficiently quick exponential decay of the hopping terms  $t_n$  such that in every iterative step the rest of the chain contributes only perturbatively [84]. For the following NRG simulations results, the discretization parameter has therefore been chosen  $\Lambda = 2$ . Typically, a local bosonic dimension  $m_b \geq 8$  is used and  $N_s = 100$  states are kept in each iteration. All NRG results presented in this thesis are based on simulations which have been carried out by Sabine Tornow and which already have been published in [44].

## 7.2 Simulation results

Since the particle number in the two fermionic sites is fixed to  $n_p = 2$ , we define the following observables

$$\begin{aligned}\hat{d}_D &= |\uparrow\downarrow, 0\rangle\langle\uparrow\downarrow, 0| = \hat{n}_{D\uparrow}\hat{n}_{D\downarrow} \\ \hat{d}_A &= |0, \uparrow\downarrow\rangle\langle 0, \uparrow\downarrow| = \hat{n}_{A\uparrow}\hat{n}_{A\downarrow} \\ \hat{n}_{DA} &= |\uparrow, \downarrow\rangle\langle\uparrow, \downarrow| + |\downarrow, \uparrow\rangle\langle\downarrow, \uparrow| = \hat{n}_{D\uparrow}\hat{n}_{A\downarrow} + \hat{n}_{D\downarrow}\hat{n}_{A\uparrow}\end{aligned}\quad (7.6)$$

which measure the double occupancy  $\hat{d}_D$ ,  $\hat{d}_A$  of donor and acceptor and the combined population of the singly occupied states  $\hat{n}_{DA}$ .

### 7.2.1 Equilibrium properties

The equilibrium double occupancy expectation values for  $\epsilon = 0$  in the presented model have been calculated using NRG and TEBD, see figure 7.3. For this symmetric model ( $\epsilon = 0$ ) these expectation values are equal for donor and acceptor (in the equilibrium state)

$$\langle\hat{d}_D\rangle_{\text{eq}} = \langle\hat{d}_A\rangle_{\text{eq}} = \langle\hat{d}\rangle_{\text{eq}}. \quad (7.7)$$

Each TEBD simulation took almost one month on 8 cores. On the one hand, a very ‘high’ maximal Schmidt dimension  $\chi_c = 150$  compared to the local dimension of the bosonic bath  $m_b = 8$  had to be used. We note that the

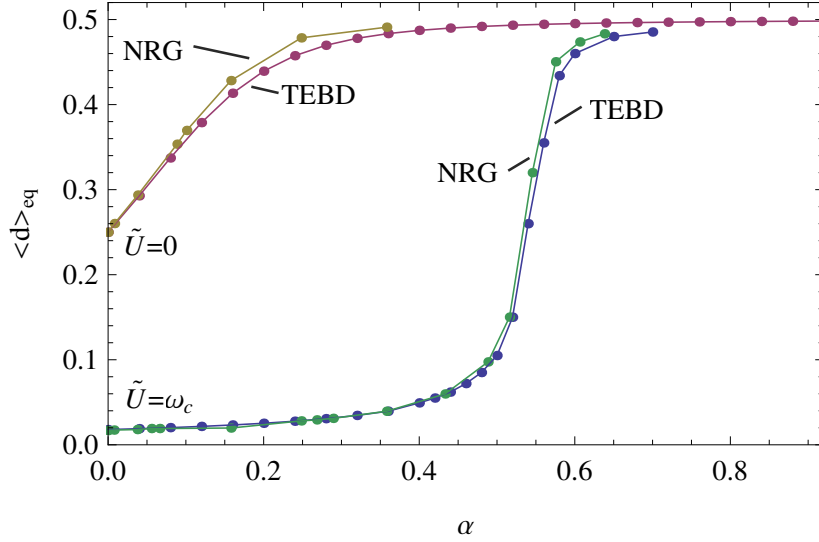


Figure 7.3. Low-temperature equilibrium probability for double occupancy  $\langle d \rangle_{\text{eq}}$  as a function of the coupling parameter  $\alpha$  for  $\epsilon = 0$  and  $t_{\text{H}} = 0.1\omega_c$ .  $\Lambda = 2$  for NRG and  $\Lambda = 1.1$  for TEBD with a chain length  $N_{\text{bath}} = 40$ , a maximal Schmidt dimension  $\chi_c = 150$  and a local dimension of the bath  $m_b = 8$ . Note that  $\tilde{U} = U_{\text{H}} - V_{\text{H}}$ , as described in the text.

simulation time of the TEBD method scales with  $\mathcal{O}(\chi_c^3)$  and  $\mathcal{O}(m_b^3)$ , where in case of a local dimension of 8, a simulation performs 64 times worse than a simulation of the spinless fermion system with the same  $\chi_c$ . This scaling can be seen in [app. C], since the density matrix is of size  $(\chi_c \cdot m_b) \times (\chi_c \cdot m_b)$  and the main computational time is needed to diagonalize it. On the other hand, TEBD has never been the best candidate to calculate the ground (equilibrium) state of a system since the imaginary time evolution is typically much slower than for instance the corresponding NRG or DMRG routine. Consequently, it turns out to be very hard to simulate the equilibrium state of a system coupled to a bosonic bath using the TEBD algorithm.

We note that the double occupancy  $\langle \hat{d} \rangle_{\text{eq}}$  decreases with increasing  $\tilde{U}$ , as expected, and increases with increasing  $\alpha$  (see figure 7.3). For further interpretations see [44], where several aspects of the model have been investigated in detail.

## 7.2.2 Realtime dynamics

For the realtime simulations performed in this section, we prepare the system such that initially two electrons are located in the donor and none in the acceptor. The bosonic bath is empty for  $t = 0$ . We then let the system evolve in time and the particles start moving from donor to acceptor. The result for the double occupancy  $\langle d_A \rangle$  together with the NRG simulation outcomes can be seen in figure 7.4. First, we note that our data agrees with the results from

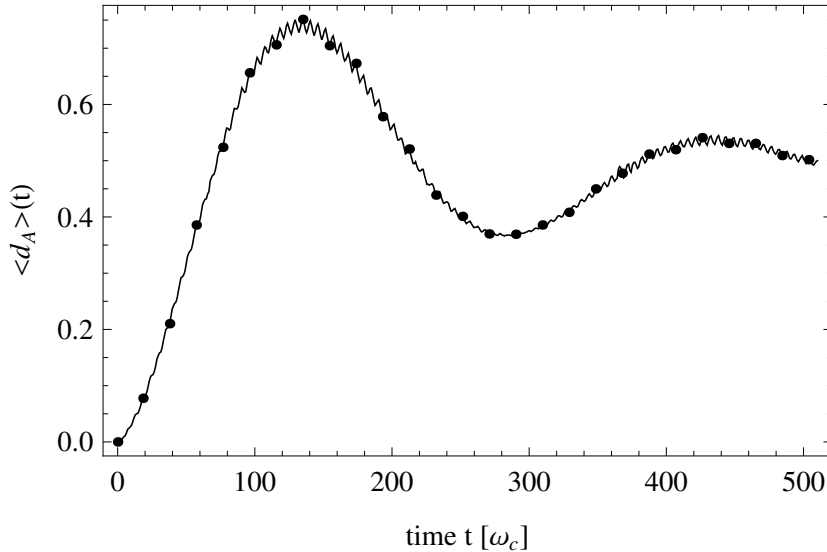


Figure 7.4. Probability for double occupancy  $\langle d_A(t) \rangle$  as a function of time for  $\alpha = 0.04$ ,  $\epsilon = 0$  (for  $t > 0$ ),  $\tilde{U} = -\omega_c$  and  $t_H = 0.1\omega_c$ .  $\Lambda = 2$  for NRG and  $\Lambda = 1.1$  for TEBD with a chain length  $N_{\text{bath}} = 40$ , a maximal Schmidt dimension  $\chi_c = 150$  and a local dimension of the bath  $m_b = 8$ . The initial state has been prepared with the two electrons at the donor site and an empty bosonic bath. The line denotes the NRG results from [44] and the dots are TEBD outcomes for comparison.

the NRG simulation. One can see a dominant oscillation stemming from a coherent oscillation between the two sites. It is damped, due to the coupling to the bosonic bath, i.e. the presence of dissipation in the impurity. As can be explained in the framework of the spin-boson model, this oscillation disappears for larger values of  $\alpha$  leading to an overdamped current, see [44].

In figure 7.5 we see the realtime evolution of the particle number distribution  $\langle n_{bi} \rangle$  of the bosonic bath. For  $t = 0$  no bosons are in the bath

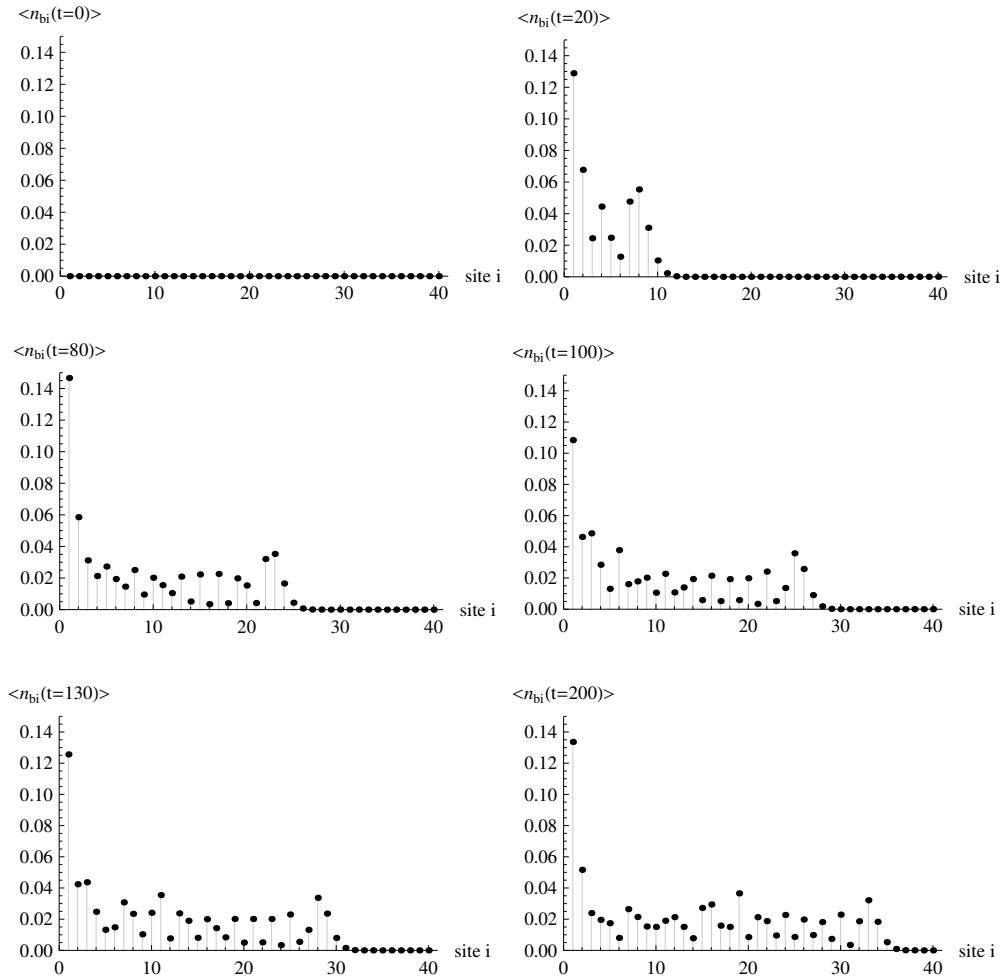


Figure 7.5. Particle number distribution  $\langle n_{bi} \rangle$  as a function of time, in the bosonic bath for the realtime evolution with the same parameters as for the simulations from figure 7.4.

but as the simulation continues, the coupling to the impurity creates bosons which start to move along the chain. A corresponding movie is available on [whypsi.com/einhellinger/bosonicBathDistribution.zip](http://whypsi.com/einhellinger/bosonicBathDistribution.zip). In this movie, it becomes more clearly, that the propagation speed of the bosons is (apparently exponentially) reduced over time. Thus, we found that a length of  $N_{\text{bath}} = 40$  is enough to simulate the time scale depicted in figure 7.4. Even though in figure 7.5 it looks as if the bosons had almost (in terms of time) reached the

border, this is actually not the case.

We have performed the above simulations with various discretizations  $\Lambda = 1.1, 1.5, 1.8, 2$  and found no difference in our outcomes. Thus, we can confirm that the simulations performed with  $\Lambda = 2$  using the (TD) NRG method most probably reveal the true characteristics of the system.

The TEBD simulations have been performed with a maximal Schmidt dimension  $\chi_c = 150$ , resulting in a maximal discarded weight (4.13)  $D = 10^{-6}$ . Although we have seen the applicability of the TEBD method to systems coupled to a bosonic bath, the realtime evolution performs really badly since we have to use a very small time step  $\delta t = 10^{-3}$ . In case of a Suzuki-Trotter expansion of  $p$ -th order, the error is of the order  $\mathcal{O}(\delta t^{p+1})$ , i.e. for the second order expansion (4.10) we have used, it is  $\mathcal{O}(\delta t^3)$ . Unfortunately, TEBD is only highly parallelizable if a high Schmidt dimension  $\chi_c$  is needed and not a small time step. For the simulations performed in chapter 7 only eight threads could be used until the overhead quickly exceeded 10%. Thus, further effort should be put in optimizing the TEBD algorithm for such cases, for instance by using a higher (for instance fourth) order Suzuki-Trotter decomposition

$$e^{\delta t(F+G)} = e^{s\delta t F/2} e^{s\delta t G} e^{(1-s)\delta t F/2} e^{(1-2s)\delta t G} e^{(1-s)\delta t F/2} e^{s\delta t G} e^{s\delta t F/2} + \mathcal{O}(\delta t^5) \quad (7.8)$$

with  $s = 1/(2 - 2^{1/3})$ . Using this decomposition, a one hundred times larger time step could be applied at less than three times the computational cost for each time step. Alternatively, one could also work on a Krylov basis using a Lanczos diagonalization routine or with a higher order Runge-Kutta procedure (which is admittedly non-unitary). Some of these solutions have already been implemented for the td-DMRG method [85]. However, this seems to be the main task if one is interested in using the TEBD method for systems coupled to bosonic baths. In addition, an optimized basis for the bosons [86, 87] could also improve the performance of ground state and realtime simulations.

### 7.3 Summary

In this chapter, we successfully extended the TEBD method and applied it to an impurity system coupled to a bosonic bath. We compared our outcomes for the ground state and realtime calculations with (TD) NRG results from [44] and found both data in good agreement. Moreover, we performed our simulations with various discretizations  $\Lambda = 1.1, 1.5, 1.8, 2$  and found no difference in our outcomes, thus confirming that (TD) NRG calculations with  $\Lambda = 2$  actually give correct results.



Admittedly, TEBD does not perform well, neither for the ground state calculation nor for the realtime evolution of a system coupled to a bosonic bath. An optimized basis for the bosons [86, 87] could improve this behaviour for imaginary and realtime evolutions, while for the realtime evolution an improved time evolution approach seems necessary.

Nevertheless, we have proven the general applicability of the TEBD method to such problems, such that with an improved method (or using an adapted td-DMRG algorithm for instance), we could principally study larger quantum systems coupled to phonon baths, such as molecular junctions [88] or nanowires which are beyond reach for the (TD) NRG method.



## CHAPTER 8

### Ladder systems

As already emphasized in the introduction (chapter 1), realistic nanowires are not truly one-dimensional. Our first step towards higher-dimensional systems is a ladder system, i.e. a two-dimensional model with a width of only a few lattice sites. Although various methods such as the DMRG algorithm have been applied to study two dimensional systems [89] like the two-dimensional t-J-model or the Hubbard model, most research is concentrated on ground state calculations and none is concerned with the realtime dynamics of correlated conductors. However, the TEBD method has not been used yet to study the realtime evolution of two-dimensional systems driven out-of-equilibrium by an external bias.

Although at a first glance, it might seem difficult to apply TEBD to a two-dimensional system, since the Suzuki-Trotter decomposition can not be used, it can be achieved for 2D systems with a small extent in one dimension (ladder systems) by projecting several sites onto a single one. This amounts to building an effectively one-dimensional Hamiltonian with nearest-neighbor interaction, see figure 8.1. For every effective site in the new model we take the full Hilbert space into account, i.e. given that  $n_o$  original sites, each with a local dimension  $m$ , contribute to one effective site, the dimension of the effective site will be  $m^{n_o}$ . However, one can not simply work in the effective model as if it were one-dimensional by construction, but has to keep in mind its two-dimensional origin, for instance when computing expectation values. It is especially important to take the fermion anti-commutation relation into account.

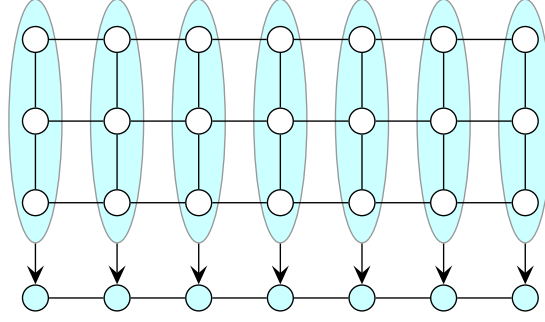


Figure 8.1. Mapping of all sites and bonds in the smaller dimension (width) onto a single site and bond.

## 8.1 Tight-binding ladder system

The model which is chosen to show the applicability of TEBD to two-dimensional models is described by the tight-binding Hamiltonian

$$\begin{aligned}
 H = & -t_H \left[ \sum_{x=1}^{N-1} \sum_{y=1}^W (c_{xy}^\dagger c_{x+1,y} + c_{x+1,y}^\dagger c_{xy}) \right. \\
 & \left. + \sum_{y=1}^{W-1} \sum_{x=1}^N (c_{xy}^\dagger c_{x,y+1} + c_{x,y+1}^\dagger c_{xy}) \right] - \sum_{x=1}^N \sum_{y=1}^W \epsilon_{xy} \quad (8.1)
 \end{aligned}$$

where  $c_{xy}^{(\dagger)}$  is the fermionic annihilation (creation) operator for site  $(x, y)$ ,  $t_H$  denotes the hopping term and  $\epsilon_{xy}$  is an on-site potential. Whenever only two different potentials are applied in the system, we refer to the potential difference as  $\Delta\epsilon$ . We study the model at half-filling. In the following, the system is restricted to a width  $W = 2$  and a length  $N = 60$ . As we want to show the applicability of the TEBD method to such two-dimensional systems, we exclude any Coulomb interaction to be able to compare our results with one-particle equation of motion (3.10) outcomes, since results for interacting systems are not available.

## 8.2 Simulation parameters and errors

For the simulations whose results are presented in the following section, we use a maximal Schmidt dimension  $\chi_c = 750$ , a system length  $N = 60$  and a time-step  $\delta t = 0.01$ . Since the local dimension of the (spinless) tight-binding model is  $m = 2$ , the local dimension of the effective model is  $m = 4$ , as

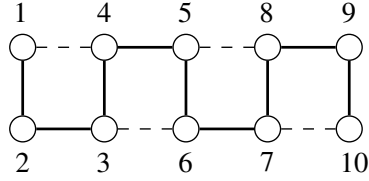


Figure 8.2. Consecutive numbering of the sites in a ladder system. The bold bonds are highlighted to show the path along which the sites are numbered, but apart from that all bonds are equal.

for instance for the Hubbard model which was presented in chapter 6. One could see the two legs in the ladder systems as the two spin channels in the Hubbard model and accordingly the hopping from the first to the second leg as a spin-flip.

As we are simulating fermions, it holds that due to the fermion anti commutation relation, a term  $c_j^\dagger c_{j+n}$  gives the phase

$$(-1)^{\sum_{i=1}^{j-1} n_i} (-1)^{\sum_{i=1}^{j-1+n} n_i} = (-1)^{\sum_{i=j}^{j-1+n} n_i} \quad (8.2)$$

where  $n_i$  denotes the particle number for site  $i$  and a numbering of the sites is necessary, see figure 8.2. In a nearest-neighbor model in one dimension we basically have the terms  $c_j^\dagger c_{j+1}$  and  $c_j^\dagger c_j$ . It is clear from equation (8.2) that  $c_j^\dagger c_j$  has a phase 1. For  $c_j^\dagger c_{j+1}$ -terms one only gets a contribution if there is a particle at the  $(j+1)$ -site and none at site  $j$ . Thus,  $n_j = 0$ , which also gives 1 for the phase of a nearest-neighbor hopping term. Although for a one-dimensional setup the phases can be neglected, it is different for the presented ladder system where terms  $c_j^\dagger c_{j+3}$  with a possibly negative phase appear, see figure 8.2. Effectively, there is no difference between hardcore bosons and fermions in one dimension with nearest neighbor hopping since without loops in the system, the particles can not be interchanged. However, this can happen in the presented fermionic ladder system.

The maximal discarded weight (4.13) for the shown simulation results is smaller than  $10^{-8}$  and the maximal deviation of the TEBD results from the one-particle equation of motion outcomes amounts to a little less than 2% for the realtime evolution.

## 8.3 Simulation results

The presented system is driven out of equilibrium using the two setups (I) and (II), which are adapted to the two-dimensional character of the system.

First, both legs are prepared in the same way in setup (I) and (II) and the current  $J_{N/2,1st\ leg} + J_{N/2,2nd\ leg}$  through the two bonds (figure 8.3a) in the middle is measured. Second, we prepare the system such that the voltage difference according to setup (I) or setup (II) is applied between the two legs, see figure 8.3b, and the total current (the sum of the currents through all bonds) from the first to the second leg is measured.

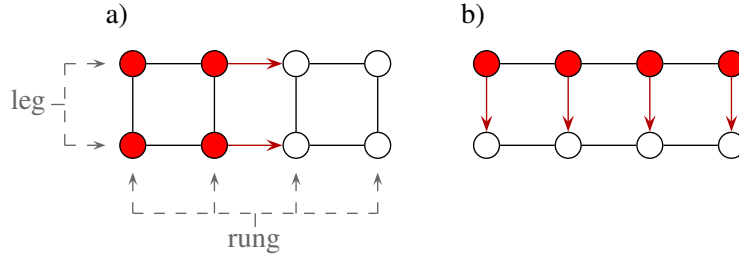


Figure 8.3. Two ways of driving the system out of equilibrium: a) All sites in the left half of the system have an applied potential  $+\Delta\epsilon/2$  while the rest has  $-\Delta\epsilon/2$ , either for  $t = 0$  (setup (I)) or for  $t > 0$  (setup (II)). b) The same preparation, but rotated through 90 degrees, i.e. rungs and legs are switched. The current is always measured as the sum through all bonds which are highlighted by red arrows.

The corresponding simulation results are shown in figures 8.4 and 8.5. We note that our TEBD results agree with the one-particle equation of motion calculations. However, the currents and their stationary values are different from the results of the one-dimensional system with the corresponding setups. This is mostly due to a different ground state in which the particles are delocalized over both legs. Our simulations further show that no current is flowing between the two legs for the simulations whose results are shown in figure 8.4 and accordingly no current is flowing between the rungs in the simulations whose results are displayed in figure 8.5. We conclude (only for the realtime evolution) that the legs (respectively the rungs) behave like unconnected one-dimensional structures for setup (I). Thus we expect that in an actual experiment including isolated charged nanowires, many one-dimensional effects should be reproducible, although the structures are not truly one-dimensional. However, further analyses of currents in two-dimensional systems including electron-electron interactions need to be done before we can speculate about a proper experimental setup.

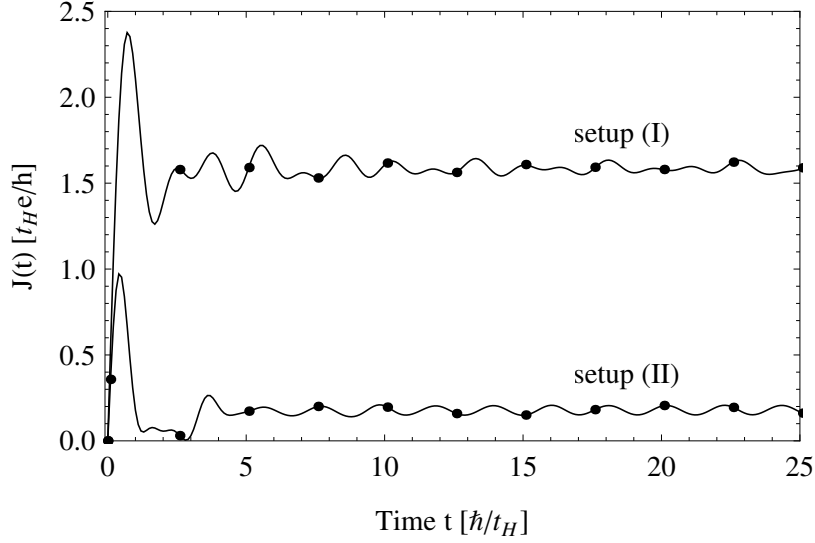


Figure 8.4. Current in the ladder system prepared as shown in figure 8.3a, with  $\Delta\epsilon = 3t_H$  and  $N = 60$ . The lines are calculated using the one-particle equation of motion (3.10) and the dots denote TEBD results for comparison.

## 8.4 Summary

In this chapter, we extended the TEBD method for two-dimensional systems, applied it to a tight-binding ladder and found that our results agree with the exact results from the one-particle equation of motion formalism. Furthermore, our first results indicate that the legs (respectively the rungs) behave like unconnected one-dimensional nanowires for the realtime evolution using setup (I).

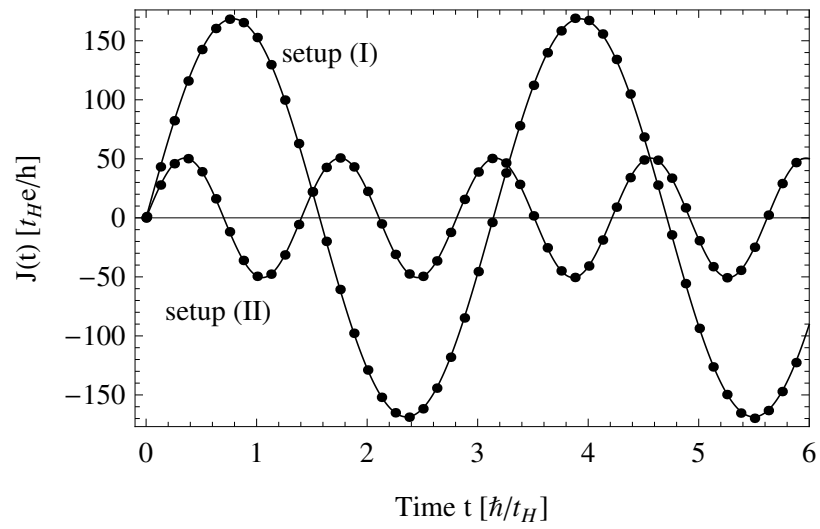


Figure 8.5. Current in the ladder system prepared as shown in figure 8.3b, with  $\Delta\epsilon = 4t_H$  and  $N = 60$ . The lines are calculated using the one-particle equation of motion (3.10) and the dots denote TEBD results for comparison.



## CHAPTER 9

# Summary, Conclusion & Outlook

### 9.1 Summary & Conclusion

The goal of this thesis has been to investigate basic transport properties in finite and infinitely large correlated nanosystems. Additionally, we have studied the possibilities to describe an actual experimental situation better, using the time evolving block decimation (TEBD) method. We have started our investigations with the classical  $LC$  line and investigated its transport properties for a setup in which one half of the system has been initially charged. We have found explanations for many finite-size effects, like for instance the origin of the rectangular or rapid oscillation, and solved the model exactly for the infinite case. Based on our studies we have developed a ‘Fourier analysis based extraction’ (FABE) method, which allows us to extract the stationary current from outcomes of analyses of finite systems.

We have then shown the close connection between the  $LC$  line and a quantum system described by the tight-binding model and we implemented a one-particle equation of motion algorithm to solve the quantum system exactly. The general applicability of our FABE approach to quantum systems has been first shown in that context and we argued that an extrapolation of the stationary current values obtained by our approach is unnecessary if the system size is sufficiently high ( $N \geq 70$  in our case).

For the investigation of correlated quantum systems such as the spinless fermion model or the Hubbard model, we have implemented a multi-threaded version of the TEBD algorithm, which is capable of running on 150 cores with an extremely low overhead. Using the TEBD method and our FABE approach, the full  $I$ - $V$  characteristics of the half-filled spinless fermion model and also  $I$ - $V$  characteristics of the Hubbard model away from half-filling have been obtained. For the Hubbard model, we have extended the TEBD method to enforce a fixed particle number to the system by adapting an applied potential offset during the imaginary time evolution. Thus, we have been able to perform all simulations with the same band filling (0.9). For our simulations, we have used two different setups to generate a current. In setup (I) the initial state has different particle numbers in its two halves

due to an applied potential difference while the system evolves in time with an overall equal onsite potential. In setup (II) we calculate the initial state without a potential difference but turn it on for the realtime evolution.

While our results for the linear regime are mostly independent from the specific setup, the non-linear behaviour of the system is primarily determined by it. For setup (I), we find a positive differential conductance for the full voltage range and a saturation in the  $I$ - $V$  curves for higher potential biases. With setup (II) we observe a negative differential conductance that can be understood in terms of the overlap of the elementary excitation bands in the spinless Luttinger liquids in the two halves of the system. Both effects – the plateaus and the negative differential conductance at large potential biases – also appear in the non-interacting case, and are due to the finite bandwidth of the system. For the spinless fermion model, we have found that the period of the rectangular current curve in the finite system is fully determined by the time-scale of the non-interacting system  $T^{\max}(V_H = 0)$  and the renormalized Fermi velocity  $v$ . For the Hubbard model, a second plateau has been observed for positive  $U_H$  which could be explained in terms of the band structure of the model. Several comparisons (with one-particle equation of motion results, exact results and other numerical data) have shown that our methods for simulating and extracting the stationary current (using TEBD and the FAFE approach) give correct results.

We have then explored the possibilities to include experimentally relevant extensions, such as lattice vibrations (i.e. coupling to a bosonic bath) and a higher dimensionality of our nanostructure. First, we have successfully extended the TEBD method and applied it to a two-site fermionic system coupled to a bosonic bath. Our results have been found to agree with equilibrium and realtime (TD) NRG calculations from [44]. Performing several simulations with different discretizations  $\Lambda = 1.1, 1.5, 1.8, 2$ , we have found no difference in the results, which confirms the validity of (TD) NRG calculations with  $\Lambda = 2$ . For a first test, we have extended the TEBD method for two-dimensional systems and applied it to a tight-binding ladder. We found that our results agree with the one-particle equation of motion calculations, and thus we have proven that TEBD can in principle be use to simulate such systems.

## 9.2 Outlook

The methods for extracting the stationary current presented in this thesis can be applied to other systems, such as systems with quantum dots or wires coupled to leads including electronic and also bosonic degrees of freedom. A bosonic bath added to the drain could for instance hinder particles emitted from source from being reflected at the hard edge by taking away their kinetic energy. Since then computations for the current from a longer time-interval could be taken into account, we would get more accurate results using smaller system sizes. As we already successfully applied the presented methods to the spinless fermion model, the Hubbard model and a non-interacting ladder system, we believe that they will be very useful to study nonlinear transport properties of correlated low-dimensional conductors. We have mostly tested our approach in the limit of transparent coupling between source and drain, thus it has to be checked if the methods still work when the hybridization between the leads is very small, i.e. when a weak coupling for instance through a quantum dot is present.

Unfortunately, we have found that TEBD performs poorly for the ground state and realtime calculations of bosonic systems. Using an optimized basis for the bosons [86, 87] could in principle improve this behaviour, but nevertheless, an improved time evolution approach (higher order Suzuki-Trotter, Runge-Kutta, Krylov-methods) seems to be necessary to efficiently apply TEBD to such problems. Nevertheless, with an improved method (or an extended td-DMRG algorithm for instance), we could study larger quantum systems coupled to bosonic baths, which are beyond reach of the (TD) NRG method.



## APPENDIX A

### LC line

#### A.1 Current in the finite LC line

The formal solution of equation (2.11) is given by [90]

$$q_k(t) = b_k \sin(\omega_k t) + d_k \cos(\omega_k t) \quad (\text{A.1})$$

with  $b_k, d_k \in \mathbb{R}$  given by initial conditions at time  $t = t_0 = 0$  and

$$\omega_k = \sqrt{\frac{\lambda_k}{LC}}. \quad (\text{A.2})$$

The matrix  $m_{ij}$  in equation (2.12) can be analytically diagonalized. Using equation (2.12), its eigenvalue equation

$$\begin{aligned} \sum_{j=1}^{N-1} m_{ij} p_{k,j} &= \lambda_k p_{k,i} \\ \Rightarrow -p_{k,i-1} - p_{k,i+1} &= (\lambda_k - 2) p_{k,i} \end{aligned} \quad (\text{A.3})$$

is solved by

$$p_{k,i} = \sqrt{\frac{2}{N}} \sin\left(\frac{ki\pi}{N}\right) \quad \text{and} \quad \lambda_k = 2 - 2 \cos\left(\frac{k\pi}{N}\right) \quad (\text{A.4})$$

where  $p_{k,i} = (\vec{p}_k)_i$  denotes the  $i$ -th component of the  $k$ -th eigenvector of  $m_{ij}$  and  $p_{k,0} = p_{k,N} = 0$  was defined.

*Proof:*

$$\begin{aligned} &\sin\left(\frac{ki\pi}{N} - \frac{k\pi}{N}\right) + \sin\left(\frac{ki\pi}{N} + \frac{k\pi}{N}\right) = 2 \cos\left(\frac{k\pi}{N}\right) \sin\left(\frac{ki\pi}{N}\right) \\ \Rightarrow &\sin\left(\frac{ki\pi}{N}\right) \cos\left(\frac{k\pi}{N}\right) + \underbrace{\cos\left(\frac{ki\pi}{N}\right) \sin\left(\frac{k\pi}{N}\right) - \cos\left(\frac{ki\pi}{N}\right) \sin\left(\frac{k\pi}{N}\right)}_{=0} \\ &+ \sin\left(\frac{ki\pi}{N}\right) \cos\left(\frac{k\pi}{N}\right) = 2 \sin\left(\frac{ki\pi}{N}\right) \cos\left(\frac{k\pi}{N}\right) \end{aligned} \quad (\text{A.5})$$

Using  $\vec{q} = O^{-1}\vec{I}$  from equation (2.8) and knowing that  $O$  contains the normalized eigenvectors  $\vec{p}_k$  of  $m_{ij}$  in its columns, it follows

$$I_i(t) = \sum_{k=1}^{N-1} p_{k,i} q_k(t) = \sqrt{\frac{2}{N}} \sum_{k=1}^{N-1} \sin\left(\frac{ki\pi}{N}\right) q_k(t) \quad (\text{A.6})$$

and with the formal solution (A.1) and equation (A.6), one gets

$$I_i(t) = \sqrt{\frac{2}{N}} \sum_{k=1}^{N-1} \sin\left(\frac{ki\pi}{N}\right) (b_k \sin(\omega_k t) + d_k \cos(\omega_k t)) \quad (\text{A.7})$$

where  $\omega_k$ , using equations (A.2), (A.4) and  $\cos(2x) = 1 - 2\sin^2(x)$ , is given by

$$\omega_k = \sqrt{\frac{\lambda_k}{LC}} = \frac{2}{\sqrt{LC}} \sin\left(\frac{k\pi}{2N}\right). \quad (\text{A.8})$$

*Note:*

Since  $O^{-1} = O^T$  one can write down  $c_k$  explicitly

$$\begin{aligned} c_k &= \sum_{i=1}^{N-1} (O^{-1})_{ki} (\dot{\phi}_i - \dot{\phi}_{i+1}) \\ &= \sum_{i=1}^{N-1} p_{k,i} (\dot{\phi}_i - \dot{\phi}_{i+1}) \\ &= \sqrt{\frac{2}{N}} \sum_{i=1}^{N-1} \sin\left(\frac{ki\pi}{N}\right) (\dot{\phi}_i - \dot{\phi}_{i+1}) \end{aligned} \quad (\text{A.9})$$

which gives us a better understanding of the condition  $c_k(t) = 0$ . Simply put, it means that  $\phi_k(t) = \phi_{k+1}(t) + K_k$ ;  $K_k \in \mathbb{R}$  such that one could for instance ‘drive’ the system with a homogeneous external field and yet it would hold that  $c_k(t) = 0 \quad \forall t$ .

## A.2 Solution of the integral (2.24)

We use the substitutions  $\eta = \sin(x)$ ,  $a = \frac{2t}{\sqrt{LC}}$ ,  $\varphi = \frac{2}{\sqrt{LC}}$  and get

$$\begin{aligned}
I_\infty(t) &= \frac{Q_L - Q_R}{\sqrt{LC}} \frac{1}{\pi} \int_0^{\frac{\pi}{2}} \frac{\sin\left(\frac{2}{\sqrt{LC}} \sin(x) t\right)}{\sin(x)} dx \\
&= \frac{Q_L - Q_R}{\sqrt{LC}} \frac{1}{\pi} \int_0^1 \frac{\sin(a\eta)}{\eta \sqrt{1-\eta^2}} d\eta \\
&= -\frac{Q_L - Q_R}{\sqrt{LC}} \frac{1}{4\pi} a\pi [-2\mathcal{J}_0(a) + \pi\mathcal{J}_0(a)\mathcal{H}_1(a) - \pi\mathcal{J}_1(a)\mathcal{H}_0(a)] \\
&= \frac{(Q_L - Q_R)t}{2LC} [\mathcal{J}_0(\varphi t) (2 - \pi\mathcal{H}_1(\varphi t)) + \pi\mathcal{J}_1(\varphi t) \mathcal{H}_0(\varphi t)] \quad (\text{A.10})
\end{aligned}$$

where  $\mathcal{J}_n(x)$  are the Bessel functions of the first kind and  $\mathcal{H}_n(x)$  denotes the Struve function, both described for instance in [50, 91]. The solution of the integral in the second last transformation was found with the help of Mathematica and can be checked by plugging in the integral definitions of the mentioned functions.

## A.3 Solution of the integral (2.32)

As in [app. A.2] we use the substitutions  $\eta = \sin(x)$ ,  $a = \frac{2t}{\sqrt{LC}}$ ,  $\varphi = \frac{2}{\sqrt{LC}}$  and get

$$\begin{aligned}
I_{\text{dot},\infty}(t) &= \frac{Q_L - Q_R}{\sqrt{LC}} \frac{1}{\pi} \int_0^1 \frac{\sin(a\eta)}{\eta} \cos^2(\arcsin(\eta)) \frac{d\eta}{dx} dx \\
&= \frac{Q_L - Q_R}{\sqrt{LC}} \frac{1}{\pi} \int_0^1 \frac{\sin(a\eta)}{\eta} (1-\eta^2) \sqrt{1-\eta^2} d\eta \\
&= \frac{Q_L - Q_R}{\sqrt{LC}} [\mathcal{J}_1(a) \left( \frac{\pi a}{4} \mathcal{H}_0(a) - \frac{1}{a^2} - \frac{1}{2} \right) \\
&\quad + \mathcal{J}_0(a) \left( \frac{a}{2} + \frac{1}{2a} - \frac{\pi a}{4} \mathcal{H}_1(a) \right)] \\
&= \frac{Q_L - Q_R}{\sqrt{LC}} [\mathcal{J}_1(\varphi t) \left( \frac{\pi \varphi t}{4} \mathcal{H}_0(\varphi t) - \frac{1}{\varphi^2 t^2} - \frac{1}{2} \right) \\
&\quad + \mathcal{J}_0(\varphi t) \left( \frac{\varphi t}{2} + \frac{1}{2\varphi t} - \frac{\pi \varphi t}{4} \mathcal{H}_1(\varphi t) \right)] \quad (\text{A.11})
\end{aligned}$$

where  $\mathcal{J}_n(x)$  are the Bessel functions of the first kind and  $\mathcal{H}_n(x)$  denotes the Struve function, both described for instance in [50, 91]. The solution of

the integral was found with the help of Mathematica and can be checked by plugging in the integral definitions of the mentioned functions.

## A.4 Approximations of the Bessel and Struve functions

The Bessel functions of the first kind and Struve functions have the following approximations which become exact for  $x \rightarrow \infty$

$$\begin{aligned}
 \mathcal{J}_0(x) &= \sqrt{\frac{2}{\pi x}} \cos\left(x - \frac{\pi}{4}\right) + \mathcal{O}\left(\frac{1}{x}\right), \\
 \mathcal{J}_1(x) &= \sqrt{\frac{2}{\pi x}} \cos\left(x - \frac{3}{4}\pi\right) + \mathcal{O}\left(\frac{1}{x}\right), \\
 \mathcal{H}_0(x) &= \sqrt{\frac{2}{\pi x}} \sin\left(x - \frac{\pi}{4}\right) + \mathcal{O}\left(\frac{1}{x}\right), \\
 \mathcal{H}_1(x) &= \frac{2}{\pi} - \sqrt{\frac{2}{\pi x}} \cos\left(x - \frac{\pi}{4}\right) + \mathcal{O}\left(\frac{1}{x}\right).
 \end{aligned} \tag{A.12}$$

Using these expressions together with equation (2.25) leads to

$$\begin{aligned}
 \bar{I}_{\text{cl}} &= \lim_{t \rightarrow \infty} I_{\infty}(t) \\
 &= \lim_{t \rightarrow \infty} \frac{Q_L - Q_R}{2LC} t \cdot \frac{2}{\varphi t} \left[ \cos^2\left(\varphi t - \frac{\pi}{4}\right) \right. \\
 &\quad \left. + \cos\left(\varphi t - \frac{3\pi}{4}\right) \sin\left(\varphi t - \frac{\pi}{4}\right) + \mathcal{O}\left(t^{-\frac{3}{2}}\right) \right] \\
 &= \frac{Q_L - Q_R}{2\sqrt{LC}} \lim_{t \rightarrow \infty} \underbrace{\left[ \cos^2\left(\varphi t - \frac{\pi}{4}\right) + \sin^2\left(\varphi t - \frac{\pi}{4}\right) \right]}_1 + \mathcal{O}\left(\frac{1}{\sqrt{t}}\right).
 \end{aligned} \tag{A.13}$$

Note that the order terms have been rewritten

$$\mathcal{O}\left(\frac{1}{t}\right) \rightarrow \sqrt{\frac{2}{\pi \varphi t}} \mathcal{O}\left(\frac{1}{\sqrt{t}}\right) \tag{A.14}$$

which explains the unexpected fractional value. One finally obtains expression (2.27) for the stationary current which does not provide an approximate expression for the short-time behaviour of the current, since all time-dependent terms cancel out.



Instead, one can use the asymptotic series expansions from [50, 92] and the approximation of  $\mathcal{H}_1(x)$  from [51]

$$\begin{aligned}
\mathcal{J}_0(x) &= \frac{(8x-1)\cos(x) + (8x+1)\sin(x)}{8\sqrt{\pi x^3}} + \mathcal{O}\left(\frac{1}{x^{\frac{5}{2}}}\right), \\
\mathcal{J}_1(x) &= \frac{(3-8x)\cos(x) + (3+8x)\sin(x)}{8\sqrt{\pi x^3}} + \mathcal{O}\left(\frac{1}{x^{\frac{5}{2}}}\right), \\
\mathcal{H}_0(x) &= \frac{8x\sqrt{\pi}(\sin(x) - \cos(x)) + 16\sqrt{x} - \sqrt{\pi}}{8\pi\sqrt{x^3}} + \mathcal{O}\left(\frac{1}{x^{\frac{5}{2}}}\right), \\
\mathcal{H}_1(x) &\approx \frac{2}{\pi} + \frac{\left(\frac{16}{\pi} - 5\right)\sin x}{x} \\
&\quad + \frac{\left(12 - \frac{36}{\pi}\right)(1 - \cos(x))}{x^2} - \mathcal{J}_0(x)
\end{aligned} \tag{A.15}$$

whereas one can plug the approximate expression for  $\mathcal{J}_0(x)$  into the equation for  $\mathcal{H}_1(x)$ . Unlike  $\mathcal{J}_0(x)$ ,  $\mathcal{J}_1(x)$  and  $\mathcal{H}_0(x)$ , the approximation of  $\mathcal{H}_1(x)$  stems from [51] since the simple asymptotic approximation has a higher error for small  $x$  as shown in figure A.1. Using the given equation for  $\mathcal{H}_1(x)$  is also crucial for an acceptable error for the approximative current expression (error shown in figure A.2). Aarts and Janssen [51] state that the approximation of  $\mathcal{H}_1(x)$  has a squared approximation error on  $[0, \infty)$  equal to  $2.2 \cdot 10^{-4}$  by Parseval's formula but cannot give a precise behaviour of the remainder for  $x \rightarrow \infty$ . Using the approximations (A.15), equation (2.25) for  $I_\infty(t)$  can be transformed into expression (2.29) for  $t \gg 1$ . Figure A.2 shows the relative error between the exact solution (2.25) and the approximation curve (2.29).

## A.5 Remainder approximation for the Taylor series expansion

One can use Lagrange's remainder approximation for the Taylor series expansion around zero [90, 50]

$$T_n^{[f(x)]}(x) = \sum_{i=0}^n \frac{f^{(i)}(x)|_{x=\gamma}}{i!} x^i \tag{A.16}$$

which is given by

$$R_n^{[f(x)]}(x, \gamma) = \frac{f^{(n+1)}(x)|_{x=\gamma}}{(n+1)!} x^{n+1} \tag{A.17}$$

where an upper index ( $n$ ) in round brackets denotes the  $n$ -th derivation and  $\gamma \in [0, x] \subset \mathbb{R}$ . In order to give an upper or lower border for the error, one

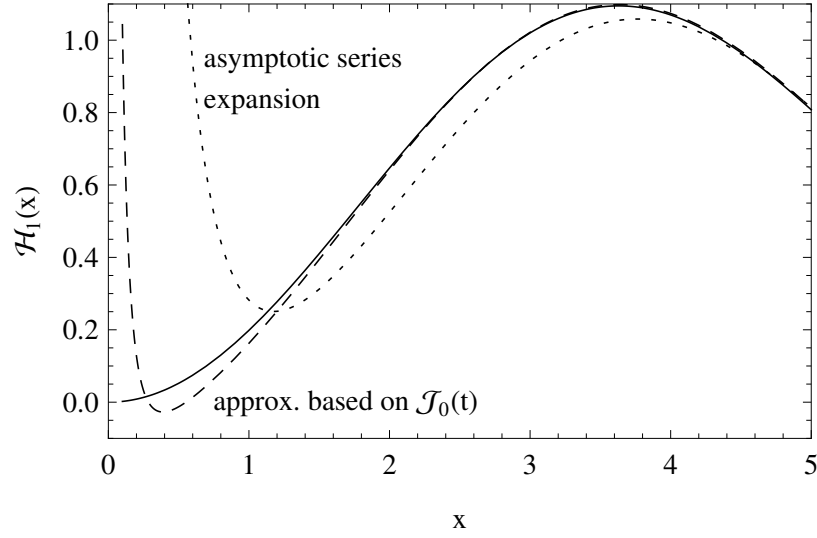


Figure A.1. Solid curve: Struve function  $\mathcal{H}_1(x)$ . Two approximations are shown: See [93] for the expression of the asymptotic approximation (dotted line) and equation (A.15) for the approximation based on  $\mathcal{J}_0(x)$  (dashed line).

has to choose those  $\gamma$  that maximize, respectively minimize the remainder. The maximal error of an  $n$ -th order Taylor series expansion of a function  $f(x)$  in the vicinity of zero is given by

$$E_n[f(x)] = \frac{\max_{\gamma} (|R_n^{[f(x)]}(x, \gamma)|)}{|f(x)|}. \quad (\text{A.18})$$

The approximation  $\sin(x) \approx x$  leads to  $R_1^{[\sin(x)]}(x, \gamma) = -x^2 \sin(\gamma)/2$  such that the maximal error for  $0 \leq x \leq \frac{\pi}{2}$  is given by

$$E_1[\sin(x)] = \frac{x^2}{2}. \quad (\text{A.19})$$

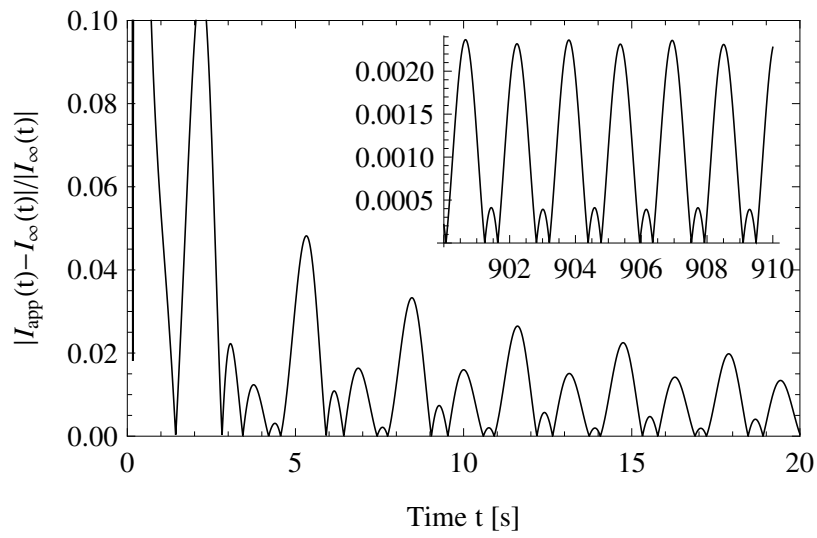


Figure A.2. Error  $\left| \frac{I_{\text{app}}(t) - I_{\infty}(t)}{I_{\infty}(t)} \right|$  with  $L = C = 1$ ,  $Q_L = 1$  and  $Q_R = -1$ .



## APPENDIX B

### Non-equilibrium simulations

#### B.1 Perturbation theory for small and large biases

As we change the applied potential bias in both setups (I) and (II), the Hamiltonian is actually time-dependent and we can write it as

$$\hat{H}(t) = \hat{H}_0 + \Delta\epsilon \hat{H}_1 \cdot h(t) \quad (\text{B.1})$$

where for setup (I)  $h(t) = \Theta(-t)$  and for setup (II)  $h(t) = \Theta(t)$  with  $\Theta(0) = 1$ . Thus, for setup (I) we initially (for times  $t < 0$ ) prepare the system in the ground state  $|\Psi_1\rangle$  of  $\hat{H}_0 + \Delta\epsilon \hat{H}_1$  and the time evolution for  $t \geq 0$  of the (expectation value of the) current is given by

$$J(t) = \langle \Psi_1 | \hat{J}(t) | \Psi_1 \rangle \quad \text{with} \quad \hat{J}(t) = e^{\frac{i}{\hbar} \hat{H}_0 t} \hat{J}_0 e^{-\frac{i}{\hbar} \hat{H}_0 t}. \quad (\text{B.2})$$

For small applied potentials  $\Delta\epsilon$ , and if the ground state of  $\hat{H}_0$  is not degenerate, it holds

$$|\Psi_1\rangle = |\Psi_0\rangle + \Delta\epsilon \cdot \frac{1}{\hat{H}_0 - E_0} \hat{M}_1 |\Psi_0\rangle + \mathcal{O}(\Delta\epsilon^2) \quad (\text{B.3})$$

with

$$\hat{M}_1 = \hat{H}_1 - \langle \Psi_0 | \hat{H}_1 | \Psi_0 \rangle \quad (\text{B.4})$$

where  $|\Psi_0\rangle$  is the ground state of  $\hat{H}_0$ , and  $E_0$  the corresponding ground energy. Plugging expression (B.3) into equation (B.2) one gets

$$\begin{aligned} J(t) = & \underbrace{\langle \Psi_0 | \hat{J}(t) | \Psi_0 \rangle}_{= \langle \Psi_0 | \hat{J}_0 | \Psi_0 \rangle} + \Delta\epsilon \cdot \langle \Psi_0 | \left( \hat{J}(t) \frac{1}{\hat{H}_0 - E_0} \hat{M}_1 \right. \\ & \left. + \hat{M}_1 \frac{1}{\hat{H}_0 - E_0} \hat{J}(t) \right) | \Psi_0 \rangle + \mathcal{O}(\Delta\epsilon^2) \end{aligned} \quad (\text{B.5})$$

For setup (II) the system is initially prepared in the ground state  $|\Psi_0\rangle$  of  $\hat{H}_0$  and evolved in time with  $\hat{H}_2 = \hat{H}_0 + \Delta\epsilon\hat{H}_1$ . Thus, it holds

$$J(t) = \langle\Psi_0|\hat{J}(t)|\Psi_0\rangle \quad \text{with} \quad \hat{J}(t) = e^{\frac{i}{\hbar}\hat{H}_2t}\hat{J}_0e^{-\frac{i}{\hbar}\hat{H}_2t} \quad (\text{B.6})$$

and using time-dependent perturbation theory

$$e^{-\frac{i}{\hbar}\hat{H}_2t} = e^{-\frac{i}{\hbar}\hat{H}_0t} \left( 1 - \Delta\epsilon \cdot \frac{i}{\hbar} \int_0^t \hat{H}_1(t')dt' + \mathcal{O}(\Delta\epsilon^2) \right) \quad (\text{B.7})$$

one gets after a short calculation

$$\begin{aligned} J(t) = \langle\Psi_0|\hat{J}_0|\Psi_0\rangle + \Delta\epsilon \cdot \langle\Psi_0| & \left( (\hat{J}(t) - \hat{J}_0) \frac{1}{\hat{H}_0 - E_0} \hat{H}_1 \right. \\ & \left. + \hat{H}_1 \frac{1}{\hat{H}_0 - E_0} (\hat{J}(t) - \hat{J}_0) \right) |\Psi_0\rangle + \mathcal{O}(\Delta\epsilon^2) \end{aligned} \quad (\text{B.8})$$

We note that up to the order  $\mathcal{O}(\Delta\epsilon)$ , equation (B.5) for setup (I) and equation (B.5) for setup (II) are equal if  $\langle\Psi_0|\hat{H}_1|\Psi_0\rangle = 0$  and  $\hat{J}_0 \propto [\hat{H}_0, \hat{H}_1]$ , which is given (or can easily be achieved) for our models and setups.

For large biases  $\Delta\epsilon$  and setup (II), the time evolution is determined by  $\hat{H} = \lambda\hat{H}_0 + \hat{H}_1$ . Time-dependent perturbation theory

$$e^{-\frac{i}{\hbar}\hat{H}t} = e^{-\frac{i}{\hbar}\hat{H}_1t} \left( 1 - \lambda \cdot \frac{i}{\hbar} \int_0^t e^{\frac{i}{\hbar}\hat{H}_1t'} \hat{H}_0 e^{-\frac{i}{\hbar}\hat{H}_1t'} dt' + \mathcal{O}(\lambda^2) \right) \quad (\text{B.9})$$

yields

$$J(t) = \langle\Psi_0|\hat{J}(t)|\Psi_0\rangle + \lambda \cdot \frac{i}{\hbar} \langle\Psi_0| \int_0^t [\hat{H}_0(t'), \hat{J}(t)] dt' |\Psi_0\rangle + \mathcal{O}(\lambda^2) \quad (\text{B.10})$$

with

$$\hat{J}(t) = e^{\frac{i}{\hbar}\hat{H}_1t} \hat{J}_0 e^{-\frac{i}{\hbar}\hat{H}_1t} \quad \text{and} \quad \hat{H}_0(t') = e^{\frac{i}{\hbar}\hat{H}_1t'} \hat{H}_0 e^{-\frac{i}{\hbar}\hat{H}_1t'}. \quad (\text{B.11})$$

Inserting (for instance) the Hamiltonian for the spinless fermion model (5.1), one can see that the expectation value of the current vanished for  $\Delta\epsilon \rightarrow \infty$ .

## B.2 Period of the rectangular oscillation in the tight-binding model

The following calculation has already been performed in [94]. The time evolution of the single particle reduced density matrix (3.10) is given by

$$\mathcal{G}_{ij}(t) = \exp\left(-\frac{i}{\hbar}\varepsilon_q t\right) \mathcal{G}_{kq}(0) \exp\left(\frac{i}{\hbar}\varepsilon_k t\right) \quad (\text{B.12})$$

in the eigenbasis of a time-constant single particle Hamiltonian  $H^{(1)}$ .  $\Psi_{k,i}$  denotes the  $i$ -th component of the  $k$ -th eigenvector of  $H^{(1)}$  and  $\varepsilon_k$  the corresponding eigenvalue. A Fourier transformation gives

$$\tilde{\mathcal{G}}_{kq}(\omega) = \delta[\varepsilon_k - \varepsilon_q - \hbar\omega] \mathcal{G}_{kq}(0). \quad (\text{B.13})$$

For the tight-binding model with zero onsite potentials one has

$$\begin{aligned} \Psi_{k,i} &= \sqrt{\frac{2}{N+1}} \sin\left(\frac{ki\pi}{N+1}\right), \\ \varepsilon_k &= -2t_{\text{H}} \cos\left(\frac{k\pi}{N+1}\right). \end{aligned} \quad (\text{B.14})$$

The period of the largest (rectangular) oscillation is then given by

$$T^{\text{max}} = \frac{\pi\hbar}{t_{\text{H}} \sin\left(\frac{\pi}{N+1}\right)} \approx \hbar \cdot \frac{N}{t_{\text{H}}} \quad \text{for } N \gg 1. \quad (\text{B.15})$$

### B.3 Current in the infinite tight-binding model

The expectation value of the current for setup (I) and for initial conditions like in figure 3.4 (one completely filled and one completely empty half) is for  $N \rightarrow \infty$  given by [15, 56]

$$J_{\text{F}}^k(t) = \frac{2et_{\text{H}}}{\hbar} \sum_{l=k-\frac{N}{2}}^{\infty} \mathcal{J}_l(\omega t) \mathcal{J}_{l+1}(\omega t) \quad (\text{B.16})$$

where  $k$  denotes the site,  $\omega = 2t_{\text{H}}/\hbar$  and  $\mathcal{J}_l(z)$  are the Bessel functions of the first kind. Reformulating the sum and utilizing the Bessel recursion relation

$$\frac{2l}{z} \mathcal{J}_l(z) = \mathcal{J}_{l+1}(z) + \mathcal{J}_{l-1}(z) \quad (\text{B.17})$$

gives for  $z \neq 0$  and  $k = N/2$

$$J_{\text{F}}(\omega t) := J_{\text{F}}^{N/2}(\omega t) = \frac{4et_{\text{H}}}{\hbar\omega t} \sum_{l=0}^{\infty} [(\mathcal{J}_{2l+1}(\omega t))^2 \cdot (2l+1)]. \quad (\text{B.18})$$

With [50]

$$\begin{aligned} &\sum_{l=0}^{\infty} (4l+2\nu+2) \mathcal{J}_{2l+\nu+1}(z) \mathcal{J}_{2l+\nu+1}(w) \\ &= \frac{zw}{z^2-w^2} [z \mathcal{J}_{\nu+1}(z) \mathcal{J}_{\nu}(w) - w \mathcal{J}_{\nu}(z) \mathcal{J}_{\nu+1}(w)] \end{aligned} \quad (\text{B.19})$$

for  $\text{Re}(\nu) > -1$  and  $z \neq w$ , the current is given by

$$J_{\text{F}}(t) = \frac{2et_{\text{H}}}{\hbar} \lim_{t' \rightarrow t} \frac{\omega t \mathcal{J}_1(\omega t) \mathcal{J}_0(\omega t') - \omega t' \mathcal{J}_0(\omega t) \mathcal{J}_1(\omega t')}{(\pi \omega t')^{-1} ((\omega t)^2 - (\omega t')^2)}. \quad (\text{B.20})$$

Applying l'Hôspital's rule one gets

$$J_{\text{F}}(t) = \frac{et_{\text{H}}}{\hbar} \omega t [(\mathcal{J}_0(\omega t))^2 + (\mathcal{J}_1(\omega t))^2]. \quad (\text{B.21})$$



## APPENDIX C

### TEBD update scheme

In the following part SVD and  $\text{TEBD}_n$  are defined as functions and written in pseudo-code. Let  $\chi_c^l$  be the Schmidt dimension for site  $l$  and  $\chi_c^l \leq \chi_c \forall l$ .  $m$  denotes the local dimension,  $N$  the number of lattice sites,  $i, j, k, o, p = 1, 2, \dots, m$ ,  $\xi_{l+1} = 1, 2, \dots, m \cdot \chi_c^{l+1}$  and  $U^l$  is the time evolving operator for the  $l$ -th bond. With  $\alpha = 1, 2, \dots, \chi_c^{l-1}$ ,  $\beta = 1, 2, \dots, \chi_c^l$  and  $\gamma = 1, 2, \dots, \chi_c^{l+1}$  the singular value decomposition (SVD) is defined as:

$$\begin{aligned} \phi_\beta &\leftarrow \{ \text{EW} [\rho_{xy}^{(R)}] : \text{EW} [\rho_{xy}^{(R)}] > \varepsilon \text{ and } \beta \leq \chi_c \} \\ \Phi_\beta^{\xi_{l+1}} &\leftarrow \{ \text{EV} [\rho_{xy}^{(R)}]_\beta^{\xi_{l+1}} : \text{EW} [\rho_{xy}^{(R)}] > \varepsilon \text{ and } \beta \leq \chi_c \} \end{aligned}$$

where  $\Phi_\beta^{\xi_{l+1}}$  is the  $\xi_{l+1}$ -th component  
of the  $\beta$ -th eigenvector

$$\begin{aligned} \chi_c^l &\leftarrow \text{size}(\phi_\beta) \\ R &\leftarrow \sum_{\beta=1}^{\chi_c^l} \phi_\beta \quad (\text{renormalization factor}) \\ \lambda_\beta^{[l]} &\leftarrow \sqrt{\phi_\beta / R} \end{aligned}$$

An eigenvalue of  $\rho^{(R)}$  is only kept if it is larger than  $\varepsilon$  (a small number dependent on the system) and it the maximal Schmidt dimension  $\chi_c$  is not exceeded. Accordingly, all eigenvectors whose corresponding eigenvalues do not fulfill these requirements are discarded. We further define  $\text{TEBD}_1$  with  $l = 1$ :

$$\begin{aligned} \theta_{ij\gamma} &\leftarrow \sum_{o,p=1}^m \sum_{\beta=1}^{\chi_c} \Gamma_\beta^{[l]o} \lambda_\beta^{[l]} \Gamma_{\beta\gamma}^{[l+1]p} \lambda_\gamma^{[l+1]} U_{ij}^{lop} \\ \rho_{\substack{x=j(\chi_c^{l+1}-1)+\gamma, \\ y=j'(\chi_c^{l+1}-1)+\gamma'}}^{(R)} &\leftarrow \sum_{i=1}^m \theta_{ij\gamma} \cdot \theta_{ij'\gamma'}^* \\ &\text{call SVD;} \end{aligned}$$

$$\Gamma_{\beta\gamma}^{[l+1]j} \leftarrow \frac{\Phi_{\beta}^{j(\chi_c^{l+1}-1)+\gamma}}{\lambda_{\gamma}^{[l+1]}}$$

$$\Gamma_{\beta}^{[l]i} \leftarrow \frac{1}{\lambda_{\beta}^{[l]}} \cdot \sum_{j=1}^m \sum_{\gamma=1}^{\chi_c^{l+1}} \theta_{ij\gamma} \Phi_{\beta}^{j(\chi_c^{l+1}-1)+\gamma}$$

and TEBD<sub>l</sub>:

$$\Theta_{\alpha ij\gamma} \leftarrow \sum_{o,p=1}^m \sum_{\beta=1}^{\chi_c^l} \lambda_{\alpha}^{[l-1]} \Gamma_{\alpha\beta}^{[l]o} \lambda_{\beta}^{[l]} \Gamma_{\beta\gamma}^{[l+1]p} \lambda_{\gamma}^{[l+1]} U_{ij}^{lop}$$

$$\rho_{\substack{x=j(\chi_c^{l+1}-1)+\gamma, \\ y=j'(\chi_c^{l+1}-1)+\gamma'}}^{(R)} \leftarrow \sum_{i=1}^m \sum_{\alpha=1}^{\chi_c^{l-1}} \Theta_{\alpha ij\gamma} \cdot \Theta_{\alpha ij'\gamma'}^*$$

call SVD;

$$\Gamma_{\beta\gamma}^{[l+1]j} \leftarrow \frac{\Phi_{\beta}^{j(\chi_c^{l+1}-1)+\gamma}}{\lambda_{\gamma}^{[l+1]}}$$

$$\Gamma_{\alpha\beta}^{[l]i} \leftarrow \frac{1}{\lambda_{\alpha}^{[l-1]} \lambda_{\beta}^{[l]}} \cdot \sum_{j=1}^m \sum_{\gamma=1}^{\chi_c^{l+1}} \Theta_{\alpha ij\gamma} \Phi_{\beta}^{j(\chi_c^{l+1}-1)+\gamma}$$

and TEBD<sub>n-1</sub> with  $l = n - 1$ :

$$\Omega_{\alpha ij} \leftarrow \sum_{o,p=1}^m \sum_{\beta=1}^{\chi_c^l} \lambda_{\alpha}^{[l-1]} \Gamma_{\alpha\beta}^{[l]o} \lambda_{\beta}^{[l]} \Gamma_{\beta}^{[l+1]p} U_{ij}^{lop}$$

$$\rho_{x=j,y=j'}^{(R)} \leftarrow \sum_{i=1}^m \sum_{\alpha=1}^{\chi_c^{l-1}} \Omega_{\alpha ij} \cdot \Omega_{\alpha ij'}^*$$

call SVD;

$$\Gamma_{\beta}^{[l+1]j} \leftarrow \Phi_{\beta}^j$$

$$\Gamma_{\alpha\beta}^{[l]i} \leftarrow \frac{1}{\lambda_{\alpha}^{[l-1]} \lambda_{\beta}^{[l]}} \cdot \sum_{j=1}^m \sum_{\gamma=1}^{\chi_c^{l+1}} \Omega_{\alpha ij} \Phi_{\beta}^j$$

for the TEBD update scheme given in (4.12).

## Bibliography

- [1] S. Iijima, Nature **354**, 56 (1991), *Helical microtubules of graphitic carbon*
- [2] S. J. Tans, M. H. Devoret, H. J. Dai, A. Thess, R. E. Smalley, L. J. Geerligs, and C. Dekker, Nature **386**, 474 (1997), *Individual single-wall carbon nanotubes as quantum wires*
- [3] M. Bockrath, D. H. Cobden, P. L. McEuen, N. G. Chopra, A. Zettl, A. Thess, and R. E. Smalley, Science **275**, 1922 (1997), *Single-electron transport in ropes of carbon nanotubes*
- [4] S. Tomonaga, Prog. Theor. Phys. **5**, 544 (1950), *Remarks on Bloch's Method of Sound Waves applied to Many-Fermion Problems*
- [5] T. Giamarchi, *Quantum Physics in One Dimension*, Clarendon Press, Oxford (2003)
- [6] K. Schönhammer, J. Phys.: Condens. Matter **14**, 12783 (2002), *The Luttinger liquid concept for interacting electrons in one dimension*
- [7] K. Schönhammer, in *Strong Interactions in Low Dimensions*, edited by D. Baeriswyl and L. Degiorgi (Kluwer Academic Publishers, Dordrecht, 2004)
- [8] J. Kong, E. Yenilmez, T. W. Tombler, W. Kim, H. J. Dai, R. B. Laughlin, L. Liu, C. S. Jayanthi, and S. Y. Wu, Phys. Rev. Lett. **87**, 106801 (2001), *Quantum interference and ballistic transmission in nanotube electron waveguides*
- [9] J. N. Crain and F. J. Himpsel, Appl. Phys. A **82**, 431 (2006), *Low-dimensional electronic states at silicon surfaces*
- [10] P. Schmitteckert, Phys. Rev. B **70**, 121302 (2004), *Nonequilibrium electron transport using the density matrix renormalization group method*
- [11] F. Heidrich-Meisner, A.E. Feiguin, and E. Dagotto, Phys. Rev. B **79**, 235336 (2009), *Real-time simulations of nonequilibrium transport in the single-impurity Anderson model*
- [12] A. Kawabata, Rep. Prog. Phys. **70**, 219 (2007), *Electron conduction in one-dimension*

- [13] A. Yacoby, in *Strong Interactions in Low Dimensions*, edited by D. Baeriswyl and L. Degiorgi (Kluwer Academic Publishers, Dordrecht, 2004)
- [14] X. Zotos and P. Prelovsek, in *Strong Interactions in Low Dimensions*, edited by D. Baeriswyl and L. Degiorgi (Kluwer Academic Publishers, Dordrecht, 2004)
- [15] T. Antal, Z. Rácz, A. Rákos, and G.M. Schütz, Phys. Rev. E **59**, 4912 (1999), *Transport in the XX chain at zero temperature: Emergence of flat magnetization profiles*
- [16] H. Bethe, Z. Phys. **71**, 205 (1931), *Zur Theorie der Metalle*
- [17] V. E. Korepin, N. M. Bogoliubov, and A. G. Izergin, *Quantum Inverse Scattering Method and Correlation Functions*, Cambridge Univ. Press, Cambridge (1993)
- [18] T. Deguchi, F. H. L. Essler, F. Göhmann, A. Klümper, V.E. Korepin, and K. Kusakabe, Phys. Rep. **331**, 197 (2000), *Thermodynamics and excitations of the one-dimensional Hubbard model*
- [19] C. L. Kane and M. P. A. Fisher, Phys. Rev. Lett. **68**, 1220 (1992), *Transport in a one-channel Luttinger liquid*
- [20] A. Furusaki and N. Nagaosa, Phys. Rev. B **47**, 4631 (1993), *Single-barrier problem and Anderson localization in a one-dimensional interacting electron system*
- [21] G. Barak, H. Steinberg, L.N. Pfeiffer, K.W. West, L. Glazman, F. von Oppen, and A. Yacoby, Nature Physics **6**, 489 (2010), *Interacting electrons in one dimension beyond the Luttinger-liquid limit*
- [22] E. Boulat, H. Saleur, and P. Schmitteckert, Phys. Rev. Lett. **101**, 140601 (2008), *Twofold Advance in the Theoretical Understanding of Far-From-Equilibrium Properties of Interacting Nanostructures*
- [23] F. Heidrich-Meisner, G.B. Martins, K.A. Al-Hassanieh, A.E. Feiguin, G. Chiappe, E.V. Anda, and E. Dagotto, Eur. J. Phys. B **67**, 527 (2009), *Transport through quantum dots: a combined DMRG and embedded-cluster approximation study*
- [24] S. T. Carr, D. A. Bagrets, and P. Schmitteckert, Phys. Rev. Lett. **107**, 206801 (2011), *Full Counting Statistics in the Self-Dual Interacting Resonant Level Model*
- [25] G. Vidal, Phys. Rev. Lett. **91**, 147902 (2003), *Efficient Classical Simulation of Slightly Entangled Quantum Computations*

- [26] G. Vidal, Phys. Rev. Lett. **93**, 040502 (2004), *Efficient Simulation of One-Dimensional Quantum Many-Body Systems*
- [27] U. Schollwöck and S.R. White in *Effective models for low-dimensional strongly correlated systems*, edited by G. G. Batrouni and D. Poilblanc (AIP, New York, 2006)
- [28] R. M. Noack, S.R. Manmana, S. Wessel, A. and Muramatsu, in *Computational Many-Particle Physics*, edited by H. Fehske, R. Schneider, and A. Weiße (Springer, Berlin, 2008)
- [29] U. Schollwöck, Annals of Physics **326**, 96 (2011), *The density-matrix renormalization group in the age of matrix product states*
- [30] A. J. Daley, C. Kollath, U. Schollwöck, and G. Vidal, J. Stat. Mech. **2004**, 04005 (2004), *Time-dependent density-matrix renormalization-group using adaptive effective Hilbert spaces*
- [31] E. Jeckelmann, in *Computational Many-Particle Physics*, edited by H. Fehske, R. Schneider, and A. Weiße (Springer, Berlin, 2008)
- [32] M. A. Cazalilla and J. B. Marston, Phys. Rev. Lett. **88**, 256403 (2002), *Time-Dependent Density-Matrix Renormalization Group: A Systematic Method for the Study of Quantum Many-Body Out-of-Equilibrium Systems*
- [33] H. G. Luo, T. Xiang and X. Q. Wang, Phys. Rev. Lett. **91**, 049701 (2003), *Comment on ‘Time-Dependent Density-Matrix Renormalization Group: A Systematic Method for the Study of Quantum Many-Body Out-of-Equilibrium Systems’*
- [34] M. A. Cazalilla and J. B. Marston, Phys. Rev. Lett. **91**, 049702 (2003), *Cazalilla and Marston Reply*
- [35] S. Kirino, T. Fujii, J. Zhao, and K. Ueda, J. Phys. Soc. Japan **77**, 084704 (2008), *Time-Dependent DMRG Study on Quantum Dot under a Finite Bias Voltage*
- [36] S. Kirino and K. Ueda, J. Phys. Soc. Japan **79**, 093710 (2010), *Nonequilibrium Current in the One Dimensional Hubbard Model at Half-Filling*
- [37] F. Heidrich-Meisner, I. González, K.A. Al-Hassanieh, A.E. Feiguin, M.J. Rozenberg, and E. Dagotto, Phys. Rev. B **82**, 205110 (2010), *Nonequilibrium electronic transport in a one-dimensional Mott insulator*
- [38] M. Žnidarič, Phys. Rev. Lett. **106**, 220601 (2011), *Spin Transport in a One-Dimensional Anisotropic Heisenberg Model*
- [39] K. A. Al-Hassanieh, A. E. Feiguin, J. A. Riera, C. A. Büsser, and E. Dagotto, Phys. Rev. B **73**, 195304 (2006), *Adaptive time-dependent*

- density-matrix renormalization-group technique for calculating the conductance of strongly correlated nanostructures*
- [40] G. Hager, E. Jeckelmann, H. Fehske, and G. Wellein, *Journal of Computational Physics* **194**, 795 (2004), *Parallelization Strategies for Density Matrix Renormalization Group Algorithms on Shared-Memory Systems*
  - [41] P. Schmitteckert and G. Schneider in *High Performance Computing in Science and Engineering '06*, edited by W. E. Nagel, W. Jäger, and M. Resch (Springer, Berlin, 2007)
  - [42] A. Branschädel, G. Schneider, and P. Schmitteckert, *Annalen der Physik* **522**, 657 (2010), *Conductance of inhomogeneous systems: Real-time dynamics*
  - [43] I. Bâldea and H. Köppel, *Phys. Rev. B* **81**, 193401 (2010), *Sources of negative differential resistance in electric nanotransport*
  - [44] S. Tornow, R. Bulla, F. B. Anders, and A. Nitzan, *Phys. Rev. B* **78**, 035434 (2008), *Dissipative two-electron transfer: A numerical renormalization group study*
  - [45] G. Pratviel and B. Meunier, *Chem.-Eur. J.* **12**, 6018 (2006), *Guanine oxidation: one- and two-electron reactions*
  - [46] R. Hirota and K. Suzuki, *Proc. IEEE* **61**, 1483 (1973), *Theoretical and experimental studies of lattice solitons in nonlinear lumped networks*
  - [47] M. Toda, *Physics Reports* **18**, 1 (1975), *Studies of a non-linear lattice*
  - [48] A. C. Singer and A. V. Oppenheim, *International Journal of Bifurcation and Chaos* **9**, 571 (1999), *Circuit implementations of soliton systems*
  - [49] G. L. Ingold and Y. V. Nazarov, in *Single Charge Tunnelling*, edited by H. Grabert and M.H. Devoret (Plenum Press, New York, 1992); *Preprint arXiv:cond-mat/0508728*
  - [50] A. Abramowitz and I. A. Stegun, *Handbook of Mathematical Functions*, Dover Publications, New York (1972)
  - [51] R. M. Aarts and A. J. E. M. Janssen, *J. Acoust. Soc. Am.* **113**, 2635 (2003), *Approximation of the Struve function  $H_1$  occurring in impedance calculations*
  - [52] J. C. Slater and G. F. Koster, *Physical Review* **94**, 1498 (1954), *Simplified LCAO method for the Periodic Potential Problem*
  - [53] Y. Xue, S. Datta, and M. A. Ratner, *Chem. Phys.* **281**, 151 (2002) *First-Principles Based Matrix-Green's Function Approach to Molecular Electronic Devices: General Formalism*

- [54] G. D. Mahan, *Many-Particle Physics* 3.Ed., Kluwer Academic / Plenum Publishers, New York (2000)
- [55] E. Perfetto, G. Stefanucci, and M. Cini, Phys. Rev. Lett. **105**, 156802 (2010), *Correlation-Induced Memory Effects in Transport Properties of Low-Dimensional Systems*
- [56] V. Hunyadi, Z. Rácz, and L. Sasvári, Phys. Rev. E **69**, 066103 (2004), *Dynamic scaling of fronts in the quantum XX chain*
- [57] D. Gobert, C. Kollath, U. Schollwöck, and G. Schütz, Phys. Rev. E **71**, 036102 (2005), *Real-time dynamics in spin-1/2 chains with adaptive time-dependent density matrix renormalization group*
- [58] S. Langer, F. Heidrich-Meisner, J. Gemmer, I. P. McCulloch, and U. Schollwöck, Phys. Rev. B **79**, 214409 (2009), *Real-time study of diffusive and ballistic transport in spin- 1/2 chains using the adaptive time-dependent density matrix renormalization group method*
- [59] N. Hatano and M. Suzuki, in *Quantum Annealing and Other Optimization Methods*, edited by A. Das and B. K. Chakrabarti (Springer, Berlin, 2005)
- [60] A. Kawabata, J. Phys. Soc. Japan **65**, 30 (1996), *On the Renormalization of Conductance in Tomonaga-Luttinger Liquid*
- [61] I. Safi and H. J. Schulz, Phys. Rev. B **52**, 17040 (1995), *Transport in an inhomogeneous interacting one-dimensional system*
- [62] D. L. Maslov and M. Stone, Phys. Rev. B **52**, 5539 (1995), *Landauer conductance of Luttinger liquids with leads*
- [63] V. V. Ponomarenko, Phys. Rev. B **52**, 8666 (1995), *Renormalization of the one-dimensional conductance in the Luttinger-liquid model*
- [64] K. Janzen, V. Meden, and K. Schönhammer, Phys. Rev. B **74**, 085301 (2006), *Influence of the contacts on the conductance of interacting quantum wires*
- [65] U. Schneider, L. Hackermüller, J. P. Ronzheimer, S. Will, S. Braun, T. Best, I. Block, E. Demler, S. Mandt, D. Rasch, and A. Rosch, Nature Physics **8**, 213 (2012), *Fermionic transport and out-of-equilibrium dynamics in a homogeneous Hubbard model with ultracold atoms*
- [66] M. C. Gutzwiller, Phys. Rev. Lett. **10**, 159 (1963), *Effect of Correlation on the Ferromagnetism of Transition Metals*
- [67] J. Hubbard, Proc. Roy. Soc. London A **276**, 238 (1963), *Electron Correlations in Narrow Energy Bands*

- [68] J. Kanamori, Prog. Theor. Phys. **30**, 275 (1963), *Electron Correlation and Ferromagnetism of Transition Metals*
- [69] E. Fradkin, *Field Theories of Condensed Matter Systems*, Addison-Wesley, Redwood City (1991)
- [70] J. E. Hirsch, R. L. Sugar, D. J. Scalapino, and R. Blankenbecler, Phys. Rev. B **26**, 5033 (1982), *Monte Carlo simulations of one-dimensional fermion systems*
- [71] M. Jarrell, Phys. Rev. Lett. **69**, 168 (1992), *Hubbard model in infinite dimensions: A quantum Monte Carlo study*
- [72] S. Daul und R. M. Noack, Zeitschrift für Physik B Condensed Matter **103**, 293 (1997), *DMRG study of ferromagnetism in a one-dimensional Hubbard model*
- [73] F. H. L. Essler, H. Frahm, F. Göhmann, A Klümper, and V. E. Korepin, *The One Dimensional Hubbard Model*, Cambridge Univ. Press, Cambridge (2005)
- [74] E. H. Lieb and F. Y. Wu, Phys. Rev. Lett. **20**, 1445 (1968), *Absence of Mott Transition in an Exact Solution of the Short-Range, One-Band Model in One Dimension* ; Erratum: Phys. Rev. Lett. **21**, 192 (1968)
- [75] H. J. Schulz, Phys. Rev. Lett. **64**, 2831 (1990), *Correlation exponents and the metal-insulator transition in the one-dimensional Hubbard model*
- [76] F. B. Anders and A. Schiller, Phys. Rev. Lett. **95**, 196801 (2005), *Real-Time Dynamics in Quantum-Impurity Systems: A Time-Dependent Numerical Renormalization-Group Approach*
- [77] E. G. Petrov, V. I. Teslenko, and V. May, Phys. Rev. E **68**, 061916 (2003), *Two-electron transfer reactions in proteins: Bridge-mediated and proton-assisted processes*
- [78] K. G. Wilson, Rev. Mod. Phys. **47**, 773 (1975), *The renormalization group: Critical phenomena and the Kondo problem*
- [79] H. R. Krishna-murthy, J. W. Wilkins, and K. G. Wilson, Phys. Rev. B **21**, 1003 (1980), Phys. Rev. B **21**, 1044 (1980), *Renormalization-group approach to the Anderson model of dilute magnetic alloys. I. and II. Static properties for the symmetric case*
- [80] F. B. Anders and A. Schiller, Phys. Rev. B **74**, 245113 (2006), *Spin precession and real-time dynamics in the Kondo model: Time-dependent numerical renormalization-group study*



- [81] R. Bulla, H.-J. Lee, N.-H. Tong and M. Vojta, Phys. Rev. B **71**, 045122 (2005), *Numerical renormalization group for quantum impurities in a bosonic bath*
- [82] <http://www.apfloat.org> (a big number class) - 64bit version (v2.41)
- [83] W. H. Press, S. A. Teukolsky, W. T. Vetterling, and B. P. Flannery, *Numerical Recipes: The Art of Scientific Computing*, Cambridge Univ. Press, Cambridge (2007)
- [84] R. Bulla, T. Costi, and T. Pruschke, Rev. Mod. Phys. **80**, 395 (2008), *Numerical renormalization group method for quantum impurity systems*
- [85] A. E. Feiguin and S. R. White, Phys. Rev. B **72**, 020404(R) (2005), *Time-step targeting methods for real-time dynamics using the density matrix renormalization group*
- [86] C. Zhang, E. Jeckelmann, and S. R. White, Phys. Rev. Lett. **80**, 2661 (1998), *Density Matrix Approach to Local Hilbert Space Reduction*
- [87] C. Guo, A. Weichselbaum, J. von Delft, and M. Vojta, Phys. Rev. Lett. **108**, 160401 (2012), *Critical and Strong-Coupling Phases in One- and Two-Bath Spin-Boson Models*
- [88] N. A. Zimbovskaya and M. R. Pederson, Phys. Rep. **509**, 1 (2011), *Electron transport through molecular junctions*
- [89] E.M. Stoudenmire and Steven R. White, Annu. Rev. Condens.Matter Phys. Vol.3, 111-128 (2012), *Studying Two-Dimensional Systems with the Density Matrix Renormalization Group*
- [90] I. N. Bronstein, K. A. Semendjajew, G. Musiol, H. Mühlig, *Taschenbuch der Mathematik*, Wissenschaftlicher Verlag Harry Deutsch, Frankfurt a.M. (2008)
- [91] Wolfram Research (Mathematica), <http://mathworld.wolfram.com/>
- [92] A. Erdélyi, *Asymptotic Expansions*, Dover Publications, New York, (1956)
- [93] Wolfram Research:
  - <http://functions.wolfram.com/PDF/BesselJ.pdf>
  - <http://functions.wolfram.com/PDF/StruveH.pdf>
- [94] M. Einhellinger, *Reduced density matrix spectra for electronic systems out of equilibrium*, diploma thesis, Institut für theoretische Physik der Leibniz Universität Hannover (2007)

## Acknowledgments

First and foremost I thank my advisor Prof. Eric Jeckelmann for making this thesis possible, for supporting all of the ideas I came up with and for spending a lot of time during discussions with me. Moreover, he always cared for the details wedded with my thesis and my activities as an employee of the ITP. He had shown me how to work thoroughly and accurate, publishing only well-proven theories and results. I always found him an inspiring example.

Second, I thank my friends and colleagues Alex Cojuhovski and Martin Paech for fruitful and entertaining conversations. Even more, I would particularly like to thank Alex Cojuhovski for introducing me into the MPS and TEBD formalism (so many times), for fighting with me figuratively and literally, and for so much more.

I also thank the *NTH school for contacts in nanosystems* for all the educational and financial support. Sincere thanks are given to Sabine Tornow and Prof. Gertrud Zwicknagl from the TU Braunschweig for the collaboration within the context of the NTH school. I also thank Prof. Gertrud Zwicknagl for agreeing to review this thesis. Special thanks are given to the staff of the Regional Computing Center for Lower Saxony at the Leibniz Universität Hannover (RRZN) who not only provided the computational resources but dedicated themselves to serve the users to their last breaths.

Eine Doktorarbeit ist – so habe ich herausgefunden – während vieler Phasen eine egoistische Angelegenheit, da man kaum Zeit für die wirklich wichtigen Dinge im Leben findet. Daher möchte ich meiner Frau Sandra dafür danken, dass sie diese lange Zeit ertragen, mich ertragen, mich unterstützt, geliebt, verstanden und aufgemuntert hat. Bei meiner Mutter möchte ich mich dafür bedanken, dass sie mich immer unterstützt und gefördert, für längere Zeiten sehr wenig zu Gesicht bekommen und sich nie darüber beschwert hat. Das gleiche gilt leider auch für viele noch nicht genannte Freunde. Dann sei noch allen ehrlich gedankt, die meinen, dass ich ihnen danken müsste, für was immer sie für mich getan haben. Ich war oft nicht aufmerksam während der Doktorarbeit, habe das vermutlich übersehen und es nicht absichtlich als selbstverständlich angenommen.

# Curriculum vitae

Malcolm Einhellinger

Geboren: 13.09.1980 in Wolfsburg (DE), dort zunächst wohnhaft.

- 1986* Umzug von Wolfsburg nach Tiddische (LK Gifhorn)
- 1987* Einschulung in die GS Parsau
- 1989* Wechsel in die GS/OS Rühren
- 1993* Wechsel auf das Gymnasium Kreuzheide (Wolfsburg)
- 2000* Abitur am Gymnasium Kreuzheide
- 2001* Zvildienst beim Paritätischen Sozialdienst in Wolfsburg
- 2002* Studium der Physik an der Universität Hannover,  
währenddessen Umzug nach Hannover
- 2007* Diplom-Abschluss in Physik
- seit 2007* Wiss. Mitarbeiter der Leibniz Universität Hannover (ITP)

Wissenschaftliche Publikationen:

M. Einhellinger, A. Cojuhovski, and E. Jeckelmann, Phys. Rev. B **85**, 235141 (2012), *Numerical method for nonlinear steady-state transport in one-dimensional correlated conductors*

# Selbstständigkeitserklärung

Hiermit versichere ich, die vorliegende Dissertation selbstständig angefertigt und keine anderen als die aufgeführten Hilfsmittel und Quellen verwendet zu haben. Keine anderen als die aufgeführten Institutionen wurden zu Hilfsleistungen herangezogen und keine wesentlichen Teile der Dissertation wurden bereits als Master-, Diplom- oder ähnliche Prüfungsarbeit verwendet.

-----  
Malcolm Einhellinger